



THE UNIVERSITY OF
WAIKATO
Te Whare Wānanga o Waikato

Research Commons

<http://researchcommons.waikato.ac.nz/>

Research Commons at the University of Waikato

Copyright Statement:

The digital copy of this thesis is protected by the Copyright Act 1994 (New Zealand).

The thesis may be consulted by you, provided you comply with the provisions of the Act and the following conditions of use:

- Any use you make of these documents or images must be for research or private study purposes only, and you may not make them available to any other person.
- Authors control the copyright of their thesis. You will recognise the author's right to be identified as the author of the thesis, and due acknowledgement will be made to the author where appropriate.
- You will obtain the author's permission before publishing any material from the thesis.

**The control of wind and waves on sediment transport asymmetry
and the long-term morphological development of estuaries**

A thesis

submitted in fulfilment

of the requirements for the degree

of Doctor of Philosophy

in Earth Sciences

at

the University of Waikato

by Stephen Hunt



THE UNIVERSITY OF
WAIKATO
Te Whare Wānanga o Waikato

2016

Abstract

Most theories on the equilibrium shape of estuarine basins highlight the dominance of tidal asymmetry in controlling the hydrodynamic and morphodynamic feedbacks that ultimately lead to a stable morphological state. This thesis uses field measurements, numerical modelling and sediment deposition records to investigate how waves interact with tidal processes and how these interactions influence sediment transport and the non-linear feedbacks between hydrodynamics and estuarine basin morphology.

Numerical modelling experiments were conducted over a series of idealised estuaries representing different stages of infilling, which show that wind and waves are far more efficient than tides at shaping intertidal areas, with the effect being subtly dependent on the depth distribution in the intertidal. Moreover, the wind and wave climate can substantially alter the hydrodynamic regime over the entire estuary and in intertidal areas can exert a much greater control on asymmetry than tidal currents alone, which dominate in the deeper channels. Under the effect of tides alone, currents over intertidal flats are found to remain flood-dominant as the estuary infills, thus promoting continued accretion until tidal currents become too weak to entrain sediment. Therefore, estuaries with only tidal currents are likely to evolve into in-filled areas of salt-marsh or mangrove with drainage channels, whereas fetch-aligned estuaries (in which wind-waves are common) have a greater probability of attaining deeper hydrodynamically-maintained stable intertidal areas. Although waves have little direct influence on hydrodynamics within the subtidal channel, the tidal asymmetry is controlled by the height and volume of the intertidal areas and therefore is indirectly influenced by wave activity.

The higher-energy, infrequent storm-wave events can considerably modify estuarine morphology over short timescales whereas lower-energy but perpetual effects like the tides operate continuously and so the relative contribution of such events in shaping the long-term morphological evolution can be considered on a range of timescales. Within this thesis a combination of hydrodynamic measurements, sediment deposition records and numerical modelling are used to determine the conditions under which observed waves are morphologically

significant. Morphological significance is defined as when waves influence tidal and suspended sediment flux asymmetry and subsequently infilling over geomorphological timescales. By comparing a fetch-aligned and a non fetch-aligned mesotidal basin, it is shown that for a sufficiently large fetch, even small and frequently occurring wind events are able to create waves that are morphologically significant. Conversely, in basins with a reduced fetch, wave events are less frequent and therefore of far less morphological significance.

The role of tidal range in controlling sediment transport is investigated through consideration of its influence on bed shear stress, τ_{max} . The decrease in bed shear stress associated with greater water depths is compared to increases owing to the larger fetch that accompanies the increased tidal range and the generally stronger currents associated with larger tidal range. Here, it is shown that during neap tides the reduction in water depths around high water and tidal currents are not offset by the reduction in fetch. Thus, it is shown that the basin-averaged τ_{max} is similar during both spring and neap tides in addition to the shorter duration of slack water during neap tides. Consequently, as τ_{max} is lower in the subtidal channel during neaps, the sediment gradient (and hence sediment transport potential) between tidal flats and channels is greater. Thus it is concluded that sediment deposition potential may actually be increased during a neap tide. This result is in sharp contrast to previous observations from microtidal wave-dominated environments, in which differences between spring and neap result in increased erosion during spring tides.

Overall, this thesis shows that short period locally generated waves can be considered a morphologically significant hydrodynamic process within estuaries. With increased fetch, waves become more morphologically significant relative to tides as even low, frequent wind speeds are able to generate waves that are capable of controlling patterns of sediment transport.

Acknowledgments

An extra special thank you must go to my supervisors Dr. Karin Bryan and Dr. Julia Mullarney from the University of Waikato for superb advice, guidance and support through much appreciated weekly meetings. Also many thanks to my supervisor Dr. Mark Pritchard from NIWA for valuable advice on my technical approach throughout this research, particularly during the field work part of this study. I can't imagine a harder working, more technically proficient or intellectually stimulating mentors, I have learned more than ever hoped for and I consider myself very fortunate to have worked with you all.

Extensive and valuable field assistance was given by the University of Waikato technical staff Dean Sandwell and Dirk Immenga who helped me solve considerable technical and logistical issues whilst collecting this unique dataset in Raglan Harbour, thank you very much for returning nearly 100% of what we aimed to collect. Special mention should go to Dean for his efforts during the intertidal data collection which was especially muddy, inaccessible and technically challenging but resulted in the collection of some valuable data. Dudley Bell, Phil Ross and Shawn Harrison from the University of Waikato also assisted greatly in the field.

The funding for this PhD research was provided by the Commonwealth Doctoral Scholarship Award, the ASLO Global Outreach Initiative and the Terry Healy Memorial Award. This funding enabled the research to progress and also facilitated my attendance at the Coastal Dynamics conference 2013 in France.

Although a PhD is a solitary experience, advice and help was always available from staff and my fellow students at the University of Waikato, especially my friends Alex Port, Shawn Harrison, Amir Emami and everyone in the Coastal and Marine Group. It has been a pleasure to study alongside you all; and I consider myself very lucky to have had such a supportive and fun learning environment. Thank you fellow PhD student and valued friend Hannah Mueller for your friendship, patience, coffee and cake.

Outside of the University lots of helpful and insightful comments helped to make this research more rounded and robust. Dr. Vernon Pickett and Dr. Hilke Giles

from Waikato Regional Council offered sound advice and data including LiDAR, bathymetry and sediment plate data from Raglan Harbour. Dr. Mal Green, Dr. Andrew Swales and Dr. Ian McDonald from NIWA all offered advice and access to data at various stages. The Taharoa wind data was supplied by NIWA through the CliFlo database. The Trustees of the Mai-Uenuku-ki-te-whenua Marae and the Trustees of Waingaro Pā gave valuable assistance, advice and guidance during the development of the fieldwork programme.

Thank you to friends and family both in the UK and NZ for all your support especially Mum, Dad, Greg and the incredible Raglan Whānau.

Finally but most importantly thank you to my wife Sarah who did not even hesitate when I suggested we move to NZ and leave behind her family, friends and career so I could study for my PhD in New Zealand. Your emotional, technical and sometimes financial support has been invaluable and thanks to you having already trodden along this precarious PhD path before, it made my journey far smoother.

Table of contents

Abstract	ii
Acknowledgments	iv
Table of contents	vi
List of Figures	ix
List of Tables	xviii
Chapter 1. Introduction	1
1.1 General introduction	2
1.2 Research objective and relevance	2
1.3 Approach and research questions	4
1.3.1 Case study site	5
1.3.2 Approach	7
1.4 Thesis outline and author contributions	8
Chapter 2. The influence of wind and waves on the existence of stable intertidal morphology in mesotidal estuaries.	11
2.1 Introduction	12
2.2 The influence of Eulerian and Lagrangian asymmetry on tidal–stage relationships	15
2.3 Methods	18
2.3.1 Model setup	18
2.3.2 Construction of idealised estuaries	20
2.3.3 Case study	22
2.4 Results	24
2.4.1 Tidal model	24
2.4.2 Tides, Winds and Waves	27
2.4.3 Case study	32
2.5 Discussion	33

2.6	Conclusions.....	39
Chapter 3. Observations of asymmetry in contrasting wave- and tidally-dominated environments within a mesotidal basin: implications for estuarine evolution		
		56
3.1	Introduction.....	57
3.2	Study area and field data collection.....	59
3.2.1	Study area.....	59
3.2.2	Instrumentation and methods.....	61
3.3	Results.....	65
3.4	Discussion.....	69
3.4.1	Contrasting stable states in the two arms.....	69
3.4.2	Timescale of processes.....	73
3.4.3	Defining morphologically-active wind conditions.....	75
3.5	Conclusions.....	81
Chapter 4. The effect of wind waves on spring-neap variations in sediment transport in two mesotidal estuarine basins with contrasting fetch.		
		97
4.1	Introduction.....	98
4.2	Study area and numerical modelling.....	100
4.2.1	Case study area.....	101
4.2.2	Field data and numerical model.....	102
4.2.3	Analysis of wind data and fetch.....	103
4.3	Results.....	105
4.3.1	Tides only.....	106
4.3.2	Tides, winds and waves.....	107
4.4	Discussion.....	108
4.5	Conclusions.....	115
Chapter 5. Conclusions and future research.....		
		128

5.1	General conclusions.....	129
5.2	Directions for future research	133
	References	134

List of Figures

Figure 1.1. Geomorphology of Whaingaroa (Raglan) Harbour.....	10
Figure 2.1. Schematic of different tidal asymmetries caused by Lagrangian and Eulerian affects. The schematic shows the distribution of τ caused by tidal currents (case 1 and case 2) and τ_{max} due to wave orbital and tidal currents combined (case 2 and case 3) as the water level changes with the tide. (Shear stresses are assumed to be basin-averaged). In each schematic, ebb and flood τ and τ_{max} are plotted as negative and positive values, respectively. The dashed line represents τ_c , above which sediment suspension occurs.	44
Figure 2.2. Numerical model grid and bathymetry. The model is forced at the single open boundary on the left hand side of the domain. The bathymetry in this figure is for the infilled basin ($\gamma=4.0$).....	45
Figure 2.3. Schematic of unfilled (young) (a) and infilled (mature) (b) idealised morphologies showing location of LW, MSL and HW with cross sections taken through centre of basin (c) for unfilled (solid line) and infilled (dashed line) basins.	46
Figure 2.4. Location of Raglan Harbour on the coastline of the North Island, NZ (a) and detail of estuary form (b) showing the locations of field deployments of the intertidal FSI current meter (dot marker) and the subtidal Sontek ADP (cross marker). The morphological form of the northern (Waingaro) and southern (Waitetuna) arms (locations shown in (b)) is summarised and compared with the idealised estuaries as a series of hypsometric curves (c) with $\gamma =4$ (dot dashed), $\gamma =3$ (thin dashed), $\gamma =2$ (thin solid), $\gamma =1.8$ (dotted), northern (Waingaro) arm (thick dashed) and southern (Waitetuna) arm (thick solid).	47
Figure 2.5. Modelling results for the case forced by tides only. (a) $\tau - \tau_c$, integrated over a transect through the centre of the basin perpendicular to the main channel, the transect is half that shown in Figure 2.3c. τ_c is for a 100 micron grain size. Flood and ebb-dominated residuals are positive and negative respectively. b) Intertidal profile taken along the same transect as in (a). τ spatially averaged over the subtidal (c) and intertidal (d) plotted as a function of water level, where $\gamma =4$	

(dot dashed), $\gamma = 3$ (dashed), $\gamma = 2$ (solid) and $\gamma = 1.8$ (dotted). Averaging is performed separately for flood and ebb tide. Note different x-axis scale between c and d ($\times 10$). See text for details of averaging technique..... 48

Figure 2.6. Depth-averaged flow residuals during a steady high-water level (no tide) with a spatially uniform and consistent 10 m/s seaward (easterly) (a and c) and 10 m/s landward (westerly) wind (b and d) for an infilled (a and b) and unfilled (c and d) morphology. Large arrows denote direction of wind. 49

Figure 2.7. Model results for scenarios with tides and winds (no waves), shown for basin morphologies $\gamma = 4$ (a, b, c and d) and $\gamma = 1.8$ (e, f, g and h). Panels (a) and (e) show the $\tau - \tau_c$ (for a 100 micron grain) averaged along a transect through the centre of the basin perpendicular to the main channel (the transect is half that shown in Figure 2.3c), Positive = flood and negative = ebb results. (b) and (f) Intertidal profile shape taken along the same profile as in (a) and (e). Bed shear stress spatially averaged over the subtidal (c and g) and intertidal (d and h) domains for each scenario (dot dashed: 10 m/s westerly; dashed: 5 m/s westerly; thin solid: 5 m/s easterly; dotted: 10 m/s easterly; thick solid: no wind). Averaging is performed separately for flood (plotted as positive) and ebb tide (plotted as negative). Note different scale between (c) and (g) and (d) and (h). Westerly winds are directed into the basin (landward) and easterly winds are directed out of the basin (seaward). See text for details of averaging technique. 50

Figure 2.8. Model results for scenarios with tides, winds and waves shown for basin morphologies $\gamma = 4$ (a, b and c) and $\gamma = 1.8$ (d, e and f). Panels (a) and (d): Intertidal profile shape taken along a transect through the centre of the basin perpendicular to the main channel, the transect is half that shown in Figure 2.3c. Panels (b, c, e and f): τ_{max} from currents and waves spatially averaged over the subtidal (b and e) and intertidal (c and f) domains as a function of water level for each scenario (dot dashed: 10 m/s westerly, dashed: 5 m/s westerly; solid: 5 m/s easterly; dotted: 10 m/s easterly). Averaging is performed separately for flood (positive) and ebb tide (negative). Westerly winds are directed into the basin (landward) and easterly winds are directed out of the basin (seaward). See text for detail of averaging technique..... 51

Figure 2.9. Panel a: The potential for deposition in the intertidal presented as the percentage of cells for which $\tau_{max} < \tau_c$ (for a 100 micron grain) at any moment during the tidal cycle for $\gamma = 4$ (dot dashed), $\gamma = 3$ (dashed), $\gamma = 2$ (solid) and $\gamma = 1.8$ (dotted) morphologies. Panels b-g: spatial distribution of the length of time in minutes for which $\tau_{max} < \tau_c$ for a tide only scenario (b and e) and a 5 m/s (c and f) and 10 m/s (d and g) landward (westerly) wind and wave event for a unfilled ($\gamma = 4.0$) (b, c and d) and an infilled ($\gamma = 1.8$) (e, f and g) basin. The locations of panels b-g are marked on panel a. 52

Figure 2.10. Model results from the case study with tides, winds and waves for the less infilled fetch-aligned northern (Waingaro) arm (a, b and c) and the more-infilled non fetch-aligned southern (Waitetuna) arm (d, e and f), see Figure 2.4b for locations. The τ results from the tide only model are shown in (a) and (b) where the thick line is subtidal values and thin line is intertidal values. τ_{max} due to tides, winds and waves averaged over the subtidal (b and d) and intertidal (c and e) domain, where dashed dot: 10 m/s southwesterly; dashed: 5 m/s southwesterly; solid: 5 m/s northeasterly; dotted: 10 m/s northeasterly. Averaging is performed separately for flood (positive) and ebb (negative) tide. Southwesterly winds are directed into the basin (landward) and easterly winds are directed out of the basin (seaward). See text for details of averaging technique..... 53

Figure 2.11. Schematic representation of asymmetry-related processes identified using simple analytic relationships (see text). Panel (a) the tidal asymmetry parameter T predicted in equation 2.1 and 2.2 (solid line) and the percentage of time during the tidal cycle that the intertidal is exposed (dashed line). These equations predict that a stable intertidal should occur when $T=0$. Panel (b) τ_w averaged over the intertidal and over a tidal cycle for each hypsometry during a fetch perpendicular (b) and fetch parallel wind direction (c) and wind speeds ranging between 0 and 10 m/s, black circles show the maximum τ_w 54

Figure 2.12. Water levels (solid line) and current velocities (dotted line) collected using a Sontek ADP (subtidal) and current velocities (dashed line) collected with a FSI 3DACM Wave recorder showing contrasting tidal asymmetries over the intertidal and subtidal areas of the northern (Waingaro) arm of Raglan Harbour, New Zealand. The locations of deployments are shown in Figure 2.4b 55

Figure 3.1: Location map showing location of Raglan (red square) and the Taharoa weather station (●) (a) and the field measurement locations (b). Inset (c) shows the area indicated by the blue box. The black, grey and light grey lines show the Highest Astronomical Tide, Mean Sea Level and Lowest Astronomical Tide depth contours. Dots show locations of sediment plate measurements SP1, SP2 and SP3. T1 and T2 show locations of instrument transects consisting of Optical Backscatter (Δ), current meter (+) and Dobie wave gauge (○). An Acoustic Doppler Velocimeter (◇) was deployed in the southern arm and an Acoustic Doppler Profiler (x) in the northern arm. A weather station was deployed in the main part of the estuary near the mouth of the southern arm (*). The arrow above the scale bar shows the strongest prevailing wind direction (from the SW). The dashed polygons define the approximate limits of each arm and the areas considered in the hypsometry calculations. (d) Hypsometric curves comparing area to height distribution for the northern (dashed thick line) and the southern (solid thick line) arms. (e) Depth profiles at the T1 (solid line) and T2 (dashed line) transects. 86

Figure 3.2: Wind rose showing the wind speed (denoted by colour), the wind direction (direction from, denoted by the orientation of the bars) and the frequency of occurrence (denoted by the length of each bar) (panel a), wind data are from Taharoa (see Figure 1a for location) collected between (10th August 1978 and 1st January 2013). Using fetch distances at high water from aerial photography, the wind records are converted into the distribution of predicted wave conditions for the northern (Waingaro) (panel b) and the southern (Waitetuna) (panel c) arms. Significant wave height, wind direction and the frequency of occurrence are denoted by the colour, orientation and length of each bar, respectively..... 87

Figure 3.3: Timeseries collected during the field deployment. Locations of instruments are shown in Figure 3.1. Panel a shows water levels from the Acoustic Doppler Profiler (northern arm). Panel b shows depth averaged velocities from the northern arm (Acoustic Doppler Profiler in dark red and T1 and T2 in light and dark blue, respectively), and the Southern arm (Acoustic Doppler Velocimeter orange line). Panel c shows significant wave height at T1

(light blue) and T2 (dark blue). Panel d shows suspended sediment concentration measured using the lower sensor at T1 (light blue) and T2 (dark blue). Panel e shows the wind conditions measured at the Raglan weather station with speed (black line) and direction from (arrows). 88

Figure 3.4: Tidal stage figures showing τ (bin averaged over entire deployment, with 0.1 m vertical resolution) plotted for each water level for the northern arm (a): Acoustic Doppler Profiler (solid line), T1 (dash-dotted line) and T2 deployments (dashed line); and the southern arm Acoustic Doppler Velocimeter (b). 89

Figure 3.5: Tidal stage figures for (fetch-aligned) T2 deployment showing τ (solid line), τ_w (dashed line), τ_{max} (dash-dotted line) and suspended sediment concentrations (SSC). Cases are shown for a tidal cycle with no waves (a and b), a tidal cycle during a spring tide and a moderate wind speed (c and d), a spring tide and a high wind speed (e and f) and a neap tide with a moderate wind speed (g and h). Mean significant wave height (H_s), wind speed (WS) and direction (WD) are shown for each case..... 90

Figure 3.6: Panel a shows significant wave height (denoted by the colour) and frequency of occurrence (denoted by the length of each column relative to the scale bar) for each Dobie deployment. The direction of wind blowing during each wave event is taken from the Raglan weather station and is shown by the orientation of each column. Panel b shows the magnitude, frequency and direction of wind recorded at the Raglan weather station during each deployment. 91

Figure 3.7: Tidal stage figures for the T1 deployment showing τ (solid line), τ_w (dashed line) and τ_{max} (dash-dotted line). Cases shown are for a tidal cycle with no waves (a), a tidal cycle during a spring tide and a moderate wind speed (b), a spring tide and a high wind speed (c) and a neap tide with a moderate wind speed (d). Significant wave height, wind speed and direction are shown for each case. No suspended sediment concentrations are available for the T1 deployment due to instrument malfunction..... 92

Figure 3.8: Occurrence of wind speeds above 5m/s between 30th April 2012 and 29th September 2013 presented as percentage function of time of day. 93

Figure 3.9: (a) Percentage of time when $\tau_w > \tau$ over the entire intertidal area (solid lines) and at the location of the Dobie wave gauge (dashed lines) for neap (magenta), intermediate (blue) and spring (red) tides within an estuary with a maximum fetch of 5 km. Observations from the Dobie wave gauge are shown as circles. (b-d) Timeseries of τ in the channel (solid thick black line) against calculated τ_w (thin coloured lines) for intermediate (c), spring (d) and neap (e) tidal states. Wind speeds shown are 5 m/s (light blue), 10 m/s (orange) and 15 m/s (dark red) at the upper (dashed line), mid (dotted line) and lower (solid line) areas of the intertidal. The lower line is at the same location as the Dobie wave gauge, and the locations of the data points within the intertidal profile are shown in b. 94

Figure 3.10: (a) Percentage of time when $\tau_w > \tau$ over the entire intertidal area (solid lines) and at the location of the Dobie wave gauge (dashed lines) for neap (magenta), intermediate (blue) and spring (red) tides within an estuary with a maximum fetch of 2 km. (b-d) Timeseries of τ in the channel (solid thick black line) against calculated τ_w (thin coloured lines) for intermediate (c), spring (d) and neap (e) tidal states. Wind speeds shown are 5 m/s (light blue), 10 m/s (orange) and 15 m/s (dark red) at the upper (dashed line), mid (dotted line) and lower (solid line) areas of the intertidal. The locations of the data points within the intertidal profile are shown in b. 95

Figure 3.11: Three month running average of NOAA Oceanic Nino Index (ONI, black line), occurrence of south westerly winds (coloured by speed) as a percentage (panel a). Positive ONI denotes El Niño and negative denotes La Niña and the index is considered significant by NOAA when >0.5 and <-0.5 . Sediment plate data showing relative sediment depth (adjusted relative to first measurement) at each plate with coloured line showing mean of results for SP3, southern arm (panel b), SP1 (panel c) and SP2, northern arm (panel d). Wind data are from Taharoa weather station (see Figure 1a for location) modified according to the wind data collected in the Raglan Harbour. 96

Figure 4.1: Location map showing location of Raglan (red square) and the Taharoa weather station (●) (a) and the field measurement locations (b). Inset (c) shows the area indicated by the blue box. Model extent is same as b (red box in a). The black, grey and light grey lines show depth contours of the Highest Astronomical Tide, Mean Sea Level and Lowest Astronomical Tide. Dots show locations of sediment plate measurements SP1, SP2 and SP3. T1 and T2 show locations of instrument transects consisting of Optical Backscatter (Δ), current meter (+) and Dobie wave gauge (\circ). An Acoustic Doppler Velocimeter (\diamond) was deployed in the southern arm and an Acoustic Doppler Profiler (x) in the northern arm. S4 current meters were deployed in the main part of the estuary and at the mouth of the northern and southern arms (\star). Boundary tidal conditions were taken from constituents extracted from observation from the Manu Bay tidal gauge (\otimes). 117

Figure 4.2: Frequency distribution of wind using the observations collected at Taharoa (see Figure 1a for location) recorded between 10th August 1978 and 1st January 2013 (a) and at Raglan (see Figure 1b for location) recorded between 30th April 2012 and 29th September 2013 (b). The long term record used to describe wind conditions within the model simulations was based on a linear relationship between records at Taharoa and Raglan (c), see text for details. 118

Figure 4.3: Fetch distribution with depth within the northern (Waingaro) arm (a) and the southern (Waitetuna) arm (b) for wind directions of 80° (blue line), 235° (red line), 135° (black line) and 315° (cyan line). Solid lines show maximum fetch within each basin and dashed lines show average fetch over entire basin. Horizontal dashed lines show tidal heights in Figures 4.4, 4.5 and 4.6. 119

Figure 4.4: Tidal stage diagrams for a tide only scenario (black line), an 80° (orange line), 135° (dark red line), 235° (cyan line) and 315° (dark blue line) wind direction and a 2 (dashed lines), 5 (dotted lines) and 10 m/s (dash-dot lines) wind speeds. The tidal state shown here is for a single tidal cycle midway between a spring and a neap. The level of τ is averaged over the intertidal (a) and subtidal (c) in the northern (Waingaro) arm and the intertidal (b) and subtidal (d) in the southern (Waitetuna) arm. 120

Figure 4.5: Tidal stage diagrams for a tide only scenario (black line), an 80° (orange line), 135° (dark red line), 235° (cyan line) and 315° (dark blue line) wind direction and a 2 (dashed lines), 5 (dotted lines) and 10 m/s (dash-dot lines) wind speeds. The tidal state shown here is for a single neap tidal cycle. The level of τ is averaged over the intertidal (a) and subtidal (c) in the northern (Waingaro) arm and the intertidal (b) and subtidal (d) in the southern (Waitetuna) arm. 121

Figure 4.6: Tidal stage diagrams for a tide only scenario (black line), an 80° (orange line), 135° (dark red line), 235° (cyan line) and 315° (dark blue line) wind direction and a 2 (dashed lines), 5 (dotted lines) and 10 m/s (dash-dot lines) wind speeds. The tidal state shown here is for a single spring tidal cycle. The level of τ is averaged over the intertidal (a) and subtidal (c) in the northern (Waingaro) arm and the intertidal (b) and subtidal (d) in the southern (Waitetuna) arm. 122

Figure 4.7: Hypsometry of the northern arm (Waingaro: solid blue line) and the southern arm (Waitetuna:dashed red line) between 2.5 and -2.5 mMSL. To enable comparison between the different-sized arms the area is scaled by dividing area above specified elevation (a) by maximum overall basin area (A). Horizontal dashed lines show the locations of high water springs (HWS) and low water springs (LWS) in Figure 6; high water mid (HWM) and low water mid (LWM) in Figure 5; high water neaps (HWN) and low water neaps (LWN) in Figure 4.4. 123

Figure 4.8: Values of τ_w for a range of wind speeds and fetches for a single fixed typical neap (1.5 m, a) and spring (3 m, b) water depth. The vertical black dashed lines represent maximum fetch length in the northern arm of the case study site. The horizontal black dashed lines represent approximate maximum basin averaged values of τ in the subtidal channel from the Raglan Harbour numerical model. 124

Figure 4.9: Values of τ_w calculated for a range of fixed water depths and fetches for a strong (10 m/s, a), a moderate (5 m/s) and a weak (2 m/s, c) wind speed. The vertical black dashed lines represent maximum fetch length in the northern arm of the case study site. The horizontal black dashed and dotted lines represent approximate maximum basin-averaged values of τ in the subtidal channel during a

spring and neap tide from the Raglan Harbour numerical model. Note the change in y-axis scale between a, b and c..... 125

Figure 4.10: Calculated values of τ_w for a range of fixed water depths and fetches for a strong (10 m/s, a), a moderate (5 m/s) and a weak (2 m/s, c) wind speed. The horizontal black dashed and dotted lines represent approximate maximum basin-averaged values of τ in the subtidal channel during a spring and neap tide from the Raglan Harbour numerical model. Note the change in y-axis scale between a, b and c. 126

Figure 4.11: Values of τ_w for a range of wind speeds and fetches for a typical neap (1.5 m, a) and spring (3 m, b) water depth (solid lines). Values of τ_w are also shown for water depths modified by storm setup, taking into account both fetch and wind speed (dashed lines) The vertical black dashed lines represent maximum fetch length in the northern arm of the case study site. The horizontal black dashed lines represent approximate maximum basin-averaged values of τ in the subtidal channel of Raglan Harbour numerical model. 127

List of Tables

Table 2.1. Comparison of hydrodynamic, sedimentological and biological factors associated with convex and concave up morphologies.	41
Table 2.2. Summary of idealised geometries.	42
Table 2.3. Summary of modelled scenarios presented in this paper.	43
Table 3.1 Summary of instrumentation, deployment dates and parameters measured. See Figure 3.1 for locations of instruments.	83
Table 3.2: Influences of different hydrodynamic forcing due to frequency, type and magnitude of affect (SSC is suspended sediment concentration).....	85
Table 4.1: Modelled wind scenarios.....	116

Chapter 1. Introduction



Waingaro River Mangroves, Whaingaroa (Raglan) Harbour.

1.1 General introduction

Estuaries form at the interface between rivers and the ocean. The most commonly accepted definition (Dyer, 1997, Woodroffe, 2002) is provided by Cameron and Pritchard (1963); this definition was adapted by Dyer (1997) to give the following comprehensive description: “An estuary is a semi-enclosed coastal body of water which has free connection to the open sea, extending into the river as far as the limit of tidal influence, and within which sea water is measurably diluted with fresh water derived from land drainage”.

Estuaries are widespread worldwide with 1,200 major systems mapped covering a total area of ~500,000 km² (Agardy and Alder, 2005) and are encountered in a variety of tidal ranges and a wide range of climatic zones. Estuaries are formed from flooded river valleys due to rising sea levels following the last glacial maximum and are highly diverse in appearance, shaped by a combination of geological, hydrodynamic and biological factors (Dyer, 1997). The geology of paleo river valleys provides the underlying form around which the contemporary estuary basin forms, providing areas of flow constriction and divergence. Within the flooded river basin, the level of contemporary sediment infilling is controlled by hydrodynamics and the availability of sediment from either the open ocean, fluvial sources or redistributed within the estuarine system, where it is eroded, transported and deposited elsewhere. This sediment can be comprised of sand, shell, muds and silts, and the amount of sediment controls the distribution and extent of any intertidal flats. The morphology is related to the hydrodynamics and sediment transport in a non-linear fashion, whereby deposition of sediments modifies the morphology which in turn affects hydrodynamics and deposition. It is the non-linear feedback between tides, waves, sediments and morphology that forms the central theme of this thesis.

1.2 Research objective and relevance

Lying at the interface between fresh and saline water, estuaries provide important ecological, social and economic functions. Intertidal flats also host saltmarsh and mangrove habitats; both mangroves and salt marsh vegetation are able to influence the hydrodynamics through processes such as attenuation of waves

(Möller et al., 1999; Quartel et al., 2007; Riffe et al., 2011), flow routing and stabilisation of tidal channel networks (van Maanen et al., 2015) and promote sedimentation during periods of sea level rise (van Maanen et al., 2015). Mangroves, saltmarshes and seagrasses provide vital coastal habitats for bird and marine life (Dayton, 2003) and play an important coastal defence function (Bouma et al., 2014). The establishment of coastal vegetation is critically sensitive to the inundation regime which in turn is controlled by the intertidal morphology and therefore patterns of erosion and deposition (Mokrech et al., 2015). Humans have also been drawn to estuaries for fisheries and sheltered waters for ports and harbour and many estuarine environments now feature large populations and important port infrastructure with 62% of the world's major estuaries situated within 25km of urban centres with 100,000 people or more (Agardy and Alder, 2005). These anthropogenically-modified environments have historically required modification from their natural state, a process that continues today. Navigation is facilitated by dredging of deep water channels, and these deepened channels can be prone to infilling requiring repeat maintenance dredging projects. Ports are often built on reclaimed intertidal land using dredging material. Dredging and reclamation can directly disrupt marine life and coastal habitats and fundamentally alter the tidal prism of the harbour, influencing patterns of tidal asymmetry (Colby et al., 2010) and flushing, thus altering sediment and nutrient transport which are dependent on tides (Tay et al., 2012, Kaiser et al., 2013). Training walls fix and divert the mouths of estuaries, sometimes hindering the transfer of sediment along the open coast and between the estuary and the open sea. Seawall construction also modifies waves and currents causing erosion and scour. Both deficit and surplus sediment can create problems in estuarine environments. Catchment deforestation enhances runoff which dramatically modifies the morphology of estuaries and smothers marine life. Conversely, coastal protection and dam construction prevents erosion and redistribution of sediments which can enhance erosion elsewhere in the estuary system. Estimates of sediment flux from rivers shows that humans have both increased (due to soil erosion) and decreased (due to dam construction) sediment input to the coastal zone with a net worldwide deficit of 1.4 BT/yr compared to pre-human levels (Syvitski et al., 2005). Climate change is predicted to impact estuarine environments by modifying sea levels, tidal characteristics, the

frequency and magnitude of wave events and freshwater runoff (Wong et al., 2014). In areas backed by sea defences or steep topography with low sediment availability, the phenomenon of ‘coastal squeeze’ may occur where intertidal habitat is prevented from migrating landwards and instead declines in extent (Tono and Chmura, 2013, Mokrech et al., 2015). These changes will have consequences for sediment transport and sediment availability and therefore morphology and habitat distribution; furthermore, the non-linear interactions within estuaries mean that these changes may lead to unanticipated responses.

In summary, estuarine environments are complex systems and are home to vulnerable and valuable ecosystems and human infrastructure. To better manage these systems into the future, a sound knowledge of physical and morphological processes is required. The objective of this research is to expand the understanding of the interactions between tides, waves, sediment transport and morphology within mesotidal estuaries by addressing three main research questions which are outlined in the following section.

1.3 Approach and research questions

Tides and tidal asymmetry are often cited as the main hydrodynamic process controlling sediment transport and deposition within estuaries (Friedrichs and Aubrey, 1988, Friedrichs, 2011). Although the importance of waves is well recognised in microtidal estuaries (Fagherazzi et al., 2007) where tidal range and velocity is small in comparison to the forces exerted by waves, the role of waves in mesotidal estuaries is less well understood. Within mesotidal estuaries, the interactions between waves and tides are potentially complex, tidal forces are proportionally stronger (compared to microtidal environments), sometimes capable of transporting large volumes of sediment and can also be strongly asymmetric. In addition, water levels are also highly variable between spring and neap tides affecting fetch and water depth and therefore the strength of near-bed orbital velocities.

The hypothesis central to this thesis states that if the morphology of an estuary has a fetch which is aligned with the dominant wind direction then waves will be the dominant forcing mechanism responsible for shaping the estuary. Furthermore,

wave-dominated and tidally-dominated environments will be characterised by distinct morphologies due to the differing non-linear feedback processes between tides, waves, sediments and morphology. This hypothesis has been tested through the following research questions:

- 1 How do waves and tides interact to control whether an estuary exports or imports sediment?
- 2 How does the morphology (fetch and intertidal shape) influence whether exporting or importing conditions occur, and how does this vary spatially through an estuary?
- 3 Waves depend on wind conditions, which can vary over a number of timescales. Under what conditions do waves become more important than tides for modifying asymmetry?

These questions have been answered using a combination of idealised numerical modelling, field work and numerical modelling of a real-world system.

1.3.1 Case study site

This thesis uses the case study site of Whaingaroa (Raglan) Harbour (Figure 1.1) on the west coast of the North Island, New Zealand. The estuary is a dendritic mesotidal system formed by the post-glacial drowning of a river system, the mouth of the estuary is enclosed by black sand beaches and dunes (Figure 1.1j) and is classified as a barrier enclosed drowned river valley (Sherwood and Nelson, 1979; Hume et al., 2007). Rocky outcrops partially control the dendritic estuary form (Figure 1.1a, d and h), this geomorphic control is particularly apparent at the “Narrows” where the mouth of the southern arm is heavily constricted (Figure 1.1h). Freshwater input is low relative to the tidal prism and salinities vary little throughout the estuary and therefore the estuary is described as predominantly well-mixed (Heath, 1976; Heath and Shakespeare, 1977, Sherwood and Nelson, 1979).

Whaingaroa (Raglan) Harbour exhibits distinct sedimentary (Swales et al, 2005, Bentley et al., 2014) and sedimentological (Sherwood and Nelson, 1979) characteristics in each arm of the harbour. The intertidal of the northern

(Waingaro) arm is characterised by limited deposition and coarser intertidal sediments (Figure 1.1c, e and f) whereas the southern (Waitetuna) arm is characterised by extensive deposition of fine sediments (Figure 1.1g). This distinction between the northern (Waingaro) and southern (Waitetuna) arms is hypothesised to be primarily due to fetch length in relation to prevailing wind direction. In the northern (Waingaro) arm the fetch is aligned with the prevailing wind direction allowing the generation of waves (Figure 1.1b) and preventing the deposition of sediment. In contrast the southern (Waitetuna) arm has a constricted mouth (Figure 1.1h) and is sheltered from the prevailing wind direction and therefore tidal processes are predominant allowing the deposition of sediment. Whaingaroa (Raglan) Harbour has been selected as a case study site because the spatial variability in sedimentation and morphology within a single system allows a direct comparison to be easily made between the two environments.

As outlined in Section 1.2, estuaries are subjected to a wide range of anthropogenic influences which impact on various aspects of the estuarine system such as sediment supply, hydrodynamics, morphology and ecology. These factors are connected through complex linear and non-linear feedbacks (McGlathery et al., 2013) and consequently the cause and effect of each aspect in a modified estuarine system can be difficult to determine. Furthermore, the delineation between natural and anthropogenic aspects of the system becomes difficult and arbitrary. The study site is largely unmodified (apart from catchment deforestation) with no reclamation, no dredging and limited coastal defences and therefore any distinction between the two arms will not be due to anthropogenic modification of the tidal prism. On a global scale the unmodified nature of the estuary is crucial and almost unique.

This estuary configuration is not unique to New Zealand and therefore the choice of case-study site will have applications worldwide in other similar mesotidal, well mixed systems. The dendritic shape of Whaingaroa (Raglan) Harbour means that the research will be less applicable in systems that are convergent (e.g. the ‘funnel’ shape of the Severn Estuary, Thames Estuary, Humber estuary) and the research will also be less applicable in poorly mixed, stratified systems where circulation is highly modified by patterns of salinity. However, the modification

of tidal asymmetry by wave processes in universally applicable, especially in systems with a standing or partially progressive tidal wave.

A detailed description of Whaingaroa (Raglan) Harbour is provided in Chapters 3 and 4.

1.3.2 Approach

Idealised modelling involves building a simplified numerical model of an actual system whilst still retaining enough complexity to allow the model to adequately replicate elements of the actual system. Idealised modelling is advantageous as it requires less computational effort and also helps make a complex system easier to understand. For this thesis, idealised modelling has been applied for a series of synthetic estuarine basins in Delft3D. These basins have been tested with both waves and tides to test the interaction between hydrodynamics and the morphology. A detailed description of the idealised modelling is provided in Chapter 2.

To test the results of the idealised model, field data was collected in Whaingaroa (Raglan) Harbour. Results from the idealised model were used to help select instrument deployment sites for a field program. Data collected included wind, waves, currents, water levels and suspended sediment. The field data provided information for a detailed comparison of hydrodynamic processes between the two arms of the harbour and an analysis of how waves and tides interact and influence sediment transport. A detailed description of the field data is provided in Chapter 3.

A numerical model of Whaingaroa (Raglan) Harbour was used to both validate the more general results of the idealised model by comparing it to a real-world example and also to extend the results of the field deployment to the rest of the harbour. A detailed description of the numerical model is provided in Chapter 4.

1.4 Thesis outline and author contributions

This thesis describes research investigating the interactions between waves, tides and estuarine morphology. The research is presented in 3 Chapters and although these chapters are related through common themes, each chapter can be read separately with a distinct introduction, methodology, results, discussion and conclusions.

In Chapter 2, the interactions between waves, tides and morphology are explored using an idealised model in Delft3D. Realistic morphologies with different amounts of sediment infilling were created using hypsometric relationships and were modelled using winds, waves and tides. Changes to tidal asymmetry for each morphological scenario are compared. This chapter has been published in the journal *Geomorphology* (Hunt et al., 2015). I wrote all of the numerical code to process and analyse the data, ran the numerical modelling scenarios, prepared all of the figures and wrote the initial and subsequent drafts of the article. My co-authors, K. R. Bryan and J.C. Mullarney edited drafts and provided helpful direction.

In Chapter 3, the field data collected in Whaingaroa (Raglan) Harbour is analysed to verify the results from the idealised model in Chapter 2 and to contrast the hypothesised wave and tidally dominated arms of the estuary. A historic wind record is used to identify the probability of a geomorphologically significant wave being generated in the estuary and any variability due to El Niño and La Niña climatic patterns. This chapter has been published in the journal *Earth Surface Processes and Landforms* (Hunt et al., 2016). I wrote all of the numerical code to process and analyse the field data, prepared all of the figures and wrote the initial and subsequent drafts of the article. The field data were collected with assistance of Dean Sandwell, Dirk Immenga, Dudley Bell, Phil Ross and Shawn Harrison from the University of Waikato. The sediment data was supplied by Waikato Regional Council. My co-authors, K. R. Bryan, J.C. Mullarney and M. Pritchard edited drafts and provided helpful direction.

In Chapter 4, the numerical model of Whaingaroa (Raglan) Harbour is developed in Delft3D. This model is used to extend the field work analysis throughout the

entire basin. The model scenarios are chosen based on the historic wind record and are tested over spring and neap tides. The results of the numerical modelling study are then related to the contemporary morphological form of the estuary. This chapter has been submitted and is under review in the journal *Geomorphology*. I wrote all of the numerical code to process and analyse the field data, created the hydrodynamic model, prepared all of the figures and wrote the initial and subsequent drafts of the article. The fieldwork used for the calibration was collected with assistance of Dean Sandwell, Dirk Immenga, Dudley Bell, Phil Ross and Shawn Harrison from University of Waikato. The sediment and LiDAR data were supplied by Waikato Regional Council. Part of the Raglan bathymetry used in the model was supplied by Shawn Harrison. My co-authors, K. R. Bryan and J.C. Mullarney edited drafts and provided helpful direction.

In Chapter 5, the research is summarised along with potential directions for future research.

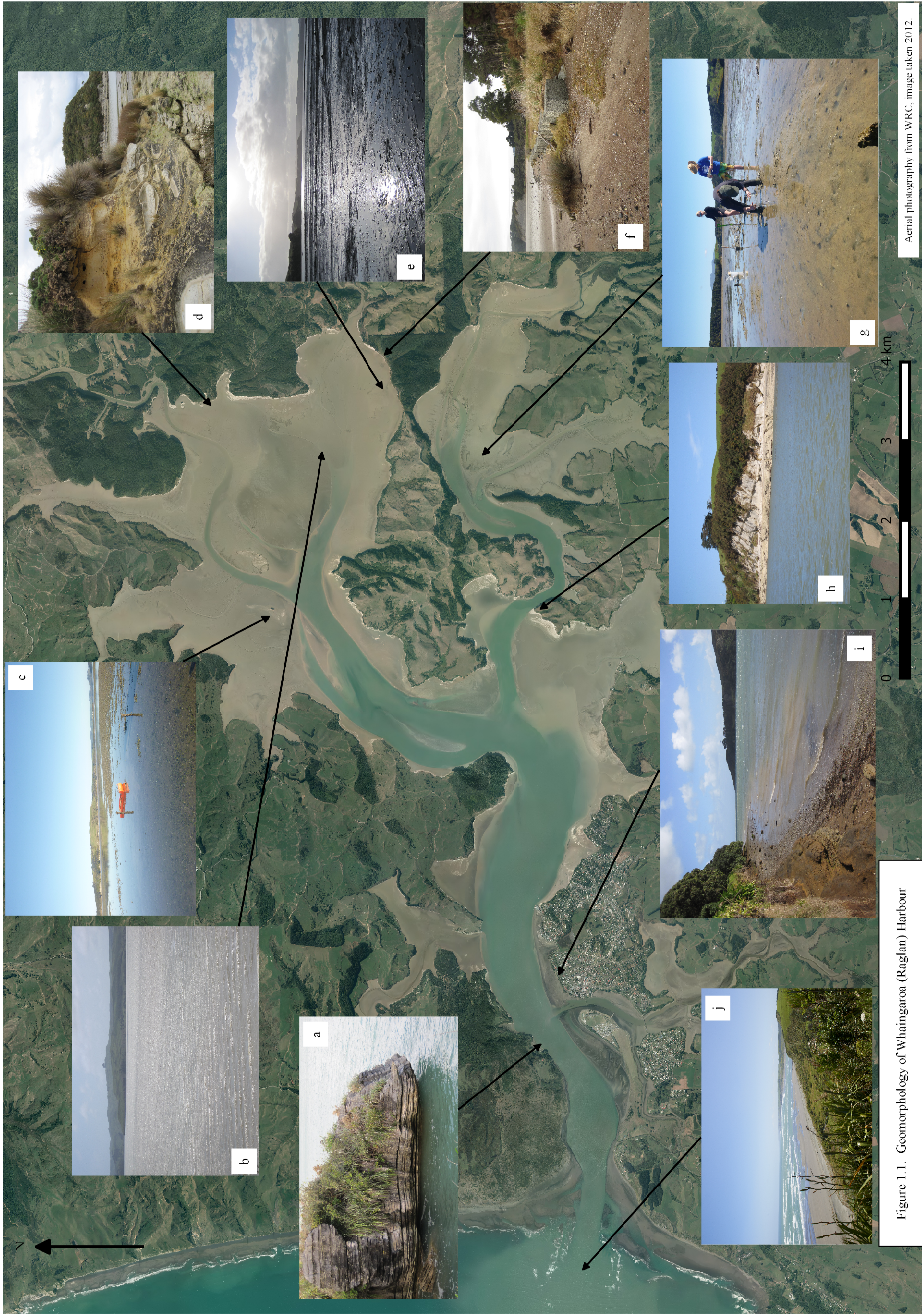


Figure 1.1. Geomorphology of Whaingaroa (Raglan) Harbour

Aerial photography from WRC, image taken 2012.

Chapter 2. The influence of wind and waves on the existence of stable intertidal morphology in mesotidal estuaries.



Waves in Whaingaroa (Raglan) Harbour).

2.1 Introduction

Coastal tidal currents largely control the pathway of sediments between estuaries and the open ocean, and ultimately determine whether estuaries are a permanent sink or temporary reservoir for sediment. Non-linear feedbacks between physical processes and the estuarine morphology can result in possible regime shifts where the estuary alternates between stable morphologies (or stable ‘states’) (McGlathery et al., 2013; Mariotti and Fagherazzi, 2013a). Stability in this case relates to a bathymetry which returns to the same configuration following perturbation (e.g. by storms or sediment pulses). The stability of estuaries is not only essential to the development of intertidal ecosystems but is also important for the maintenance of navigable shipping channels and recreational access.

The intertidal morphology is controlled by the rate of infilling, which is dependent on a non-linear feedback, whereby the hydrodynamics reshape the estuarine morphology, which in turn controls whether the seaward (ebb) tidal currents dominate over the landward (flood) currents (Dronkers, 1986; Friedrichs and Aubrey, 1988; Wang et al., 2002). Infilling is initiated by flood dominance which causes transport of sediments into the estuary; uneven infilling causes the intertidal areas to increase in elevation relative to the channels. The increased intertidal elevation causes a shift to ebb dominance and sediment export which is then limited by an eventual return to flood dominant conditions (Dronkers, 1986; Pethick, 1994; Friedrichs, 2010; 2011). This feedback process has been hypothesised to result in the emergence of stable intermediate equilibrium geometry between the extreme and unstable flood and ebb dominant regimes (Friedrichs, 2011).

Net sediment transport over a periodic tidal cycle can occur because of temporal asymmetries or Eulerian effects (e.g. distortion of the tidal wave from a sinusoidal shape) or spatial gradients or Lagrangian effects (e.g. sediment concentration gradients or settling lag effects). We refer to these as ‘Eulerian asymmetry’ and ‘Lagrangian asymmetry’ following Ridderinkhof (1997) and Friedrichs (2011). Eulerian asymmetry occurs when the tidal wave is distorted as it propagates across the adjacent shelf and through the estuary, creating an asymmetry between the magnitude of the flood and ebb tidal velocities, owing to relative differences

in either speed or duration of the ebb and flood stages of the tidal cycle (Aubrey and Speer, 1985; Speer and Aubrey, 1985; Friedrichs and Aubrey, 1988; Lanzoni and Seminara, 2002, Friedrichs, 2010). The influence of Eulerian asymmetry on sediment transport affects the coarse bedload sediment (sands and gravels) more than the fine sediment (muds, clays and silts) which travels in suspension (Green et al., 1997; Dronkers, 1986; Bolle et al., 2010). Coarse grains respond to whether the local critical threshold current speed for sediment motion is exceeded, with the rate of bed load transport approximately proportional to the cube of the current speed (Pugh, 2004), so a small asymmetry in tidal velocity results in a large increase in potential for net sediment transport over a tidal cycle. Fine sediments (muds, clays and silts) tend to travel as suspended load and have much longer settling velocities than coarser sediments (sands and gravels) that travel as bedload (Whitehouse et al., 2000), and so will be more affected by the duration of slack water.

Studies in estuarine environments using field observations and analytical solutions have shown that local winds create a superimposed residual current, with downwind currents over shallow areas and upwind currents within the subtidal channels (Wong, 1994, Sanay and Valle-Levinson, 2005; Narváez and Valle-Levinson, 2008). The reason for these opposing wind-driven currents is due to the imbalance between the accelerations provided by wind drift and those provided by the barotropic pressure gradient (Wong, 1994). In the shallow areas adjacent to the main channel, the acceleration from wind drift increases the flow in the same direction as the wind raising the water level downwind and forming a pressure gradient. This pressure gradient returns water against the wind down the channel resulting in a flow that opposes the wind (Narváez and Valle-Levinson, 2008). Fine sediments are influenced by this long-term residual circulation, which also in turn may be influenced by the baroclinicity within an estuary system.

In addition to modification of circulation patterns (Narváez and Valle-Levinson, 2008), winds also influence the hydrodynamics through the generation of short period waves, which can also control near-surface shear (Henderson and Mullarney, 2013). In shallow water, small locally-generated waves exert a bed shear stress which is comparable to a substantial tidal current (Le Hir et al., 2000)

and therefore have the potential to influence a significant component of the sediment transport regime particularly in the relatively shallow intertidal areas (de Lange and Healy, 1990; Green et al., 1997; Janssen-Stedler, 2000; Green et al., 2000; French et al., 2008; Green, 2011; Shi et al., 2012). Waves principally mobilise bed sediments through the influence of seabed orbital velocities which increase in intensity with wave size and wavelength and decrease in intensity due to the exponential decay of orbital velocities with increasing water depth (Soulsby, 1997). Within an estuary, the greatest potential for wave generation is at high water when the largest fetch is available. However, due to the attenuation of wave orbital velocities with increasing depth, the maximum impact of the orbital velocities will occur at a point at which there exists a balance between the available fetch for wave generation and sufficiently shallow water depths that allow the orbital velocities to reach the seabed (Green et al., 1997; Fagherazzi and Wiberg, 2009). Studies in estuarine environments have identified the importance of wind-waves in sediment transport processes due to the ‘stirring’ affect of wave orbital velocities over the intertidal flats (de Lange and Healy, 1990; Green et al., 1997; 2000; Swales et al., 2004). These studies indicated that waves alone controlled turbidity levels on the intertidal sandflats and tidal processes were restricted to controlling turbidity levels only in the main channel of the estuary.

Simplified modelling (Roberts et al., 2000; Waeles et al., 2004), analytical solutions (Friedrichs and Aubrey, 1996; Friedrichs, 2011) and empirical data (Kirby, 2000; 2002; Mehta, 2002; Bearman et al., 2010) have shown that convex-upwards and concave-upwards intertidal surfaces occur in response to specific hydrodynamic and sedimentological drivers; these are summarised in Table 2.1. These distinct morphologies (convex-up and concave-up) have been related to the occurrence of Lagrangian asymmetries where an idealised equilibrium cross-shore profile will occur when the spatial distribution of bed shear stress is uniform and there is no gradient in suspended sediment and asymmetries in sediment dispersal (Friedrichs and Aubrey, 1996; Friedrichs, 2011; Mariotti and Fagherazzi, 2013a). Analytical techniques have been used to show that this equilibrium results in a convex profile when tides dominate and a concave profile when waves dominate (Friedrichs and Aubrey, 1996; Friedrichs, 2011). Although these approaches to explaining intertidal curvature and infilling processes are consistent with observed

intertidal profile shapes (i.e. driven by cross-shore transport) (e.g. Kirby, 2000; Bearman et al., 2010), they neglect the influence of estuary-wide processes and circulation arising from Eulerian tidal asymmetry (from non-linear feedbacks between tidal velocities and morphology) and wind circulation (which can cause lateral transport). Moreover, waves are often treated in isolation from the wind that generates them (e.g. as in Mariotti and Fagherazzi's (2013a) model). Ideally, the equilibrium conditions that lead to the emergence of particular stable estuary geometries should be studied by including both Lagrangian and Eulerian processes, and waves should not be studied in isolation from advective currents. Currents in a real estuary are modulated by the wind and waves (Henderson and Mullaney, 2013), and so the asymmetries will be sensitive to the wind-direction, the fetch, as well as the depth and shape of intertidal flats, which has not been explored in detail.

Here, we use hydrodynamic modelling within a series of idealised estuaries that represent estuaries in different stages of infilling to show how wind and the resultant wind-waves interact on an estuary-wide scale to control the asymmetry. Although we do not include freshwater input, our methods could be extended to include baroclinic circulation, and so we will continue to use more general term 'estuary' throughout the paper even though our study is more correctly representative of a tidal basin with small freshwater input which are common in Australasia (e.g. Hume et al., 2007) and eastern U.S.A, but less common in northern Europe. Our results show that alignment of the morphology relative to prevailing wind should be considered as a morphologically significant factor in shaping the resultant sediment transport pathways, and as the estuary 'ages' through infilling. This fetch-aligned effect becomes increasingly important in controlling the final pathway toward an emergent salt-marsh.

2.2 The influence of Eulerian and Lagrangian asymmetry on tidal-stage relationships

Figure 2.1, case 1, shows a schematic illustrating the expected changes to bed shear stress τ averaged over the estuary (where τ is controlled by variations in depth-averaged current speed) as the water level changes with the tide ('the tidal stage relationship') in an idealised estuary which is dominated by Eulerian tidal

asymmetry, where the ebb and flood tides have different magnitudes or durations. The bed shear stresses that occur on the flood and ebb tides are plotted in the negative and positive directions respectively, with the critical shear stress τ_c marked with a dashed vertical line. The distortion of the tide within an estuary that causes Eulerian asymmetry has been related to the influence of estuarine morphological characteristics on the propagation speed of the tidal wave (Boon and Byrne, 1981; Dronkers, 1986; Speer and Aubrey, 1985; Friedrichs and Aubrey, 1988; Pethick, 1994; Wang et al., 2002; Prandle, 2003; Fortunato and Oliveira, 2005; Moore et al., 2009; Brown and Davies, 2010; Colby et al., 2010; Bolle et al., 2010; Friedrichs, 2010). In a shallow estuary with few or absent intertidal flats, flood dominance (larger velocity during the flood tide) occurs because the width-averaged depth is greater during the passage of the crest of the tidal wave (high water, HW) than the trough (low water, LW). The resulting shorter flood duration (and longer ebb duration) causes greater maximum speed during the flood (Speer and Aubrey, 1985; Friedrichs and Aubrey, 1988; Friedrichs, 2010). Conversely, in an estuary with shallow, extensive tidal flats and a proportionally deeper channel, the width-averaged depth is smaller at the peak of the tidal wave (HW) compared with the trough (LW) resulting in a slowing of propagation speed and a corresponding decrease in the length of the ebb stage, resulting in ebb dominance (greater peak speed during the ebb tide) (Speer and Aubrey, 1985; Friedrichs and Aubrey, 1988; Fortunato and Oliveira, 2005). The stage of the tide (flood or ebb) during which the larger current speed occurs (the Eulerian asymmetry) can be predicted using the following tidal asymmetry parameter (Friedrichs, 2010; van Maanen et al., 2013a):

$$T = \frac{\alpha}{\langle h \rangle} - \frac{1}{2} \frac{\Delta b}{\langle b \rangle}, \quad (2.1)$$

$$\Delta b = b_{HT} - \frac{b_{LT}}{2}, \quad (2.2)$$

where α is the amplitude of the tidal wave, $\langle h \rangle$ is the average channel depth relative to mean sea level, where $\langle \rangle$ indicates a mean over the estuary and over a tidal cycle, $\langle b \rangle$ is the average estuary width at mean sea level, b_{HT} is estuary width

at high water and b_{LT} is the estuary width at low water. If $T > 0$ then the width of the estuary does not increase significantly between low and high water, therefore the distortion of the tide is dominated by changes in channel depth, and the crest of the tidal wave (HW) can travel faster than the trough (LW) resulting in a faster flood tide and flood dominance. When $T < 0$, the width of the estuary is significantly greater at high water compared with low water due to the presence of intertidal flats, salt-marsh or mangroves and therefore the distortion of the tide is dominated by changes in estuary width. This distortion slows the peak (HW) of the tidal wave relative to the trough (LW) resulting in a faster ebb flow and ebb dominance. When the tidal wave is progressive, the tidal asymmetry within the intertidal and subtidal areas can be different; in such a case, the flood currents occur nearer high tide, so the intertidal area (which is only inundated near high tide) will only experience flood currents and will be flood dominant (Bowers and Al-Barakati, 1997).

Figure 2.1, case 2, illustrates the expected distribution of estuary-averaged τ (which can be due to tidal currents), τ_w (due to wave orbital currents) or τ_{max} (due to a combination of both tides and waves) with changes in water level, where the duration over which τ is below τ_c changes at high tide. The time over which τ falls below τ_c during slack water (the ‘slack water duration’), will control the amount of sediment settling out of the water column and deposition to the seabed (Dronkers, 1986; Bolle et al., 2010; Friedrichs, 2011). A case when the duration over which $\tau < \tau_c$ is longer at high tide compared with low tide is presented in Figure 2.1, i.e. case 2, left panel. The reverse scenario is presented in Figure 2.1, case 2, right panel. In an unfilled estuary, deeper water over intertidal areas at high water (which also relates to $T > 0$ in equation 2.1) corresponds to lower velocities at high water and therefore increases the duration of slack high water. This increase in slack water duration around high water promotes settling of sediment and infilling over intertidal areas (Figure 2.1, case 2, left panel). Conversely for an infilled estuary, intertidal flats (including vegetated areas) result in a greater total estuary width at high water compared with low water ($T < 0$ in equation 2.1) allowing greater water movement around high water compared with low water and which reduces the slack water duration and limits the settling of fine sediment at high water (Figure 2.1, case 2, right panel). It is also possible

that the effect of friction around high tide in the infilled estuary would be greater than in the unfilled estuary (due to shallower water depths over the intertidal) which would reduce the strength of the tidal currents around high tide slack water (Figure 2.1, case 2, left panel).

The spatial variation of τ due to the relative importance of tidal currents over the deeper areas and wave orbital currents over the intertidal areas results in a Lagrangian asymmetry (Figure 2.1, case 3), whereby a spatial gradient in hydrodynamic energy and therefore suspended sediment results in sediment being advected from areas of high concentration to low concentration (Friedrichs, 2011; Mariotti and Fagherazzi, 2013a). Tidal currents tend to produce largest shear stresses over the lower, deeper intertidal areas whereas waves create the greatest shear stresses over the shallower intertidal areas. This gradient results in a shoreward decrease of suspended sediment concentration and transport during fair weather (tides only, Figure 2.1, case 3, left panel) and a seaward decrease and transport during windy weather (tides and waves, Figure 2.1, case 3, right panel) (Jannsen-Stedler, 2000). As waves increase the average shear stress at high tide, they are also capable of reducing the duration of time around slack water over which $\tau < \tau_c$ relative to the case with no waves (case 2, right panel). Residual circulation, such as can be driven by the wind, would modify Eulerian asymmetries (case 1), and create spatial differences in shear stress (case 3).

2.3 Methods

2.3.1 Model setup

Idealised modelling techniques employ simplified model grids which, despite schematisation, aim to represent the fundamental characteristics of a natural system. The benefits of using an idealised modelling approach are that the simplified system can be systematically manipulated to test hypotheses, while the reduced complexity enables a reduction in processing time. Here, flows in four different synthetic tidal estuaries were simulated using the Delft3D hydrodynamic numerical modelling software coupled to the SWAN shallow water spectral wave model.

The Delft3D modelling package is a hydrodynamic numerical model developed by Deltares. Delft 3D is split into a series of interacting modules; the modules used within this research are Delft3D flow and Delft3D wave. Delft3D flow solves the unsteady shallow water equations on a staggered grid and can be either used to simulate 3D or 2D hydrodynamic flows and it is used here in depth-averaged (2D) barotropic mode (Lesser et al., 2004). Delft3D flow is able to simulate the flooding and drying of intertidal flats and therefore is well suited to modelling estuarine hydrodynamics.

Delft3D wave uses SWAN which solves for the evolution of the wave field using the wave action balance equation. The model includes the processes of wind-generation, refraction, non-linear wave-wave interaction and dissipation through white-capping, bottom-friction and depth induced breaking (Booij et al., 1999) so that the model is able to replicate the non-monotonic relationship between τ_w and depth observed over the intertidal areas of estuaries (Fagherazzi et al., 2006 and 2007). Delft3D wave is coupled to Delft3D flow so that the both the effects of flow on waves and the effects of waves on flow are represented in the model. This dynamic coupling allows the replication of set-up, current refraction of waves and enhanced turbulence. This coupling of waves and flow allows accurate simulation of τ due to currents, τ_w due to waves and τ_{max} due to waves and currents combined.

The model (Figure 2.2) was set up with a 50 m grid cell size (on a rectangular grid) and forced by an astronomical M_2 tide at the seaward boundary which was situated 5 km away from the estuary mouth (Figure 2.2). To assess the interaction of tides, wind and waves, three sets of model runs were executed, firstly forced by tides only (Delft3D hydrodynamic module only), secondly by a spatially uniform and constant winds of 5 and 10 m/s in both a westerly (landward) and easterly (seaward) direction (using the Delft3D hydrodynamic module coupled to the SWAN model). Finally, to isolate the influence of wind (without waves or tides) on circulation, the model (Delft3D hydrodynamic module only) was run with a steady high water sea level (i.e. no tides, but with the intertidal fully inundated) and a spatially uniform and constant wind of 10 m/s in both a westerly (landward) and easterly (seaward) direction.

A uniform bottom friction Manning coefficient of $0.035 \text{ s/m}^{1/3}$ was applied throughout the model; this value is representative of fine sand bed material (Bolle et al., 2010). Each scenario was run for 4 tidal cycles after an equilibration period of 1 tidal cycle. Within these schematised models Coriolis effects were not included; the small scale of the estuaries compared to the calculated Rosby Radius substantiates this approach.

2.3.2 Construction of idealised estuaries

Four simplified ellipsoidal estuarine basins were designed to reproduce the fundamental characteristics and geometry of a short, shallow, barrier-enclosed, mesotidal estuary basin experiencing different stages of infilling. Each synthetic estuary had the same plan shape (and consequently fixed fetch of around 5 km at high tide) and overall channel thalweg depth (5 m below mean sea level) but different morphology, which was controlled by varying the height and extent of the intertidal areas. The resulting intertidal morphologies ranged from convex and shallow (infilled) and concave and deep (unfilled) relative to mean sea level.

Previous idealised modelling studies have generally schematised the intertidal area using either linear (Friedrichs and Aubrey, 1988; Pritchard; 2005; van Maanen et al., 2013a) or a stepped representation (Brown and Davies, 2010; Mariotti and Fagherazzi, 2013a). Both of these approaches are advantageous in their simplicity but bear little resemblance to the curved profile (concave or convex) of natural intertidal systems which is related to wave-bed shear stresses and intertidal storage (which controls slack-duration). Here we use an alternative approach for schematising the estuary-wide intertidal morphology for the purposes of idealised modelling using hypsometric parameters. Hypsometry allows the characterisation of topography or bathymetry by relating estuary area to elevation or depth (Strahler, 1952; Boon, 1975; Boon and Byrne, 1981; Eiser and Kjerfve, 1986; Friedrichs and Aubrey, 1996; Wang et al., 2002; Moore et al., 2009) as defined by the following equations:

$$\frac{a}{A} = \frac{G}{[r + G(1-r)]} \quad (2.3)$$

and:

$$G=(1-h/H)^{\gamma} \quad (2.4)$$

where h is the height above the minimum estuary elevation, A is the maximum estuary area at high tide, a is the estuary area lying above height h , H is the height between lowest and highest estuary elevation (mean sea level is $h=H-\alpha$). The empirical parameter $r = 0.01$ represents the estuary curvature and is based on the slope at the point of inflection (Boon and Byrne, 1981).

The area below the hypsometric curve (controlled by the parameter γ) corresponds to the volume of sediment in the estuary and hence provides an indication of the maturity and the degree of convexity (or amount of sediment infilling) within the estuary. Observations show that an immature, concave, un-filled estuary will have γ values ranging between 3.5 and 5, and a more mature, convex, infilled estuary with a high intertidal area will have γ values ranging between 1.8 and 2.0 (Boon and Byrne, 1981; van Maanen et al., 2013a). The application of hypsometry to the elliptical estuary template was used to create four estuary morphologies ranging from morphologically ‘young’ and unfilled (concave-up estuary) through to ‘mature’ and sediment filled (convex-up estuary) all with the same overall length (and therefore fetch at high water) and thalweg depth. The size of the entrances to the synthetic estuaries was controlled by the relationship between the tidal prism and mouth cross-sectional area of the entrance, which is well described by the empirically derived O’Brien ratio (O’Brien, 1969; Jarrett, 1976, Gao and Collins, 1994; Townend, 2005):

$$M = 7.01 \times 10^{-5} P, \quad (2.5)$$

where M is the cross-sectional area of the mouth, evaluated relative to mean sea level, and P is the tidal prism. The form of the O’Brien relationship used here was derived by Townend (2005) based an analysis by from an extensive dataset (108 inlets) in the US on the Atlantic, Pacific and Gulf Coasts (Jarrett, 1976). The O’Brien relationship was further investigated for 82 NZ estuaries (including Raglan Harbour) (Hume and Herdendorf, 1993) and 75 UK estuaries (Townend, 2005) and a similar relationship between cross sectional mouth area and tidal prism was found to be applicable, with scatter in the datasets attributed to estuary type and geomorphological setting with different estuarine types exhibiting

slightly different relationships (Hume and Herdendorf, 1993 and Townend, 2005). As the objective of the idealised estuary modelling was to represent not only the specific situation at Raglan but also more general representation of estuary morphology the relationship of Townend (2005) was used as it provided a general relationship based on a diverse dataset. The comparison of the schematic geometries using both equations 2.1 and 2.5 is summarised in Table 2.2 and the two extreme hypsometric forms ($\gamma = 4.0$ and $\gamma = 1.8$) tested are summarised in Figure 2.3 in both plan and cross-section. Both Table 2.2 and Figure 2.3 show that increasing the infilling parameter (γ) reduces the area of the estuary at mean sea level (MSL) whilst maintaining the overall fetch at HW and the absolute depth of the main thalweg. This increase in γ also changes the channel shape in the sub-tidal, increasing the mean depth relative to MSL and in the intertidal, reducing the mean depth resulting in a slowing of the tidal crest (HW) relative to the trough (LW) and a shortening of the ebb phase of the tide thereby increasing ebb dominance (Equation 2.1).

Throughout these idealised experiments, the morphology was fixed rather than coupled to a morphological model and updated. The advantage of this approach is that it allows the control of the depth and extent of tidal flats on hydrodynamics to be determined in a systematic way. Using morphologies that reflect empirical studies of natural geometries allows a focus on the hydrodynamics rather than on whether realistic morphologies are being produced by the many assumptions used in the morphological models (e.g. grain size distributions, entrainment properties of cohesive sediments, compaction, flocculation processes) (Coco et al., 2013). The drawback of this approach is that the series of tested morphologies cannot be considered as a morphological progression of the same estuary from ‘young’ to ‘mature’ but instead as a series of discrete case studies and therefore the pathway toward establishing dynamic equilibrium within an estuary can only be inferred from the modelled hydrodynamics. All the modelled scenarios are summarised in Table 2.3.

2.3.3 Case study

Outcomes from the idealised modelling were compared with the observations from a barrier-enclosed estuary with a narrow entrance and similar tidal range.

Whaingaroa (also known as Raglan) Harbour is a mesotidal (~3 m) dendritic estuarine system situated on the west coast of the North Island in New Zealand (Figure 2.4). The estuary's dendritic morphology results in two arms (the Waitetuna in the south and Waingaro in the north) which have different fetch relative to the prevailing wind direction (from the southwest). These two arms have different variations in intertidal depth and area despite a similar tidal range, sediment supply (Griffiths and Glasby, 1985; Elliott et al., 2008; Kotze et al., 2008; McKergow et al., 2010; Hicks et al., 2011) and historic rate of mean sea level rise (Hannah, 2004).

2.3.3.1 Morphology

The bathymetry of Whaingaroa Harbour was created from LiDAR (flown on behalf of Environment Waikato 2010), bathymetry surveys (single beam, collected in 2008 and 2009) and navigation charts (LINZ chart NZ4421). The morphologies of northern (Waingaro) and southern (Waitetuna) arms of the harbour are summarised in Figure 2.4c as basin-wide hypsometric curves plotted alongside the idealised estuary hypsometries. This comparison shows a distinct difference between the two arms of the harbour with the northern fetch-aligned arm (Waingaro, thick solid line) exhibiting deeper water levels over the intertidal flats (relative to MSL) with a slightly concave form and the sheltered southern arm (Waitetuna, thick dashed line) showing shallower water levels over the intertidal (relative to MSL) and a more convex intertidal shape. This pattern of infilling is supported by sedimentation evidence from cores and accretion plates which show that the southern (Waitetuna) arm has experienced sedimentation rates ranging from 0.35 mm/yr prior to human settlement increasing to 1.1 mm/yr since 1890 (following deforestation) and further increasing to 2.5 mm/yr since the early 1990s (Swales et al., 2005). In direct contrast, the northern (Waingaro) arm has experienced almost no sedimentation for at least the last 150 years (Swales et al. 2005). The large spatial variation in sedimentation between the two adjacent arms has been attributed to the northern (Waingaro's) exposure and orientation to the prevailing south westerly winds with the short period waves preventing the deposition of sediment above a critical intertidal height, a process that has been replicated in this idealised modelling investigation.

2.3.3.2 Hydrodynamics

To compare the asymmetry in the idealised modelling to the Whaingaroa harbour, the model was forced with a 1.5 m amplitude M2 tide imposed at the seaward boundary (equivalent to a spring tide for Whaingaroa Harbour) both with and without wind and waves. No freshwater input was included in the model. The hydrodynamic model only replicated locally generated short period waves as although the Tasman Sea experiences large amounts of swell the propagation of this swell into the estuary is limited through breaking and dissipation on the extensive ebb tidal data at the estuary mouth (Figure 1.1j). Furthermore, the arms of the estuary which form the main focus of this study are situated further up estuary and are therefore further sheltered from oceanic swell.

2.4 Results

To highlight the complex sediment transport patterns potentially arising from both Eulerian and Lagrangian asymmetries, the bed shear stresses are presented in a way that summarises this complex data in a manner similar to the conceptual diagrams shown in Figure 2.1. To compare the relative potential contribution of tides and waves to sediment mobilisation and transport, bed shear stresses (τ) were calculated for the tidal model and the tide and wind model; and combined maximum bed shear stresses were calculated for the tide, wind and wave model (τ_{max}). Averaging over areas of equal water surface elevation η rather than over time and space, was performed to allow for the phase shift (and sloping water level) across the domain, for example a water level of $\eta = 0$ includes data from slightly different time periods (maximum time difference ~ 10 minutes). The results are presented separately for the subtidal and intertidal areas of the estuary.

2.4.1 Tidal model

To assess the relative contributions of Eulerian and Lagrangian asymmetries, we consider the solid line in Figure 2.5 as an example of the asymmetry that occurs in the idealised estuary ($\gamma = 2$) with the model forced by tide only. The overall classification of the estuary is ebb-dominant because the maximum (and average) ebb shear stress, τ , is greater than the flood τ , both in the intertidal and the subtidal area (which indicates Eulerian asymmetry). This classification is apparent in the

cross section (Figure 2.5a) and the spatially-averaged τ plots (Figures 2.5c, d) where the larger time-averaged τ occurs on the ebb phase. This relatively simple interpretation is complicated slightly by the different patterns of flooding and drying over the subtidal and intertidal areas. In subtidal regions (Figure 2.5c), the estuary is always underwater and therefore always ebb dominant. In the intertidal region, the dominance switches between ebb-dominant in the deep intertidal and flood-dominant in the shallow intertidal (Figure 2.5a). Therefore, at mid tide (water levels around $\eta = 0$), only the lower intertidal region is inundated and the intertidal average is ebb dominant, but as the tide reaches its maximum (e.g. $\eta \geq 1.5$), the intertidal average becomes flood-dominated. The shape of the curve indicates that the tide is somewhere between standing and progressive and this variation in timing of maximum bed shear stress (at around 1.5 m during the flood and around 1 m during the ebb) contributes to the increase in flood-dominated asymmetry over the shallower parts of the intertidal. The flat shape of the curve at high tide ($\eta \sim 2$) indicates a short slack duration over both the intertidal and subtidal regions and therefore there is little time available for fine sediment to fall out of suspension (as in Figure 2.1, Case 2, right panel). Finally, the potential direction of fine sediment transport due to advection (Figure 2.1, Case 3) is shown by the large difference in bed shear stress over the intertidal and subtidal areas of the estuary with advection occurring towards areas of lower bed shear stress (the intertidal in this case).

In summary, the Eulerian asymmetry in this tide-only example is ebb-dominant in the channel and lower reaches of the intertidal, and flood dominant in the upper reaches. This asymmetry pattern will scour the coarser fractions from the channels and move sediment away from the lower intertidal, contributing to flattening of the intertidal and the continued development of the characteristic tidal flat morphology. However, the Eulerian flood dominance on the intertidal is small, and the Lagrangian asymmetries are likely to dominate over this pattern by advecting finer sediment continually onto the tidal flats (since the shear stress is so much lower on the intertidal flats than in the channels), but not allowing it to settle until it is nearly at high tide (the shear stresses on the intertidal do not slacken until just before high tide). This deposition pattern will continue the

process of gradual shallowing and flattening of the intertidal while the Eulerian-driven deepening of the channel occurs.

Overall, the patterns in τ over the intertidal and subtidal were consistent for all four morphologies with a transition from flood to ebb dominance with increased tidal flat elevation (Figures 2.5a, b). The increase in the maximum τ during the ebb relative to the flood is due to the tidal wave crest (HW) slowing relative to the trough (LW) with an overall decrease in the average estuary depth at high tide that accompanies an increase in elevation and extent of the intertidal area. This distortion of the tidal wave in turn reduced the time between HW and LW (the ebb) and hence increased maximum ebb speed and therefore τ (as predicted by equation 2.1). Over the intertidal area of the estuaries (Figure 2.5c), although the pattern of τ is similar to that measured over the subtidal part of the model (Figure 2.5b), the timing of the peak τ shows that the tidal wave is slightly more standing than in the channel. This distortion of the tidal wave along with the patterns of flooding and drying over the intertidal areas results in different Eulerian asymmetries within the shallow and deep parts of the infilled estuaries ($\gamma = 1.8$ and $\gamma = 2$). A similar pattern of contrasting tidal asymmetry due to a partially progressive tidal wave (termed “tidal rectification”) has been recorded and modelled in the Conwy Estuary (Bowers and Al-Barakati, 1997).

There is an overall reduction in τ between the unfilled ($\gamma = 4$, dot-dashed line) and infilled ($\gamma = 1.8$, dotted line) estuaries (Figure 2.5). This reduction is due to a decrease in the tidal prism and an increase in friction over the relatively shallower intertidal flats (with infilling) and a corresponding decrease in depth-averaged velocities. A change in the timing of maximum velocity and τ is also apparent with the maximum ebb τ occurring later and the maximum flood τ occurring sooner; this change is due to the shifting distribution of depth in the intertidal and associated decrease in the estuarine cross-sectional area (Figure 2.5b) towards the higher part of the estuary (with infilling). It is interesting to note that the time when the maximum ebb speed occurs is when the water level is at the convex inflection point of the topography (which is at the lower limit of the intertidal area (e.g. Figure 2.5b, dotted line at 1 m), whereas the time when the maximum flood tide occurs is when the water level is at the concave inflection

point of the intertidal area (e.g. Figure 2.5b, dotted line at 1.8 m). Therefore, slowing of the flood current occurs as the water moves up over the lower edge of the tidal channel, and then increases as the water floods the tidal flat. Conversely, the ebb flow only moves quickly as the water drains off the tidal flat. The change in the timing of the maximum depth-averaged velocity (and also τ) toward high tide reduces the duration and timing of slack water when the morphology becomes more infilled, therefore potentially reducing the volume of sediment deposited around slack high water. For both the unfilled and infilled estuary basins, the greatest τ occurs over the subtidal regions of the model (note change in scale in Figures 2.5c, d) indicating the potential for landward sediment transport regardless of the estuary morphology.

In summary, the Eulerian asymmetry shows a progressive change from flood to ebb dominance as the estuary basin infills. However, this pattern is not spatially uniform throughout the estuary with the shallow intertidal areas remaining flood dominant despite infilling. The curvature around high water (in Figures. 2.5c, d) shows that the unfilled estuaries have a longer slack duration at high water than the infilled estuaries indicating that the infilling rate would slow as the estuary infilled. The difference in bed shear stress between the intertidal and subtidal remains almost constant with infilling, showing that the potential for landward transport due to sediment advection (Figure 2.1 Case 3) is not changed.

2.4.2 Tides, Winds and Waves

The complexity of the resultant pattern of tidal asymmetry is enhanced when wind and waves are included. This complexity is due to the interaction of the water circulation (predominantly from tides and wind), the stirring influence of waves (which changes the bed-shear stress on the intertidal) and the intermittent flooding and drying of the intertidal areas.

Firstly, the influence of wind on circulation patterns was tested using a wind-only model (i.e. no tide or waves and a steady water surface fixed at high water), with the wind blowing directly along the estuary both toward and away from the entrance. This scenario caused a steady circulation pattern with depth-averaged velocity over the intertidal areas in the same direction as the wind until the end of

the estuary where flow returned into the deeper subtidal channel against the prevailing wind direction (Figure 2.6a-d). The wind-driven currents are greater over the intertidal area of the infilled estuary compared with the unfilled estuary; this is because the current speeds tend to be greater over shallower areas and the infilled estuary has a greater proportion of higher intertidal level. The larger currents in the shallower estuary probably occur because inertia is larger in the deeper estuary. This wind circulation pattern is consistent with that modelled and recorded elsewhere (Sanay and Valle-Levinson, 2005; Narváez and Valle-Levinson, 2008) and occurs as a result of increased flow with the direction of the wind in shallower areas driven directly by the wind stress and increased flow against the wind in the adjacent deeper subtidal areas, driven by the resultant barotropic pressure gradient.

When both tides and wind are included within the numerical model, the wind circulation pattern described above has a marked impact on the resultant tidal asymmetry due to changes in depth-averaged velocities. These changes are presented in a similar format to both the idealised case (Figure 2.1) and the tide only model (Figure 2.5). During landward winds, the circulation pattern identified in Figures 2.6b and d occurs, and therefore the wind enhances intertidal depth-averaged velocities during the flood tide and opposes (and slows) depth-averaged velocities during the ebb tide (Figures 2.7a, d, e, h). The return current along the subtidal channel enhances depth-averaged velocities against the wind and weakens depth-averaged velocities with the wind (Figures 2.7a, c, e, and g). Under a seaward wind, the effect is reversed. This transverse flow pattern is most apparent in the transect plots (Figures 2.7a, e) because Figures 2.7c, 2.7d, 2.7g and 2.7h are averaged over the entire estuary. The transect plots also shows the existence of a steady null point around which the transverse flow strengthens and weakens depending on the wind direction and strength (Figures 2.7a, e).

For all estuaries, the seaward (ebb) enhancement of currents over the subtidal channel due to an up-estuary (westerly) wind is greater than the landward (flood) enhancement due to a down-estuary (easterly) wind. This pattern occurs because the circulation is enhanced by setup and return currents and the potential is greatest when the prevailing wind is pushing the water against the closed end of

the estuary. When the wind is being pushed against the open end of the estuary (the mouth) then setup and return currents are reduced due to the water exiting through the mouth into the open sea.

The most dramatic impact of the addition of wind-generated waves is to the Lagrangian asymmetry, changing both the length of time that $\tau < \tau_c$ (around high slack water), and the increase in overall bed-shear stress over the intertidal areas. Wind-forced waves predominantly affect the seabed sediments through wave orbital velocities. Although these orbital velocities only result in a small net transport due to net orbital velocity asymmetry, they are capable of suspending sediments, which can then be transported by mean currents to less hydrodynamically-active areas for deposition (Figure 2.1). As sediment entrainment will occur as a result of both tidal and wave currents, we consider the resultant hydrodynamic forcing on the seabed as a combined τ_{max} from both waves and currents (Figure 2.8). The information in Figure 2.8 cannot be used to assess the tidal asymmetry and direction of sediment transport due to the dominant current velocities (Figure 2.1, case 1) because the orbital velocity component is oscillatory and therefore, unlike tidal currents, does not have a net direction of sediment transport. Instead Figure 2.8 can only be used to assess the tidal asymmetry arising from the length of slack duration (Figure 2.1, case 2) and sediment advection (Figure 2.1, case 3).

To interpret the various types of Eulerian and Lagrangian asymmetries, we consider the dot-dashed line in Figure 2.8b and c as an example of the asymmetry that occurs in the unfilled idealised estuary ($\gamma = 4$) with the model forced by tide, a 10 m/s westerly (landward) wind and waves. The slope of the dot-dashed line at high tide ($\eta \sim 2$) in Figure 2.8c shows that although τ_{max} reduces towards high tide, on average across the estuary, the onset of slack water does not occur in the intertidal under this scenario and therefore there is little time available for fine sediment to fall out of suspension. This reduction in slack water occurs because the orbital velocities generated at high tide (also maximum fetch) prevent the deposition of sediments at high water (as in Figure 2.1, Case 2 right panel); this situation is in direct contrast to the tide only scenario (Figure 2.5d) and the difference can be directly attributed to the inclusion of waves in the model. The

potential direction of fine sediment transport due to advection (as in Figure 2.1, Case 3) is shown by the difference in τ_{max} over the intertidal and subtidal areas of the estuary with advection occurring towards areas of lower τ_{max} . Under the tide only scenario (Figures. 2.5c, d) the pattern of τ over the intertidal closely mirrors that over the subtidal. However, when waves are included, because the orbital velocities have more influence over the relatively shallower intertidal, the pattern of τ_{max} differs considerably between the intertidal and subtidal areas. When τ_{max} over the intertidal exceeds τ_{max} over the subtidal area at high tide (Figures. 2.8b, c) sediment advection will be in a seaward direction. In summary, the addition of waves in this example is unlikely to affect the Eulerian asymmetry due to the oscillatory nature of the orbital velocities. However, the disproportionate influence of the waves over the relatively shallower intertidal area results in a net sediment advection in a seaward direction at high water and a shortening of slack water to a point where sediment deposition is not possible over the intertidal areas (depending on sediment grain size). This advection will result in limited sediment transport onto the intertidal areas and a possible reversal in fine sediment transport around high tide compared with tidal processes alone.

In Figure 2.9, the potential for deposition in the intertidal area is presented as the percentage of grid cells for which $\tau_{max} < \tau_c$ at any moment during the tidal cycle. The potential is presented as a percentage, allowing a simple comparison of the results for all wind conditions and morphologies in one figure. The subtidal channel is relatively deep compared with the extent and influence of the orbital velocities, so waves have very little influence on seabed sediments and therefore transport in this region is dominated by only the tidal regime and consequently patterns of tidal asymmetry. In all cases, the addition of even small winds enhanced the maximum bed shear stress and caused significant portions of the intertidal to be areas of potential erosion (Figures. 2.8, 2.9a, c, d, f, g), although a clear distinction can be made between the deeper unfilled ($\gamma = 4$ and 3) and the infilled ($\gamma = 1.8$ and 2) estuaries, with the infilled estuaries being more sensitive to lower wind speeds.

The orientation of the estuary relative to the prevailing wind direction and the overall morphology of the estuary is critical to the resultant distribution of τ_{max} . In

the ‘young’ unfilled morphologies ($\gamma = 3$ and $\gamma = 4$), the intertidal zone is on average deep relative to MSL (Figure 2.5a). This deep and wide intertidal morphology increases the fetch length early on as the water level rises, so that a relatively large fetch length is attained early in the flooding tide and is maintained late into the ebbing tide. During both moderate (5 m/s) and strong (10 m/s) wind speeds the relatively large fetch at mid-tide combines with the peak tidal velocities to form a peak maximum bed shear stress at mid-flood and mid-ebb across much of the intertidal. At high tide, the deeper morphology attenuates the orbital velocities resulting in a period of slack water over the deeper intertidal areas. This effect is especially apparent during the moderate (5 m/s) wind speed; the stronger wind speed (10 m/s) is able to overcome some of this attenuation due to an increase in the strength of the orbital velocities (Figures. 2.8, 2.9a, c and d). Within the more infilled morphologies ($\gamma=1.8$ and $\gamma=2$), the intertidal is on average shallow with much of the intertidal area above mean sea level. Under this morphological scenario, a large fetch is reached later in the tidal cycle resulting in orbital velocities having their maximum around the time of high water. With this shallow water depth, the orbital velocities are able to reach the seabed during even moderate wind speeds (5 m/s) causing significantly enhanced bed shear stress during slack water and inhibiting the deposition of sediments which would occur in the absence of waves (Figures. 2.9a, f, g). This lack of deposition around the estuary margin is consistent with the recorded band of highly turbid water (the turbid fringe) attributed to waves breaking in shallow water within Manakau Harbour, New Zealand (Green et al., 1997, 2000). Overall, the probability of the intertidal flats accreting changes from nearly certain under a tidal scenario, to very unlikely with the addition of wind and waves. Therefore, there is a theoretical critical threshold of morphological development when weak winds switch from ineffective to effective erosion mechanisms. The timing of this maximum bed shear stress throughout the tidal cycle can also be seen in Figures. 2.7c and 2.8c, with a distinctive peak in maximum combined bed shear stress occurring at around mid-tide for the $\gamma = 4$ morphology and at around high water for the $\gamma = 1.8$ morphology.

When compared with the tide only scenarios (Figure 2.5), the tide, wind and wave scenarios (Figure 2.8) result in higher τ_{max} over the intertidal with similar

magnitudes to those experienced over the subtidal area. This increase in intertidal τ_{max} relative to that over the subtidal area is partly due to increased water movement from wind induced circulation but mainly due to the shear stress contributed by wave action and would result in either a reduction in the spatial gradient of suspended sediment concentration or a complete reversal leading to either a weakening of shoreward sediment transport or a switch to seaward transport during periods of increased wave activity.

2.4.3 Case study

The modelled hydrodynamics in each arm of Whaingaroa Harbour were summarised in a similar manner to the idealised estuaries for tides only (Figures. 2.10a, d) and for tides, wind and waves (Figures. 2.10b, c, e, and f).

The tide-only model shows a similar relative distribution of tidal energy in comparison to the idealised case with a similar hypsometry. The less infilled northern (Waingaro) arm (Figure 2.10a) shows a slightly stronger flood maximum velocity and slightly weaker ebb than the more infilled southern arm (Figure 2.10d) (Waitetuna), and both of these maxima occur closer to low tide in the northern arm than in the southern arm, indicating a longer period of slack duration in the northern arm. The distribution of bed shear stress is typical of the $\gamma = 3$ idealised estuary (Figures. 2.5c, d, dashed line) consistent with the hypsometry of the estuary which falls between $\gamma = 3$ and $\gamma = 2$ (Figure 2.4c). For the more infilled southern arm, the estuary is slightly ebb dominant (Figure 2.10d) with the ebb tide occurring earlier in the ebb tidal stage compared with the northern arm (Figure 2.10a). The change in ebb tide timing occurs because there is greater accommodation space over the deeper intertidal flats, increasing velocities and reducing slack water duration, which would inhibit the deposition of sediment on the intertidal flats. This distribution of bed shear stress is similar to the idealised $\gamma = 2$ (Figures. 2.5c, d, solid line) which fits with the hypsometry of the southern arm (Figure 2.4c).

When the model is forced with the prevailing south-westerly wind there is a clear contrast between the response of the fetch-aligned northern arm and the sheltered southern arm to patterns of wind circulation and orbital velocities from waves

(Figures 2.10b, c, e, and f). This modelled scenario demonstrates that despite higher intertidal levels in the southern arm, the combined bed shear stresses due to tides, waves and winds over the intertidal is greater in the fetch aligned northern arm, thereby allowing a greater chance of deposition in the southern arm.

2.5 Discussion

Estuarine hydrodynamics and morphology are linked through non-linear feedback mechanisms and a theoretical stable estuarine morphology should occur at a point where negative feedback mechanisms dominate over positive mechanisms (e.g. Mariotti and Fagherazzi, 2013a). A shift between morphological states occurs when an estuary system moves sufficiently far away from the equilibrium point that positive feedbacks cause a switch into an alternative stable state; the stability of these states (whether positive outweighs negative) is dependent on the resilience of the system to morphological, hydrodynamic and sedimentary pressures and the magnitude of these pressures (McGlathery et al. 2013; Winterwerp and Wang, 2013; Winterwerp et al. 2013). Morphological pressures include anthropogenic intervention (e.g. dredging or intertidal reclamation) (Winterwerp and Wang, 2013) and natural processes (stability and wave attenuation from vegetation, bio-films and shellfish beds) (McGlathery et al., 2013). Hydrodynamic pressures could include either sea-level rise or changes to the wind-wave climate (Fagherazzi et al., 2006; 2007; Fagherazzi and Wiberg, 2009; Townend, 2010; Mariotti and Fagherazzi, 2013a). The stable estuarine form is also dependent on sediment availability (Fagherazzi et al., 2006). Here, we have tested the hydrodynamic pressures that occur over four different estuarine basins in response to changes in intertidal extent, wind strength and wind direction whilst maintaining a constant thalweg depth and tidal range. The idealised scenarios exhibit a strong non-linear relationship between the estuarine morphology design and the tidal asymmetry that results. As the intertidal area was increased in height and volume, the maximum depth-averaged velocity (and τ) in the subtidal channel during the ebb stage of the tide also increased until the ebb tidal velocity exceeded the flood tidal velocity between the $\gamma = 3$ (concave) and $\gamma = 2$ (convex) estuaries. This pattern of tidal distortion suggests the existence of a stable morphological regime (where $T = 0$ in equation 2.1) in which the

maximum depth-averaged velocity (and τ) during the flood and ebb stages of the tide within the subtidal channel are equal in magnitude. Therefore there is no Eulerian tidal asymmetry and no net direction of sediment transport exists. This hydrodynamic response to changes in intertidal morphology agrees with previous studies (Dronkers, 1986; Friedrichs and Aubrey, 1988; Pethick, 1994; Friedrichs, 2010). However, here we show that this relationship does not necessarily hold for the upper intertidal areas where flood current speed always exceeds ebb current speed. The discrepancy between velocities over the intertidal and subtidal areas occurs due to the interaction between the timing of maximum velocity relative to the wetting and drying of the intertidal areas and indicates that, although an equal flood and ebb tide in terms of Eulerian asymmetry (and therefore a stable morphological regime, $T = 0$ in equation 2.1) could exist within the subtidal channel, the same is not true over the intertidal areas within these idealised scenarios.

Wind-generated circulation and waves are more efficient than tides alone at entraining and transporting sediment over intertidal areas by increasing τ by enhanced currents and τ_{max} through wave stirring. The process of wave stirring at high water (when the largest fetch occurs) becomes greater for the more infilled estuaries, when a pronounced reduction in the duration below τ_c occurs between the $\gamma = 3$ (concave) and the $\gamma = 2$ (convex) morphologies (Figure 2.8). This reduction in duration below τ_c indicates that there is an intertidal height (or a critical intertidal height) which is more likely to evolve to a stable intertidal morphology. Below this height, accretion is likely and above this height erosion is likely under a moderate wind speed (5 m/s). Waves have almost no direct impact on the seabed sediments in the subtidal region of the model owing to attenuation of wave orbital velocities in the deeper water depths. In contrast, the stable end-point of the tide only scenario is an emerged salt-marsh.

The stability conditions that are caused by Lagrangian and Eulerian tidal asymmetry can be illustrated by plotting Equations 2.1 and 2.2, evaluated directly for estuaries with the same dimensions as the estuaries used in the idealised modelling, ranging from $\gamma = 1$ (infilled) and $\gamma = 4$ (unfilled) (Figure 2.11a). In agreement with the numerical model, Figure 2.11a shows that unfilled estuaries (γ

= 4) are flood dominant and infilled estuaries ($\gamma = 1$) are ebb dominant with a neutral asymmetry at around $\gamma = 2.5$. However, this equation does not show the effect of wave processes on the stability of the intertidal. To explore this sensitivity, the spatial and temporal distribution of intertidal bed shear stresses due to waves (τ_w) were calculated analytically over idealised estuarine basins over a tidal cycle and averaged, where estuary hypsometries ranged from $\gamma = 1 - 4$, and the wind was assumed to be in a fetch-perpendicular (Figure 2.11b) and fetch-parallel (Figure 2.11c) direction, with wind speeds ranging between 0 and 10 m/s. In this case, fetch-limited wave height and period were calculated using CERC (1984), and bed shear stress is calculated using Soulsby (1997); currents were not included. As γ decreases, the intertidal bed shear stress increases due to the shallowing of the intertidal region allowing greater wave penetration during a fetch-perpendicular (Figure 2.11b) and fetch-parallel (Figure 2.11c) wind direction. However, a point is reached where the intertidal is so shallow that is inundated for only a short time, and the shear stress (averaged over a tidal cycle) decreases with decreasing γ . Therefore, there exists a γ , unique to each wind speed in which average intertidal shear stress is maximised (black circles on Figures. 2.12b, c). When γ is higher than these maxima (less infilled), the morphology should experience a negative feedback when perturbed by increased sediment loading. Infilling with increased sediment loading will decrease γ , which in turn will cause greater τ_w , which will entrain more sediment, and force γ to increase again. Conversely, morphologies with lower γ are inherently unstable, because infilling will cause a reduction in shear stress, and cause a reversal in sediment gradient and a shortening of the period of slack duration at high water. Under light winds (<5 m/s), orbital velocities (and therefore τ_w) are small and therefore the morphology becomes unstable only at an infilled stage ($\gamma = 2$) meaning that the estuary intertidal is able to infill to a moderate level under light winds. Under stronger winds (>5 m/s), orbital velocities (and therefore τ_w) are large and therefore the morphological point of stability would occur at a less infilled stage. Overall this schematic shows that strong winds (and waves) should slow the intertidal infilling caused by Lagrangian asymmetry, and represents the two contrasting processes in the two arms of our case study in the Whaingaroa Harbour.

The non-linear feedback between morphology, wind and hydrodynamics represented in the idealised model and summarised in Figure 2.11 shows that, with a sufficient sediment supply and a constant mean sea level, three alternate estuary states are likely. In an estuary dominated by tides, intertidal accretion will continue due to both Lagrangian and Eulerian processes until the tidal prism reduces to a point at which τ is unable to transport sediment across the intertidal. This quasi-stable high convex intertidal shape will form a deeply incised subtidal channel flushed by ebb dominant Eulerian asymmetry. In an estuary with frequent strong winds (~ 10 m/s in the idealised estuaries), the intertidal area will be deep and concave as intertidal depth is limited by wave stirring during slack water. The slightly concave intertidal profile drives a flood dominant, less incised, subtidal channel (relative to the intertidal height) which is periodically flushed by wind circulation capable of reversing the Eulerian flood asymmetry in the channel. The third stable state is an intermediate state with both tides and less frequent or weaker winds (~ 5 m/s in the idealised estuaries); in this case, the intertidal zone can attain a flat profile, between convex and concave, forming a quasi-stable either weakly flood or ebb dominant main channel which is also influenced by wind circulation. These findings are consistent with those of Mariotti and Fagherazzi (2013a), who found that tides tend to favour the formation of salt-marsh with incised channels whereas waves tend to erase the incisions formed by tides. These processes result in a salt-marsh with deep incised channels (tidally dominated), a tidal flat with channels (tide and waves) and a tidal flat without channels (wave dominated). Our conclusions here extend this regime classification further by considering the non-linear feedbacks between wind circulation and wave-enhanced bed shear stress, estuary morphology and the resultant tidal asymmetry.

The northern (Waingaro) arm of Whaingaroa (Raglan) Harbour is an example of an estuary basin that has reached a stable regime with evidence from cores and sedimentation plates showing no significant long- or short-term sediment accumulation for at least the past 150 years (Swales et al., 2005). Morphological data (described in Section 3.2.1) and hydrodynamic data (Figure 2.12) collected in October and November 2012 using a Sontek ADCP (subtidal) and a FSI (intertidal) (deployment locations are given on Figure 2.4) show an intermediate

regime characteristic of an estuary subjected to a combination of tidal and wave forcing within the idealised model. The intertidal form is relatively flat and situated at an intermediate height as shown by the estuary hypsometry (Figure 2.4). This intermediate intertidal level results in an almost equal flood and ebb velocity with slight variations between spring and neap tides (Figure 2.12), from which we can infer no net long-term preferential direction of sediment flux in the subtidal channel. As the tidal wave is not a perfect standing wave, the flooding and drying of the intertidal flats results in a highly flood dominant intertidal region (Figure 2.12); yet despite this flood dominance, no sedimentation has occurred over the intertidal areas—a factor that must be attributed to the short period wind waves generated within the harbour. Therefore, the presence of these waves is critical to the maintenance of the stable regime observed in the northern (Waingaro) arm, in agreement with the results of the idealised model.

A further distinct hydrodynamic separation between the intertidal and subtidal regions in our idealised modelling arises from the wind-driven circulation which simultaneously strengthens and weakens currents in either area depending on the wind direction, wind speed and the phase of the tide. The clear contrast between the response of the subtidal and intertidal regions to wind (Figures. 2.6a, 2.7a) creates a stable node between the two areas where no change to tidal asymmetry occurs for all wind speeds and directions. This node represents a cross-shore partial exchange barrier to waterborne particles between the subtidal and intertidal, where the wind modifies the tidal current in a different way either side of this node creating a long-shore transverse flow pattern.

The significance of the morphological sensitivity to the wind-wave climate demonstrates that inlets aligned with the predominant wind direction could be reliant on the existing weather patterns as well as the tidal regime to maintain their regime stability. Since weather patterns can be associated with climatic oscillations (e.g. El Niño and La Niña in the South Pacific), it is possible that rates of infilling could change over inter-annual cycles as the patterns of wind speed and direction change. Seasonal cycles in infilling may occur, when wind speed and direction change (e.g. Santa Ana winds in Southern California (Trasviña et al., 2003)) and the daily onset of onshore sea breezes during summer. Distinct

seasonal cycles of mudflat accretion and erosion have been identified in the Severn Estuary, UK, whereby tidal processes cause sediment accretion on mudflats during the summer and waves cause erosion during the winter (O'Brien et al., 2000, Kirby and Kirby, 2008). Although the impacts of future climate change on the wind climate are uncertain, any changes could disrupt the stability of inlets resulting in either erosion in inlets that become more fetch aligned or accretion in inlets that are no longer fetch-aligned. However, inherent uncertainties in future climate change predictions will also result in uncertainties in the prediction of the change in estuarine environments.

The results from the idealised model have allowed us to infer how the relationship between morphology and hydrodynamics influences the resultant morphological stability of the estuary and have produced results which are supported by field observations. However, morphological evolution is complex and involves interactions not only driven by hydrodynamics but by local meteorology, sediment size and composition, underlying geology, freshwater input and the biological and chemical processes that occur in intertidal sediments. Therefore, although these simplified dynamical simulations over restricted geometries have value in inferring the potential drivers of estuarine change within a controlled framework, inevitably there are certain facets of the estuarine system that are not characterised by such a simplified approach.

An important aspect not considered here is the influence of vegetation such as mangroves, saltmarsh, seagrass and biofilms on estuarine stability. For example mangroves can control intertidal stability directly by enhancing sedimentation (van Santen et al., 2007) and indirectly through the modification of hydrodynamics by attenuating waves (Quartel et al., 2007) and controlling flow speeds and direction (Horstman et al. 2013). Mangroves grow above mean sea level (Duke, 1992) and therefore would have a greater influence on the more infilled estuaries tested here and could help maintain the stability of a high convex estuarine shape.

The importance of the wave climate in shaping estuarine morphology could be tested by comparing the hypsometry of estuaries with the fetch axis relative to the prevailing wind direction. If the hypothesis presented in this paper is correct,

estuaries with a fetch axis that is aligned with the prevailing wind direction will show a deeper, more concave form and estuaries with fetches not aligned with the prevailing wind direction will be shallower with a more convex form.

2.6 Conclusions

The aim of this research has been to quantify the hydrodynamic response of different estuary morphologies to forcing from tides, winds and waves. To do this, a series of realistic idealised estuaries and one natural estuary were modelled using Delft3D for hydrodynamics and SWAN for waves to consider the impact of tide, wind and wave forcing. The modelling shows that although infilled estuaries result in ebb dominant asymmetry, tides are a relatively inefficient mechanism of erosion over the intertidal. Depth-averaged velocities (and the resultant bed shear stresses) tend to be quite weak and flood-dominant over intertidal areas. Therefore a stable intertidal flat will not be maintained through a hydrodynamic feedback which involves tidal processes alone, but instead a stable emergent morphology will occur as a result of infilling until tidal currents become too weak to transport sediment; this process might be enhanced through vegetation and biostabilisation of the intertidal area by mangroves or salt-marsh.

Both wind circulation and wave generation have the potential to significantly modify the sediment transport pathways formed by tidal asymmetry with winds modifying the peak velocity (and reversing the direction under certain scenarios) and waves modifying the duration for which the bed shear stress is below τ_c at high tide slack water. Furthermore, orbital velocities from waves are far more efficient at eroding sediments from intertidal areas when compared with tides alone because of their enhanced bed shear stresses. In this case, a stable intertidal morphology will be hydrodynamically maintained by a balance between tidal accretion and wave erosion, with the geometry subtly dependent on the strength of the wind and the fetch. As the height of the intertidal controls the asymmetry of currents in the subtidal channel, a strong wind-wave climate will keep the intertidal in a low, concave form and therefore prevent a switch in tidal dominance from occurring.

In conclusion, given the significant modification of tidal asymmetry by the wind-wave climate, it seems that a repeatable, predictable pattern of sediment flux due to tidal asymmetry is unlikely, even in an averaged sense over a geological timescale. Instead the sediment flux patterns leading to infilling are likely to depend on a combination of the tidal range, strength and seasonality of the wind climate and the orientation of the estuaries' morphology relative to the prevailing wind direction. Therefore the future estuary evolutionary pathway depends not only on the relatively easily predicted tidal regime but also on the less uncertain future meteorological conditions, and this uncertainty is likely to increase with the influence of anthropogenically-induced climate change.

Table 2.1. Comparison of hydrodynamic, sedimentological and biological factors associated with convex and concave up morphologies.

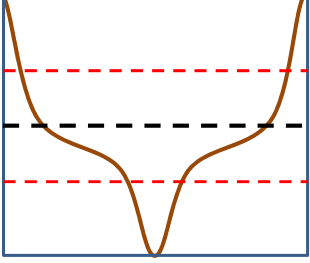
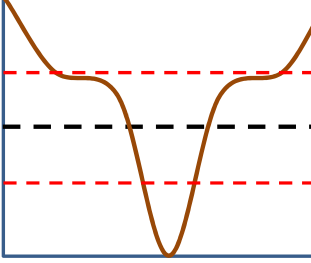
Convex-up	Concave-up
	
Increased tidal range	Decreased tidal range
Decreased wave height	Increased wave height
Increased external sediment supply	Decreased external sediment supply
Bioaggregation	Bioturbation
Bioadhesion	Human disturbance
History of erosion	History of deposition

Table 2.2. Summary of idealised geometries.

Gamma of (level infill)	Measured cross-sectional area below MSL (m²)	Measured tidal prism (m³)	Derived cross-sectional width (m²) (from equation 2.5)	Intertidal shape	Indication of asymmetry direction for Case 1 peak flow (from equations 2.1 and 2.2)	Summary
1.8	565	8068544	642	Convex-up	Ebb	Tidal prism too small and ebb dominant therefore eroding
2.0	650	9272622	645	Convex-up	Ebb	Tidal prism too small and ebb dominant therefore eroding
3.0	1054	15029333	810	Concave-up	Flood	Tidal prism too large and flood dominant therefore infilling
4.0	1387	19784406	1000	Concave-up	Flood	Tidal prism too large and flood dominant therefore infilling

Table 2.3. Summary of modelled scenarios presented in this paper.

Morphological grid	Physical processes	Figure
Idealised ($\gamma = 1.8, 2, 3$ and 4).	Tides (4m tidal range)	2.5
Idealised ($\gamma = 1.8$ and 4).	Wind (5 and 10 m/s both landward and seaward direction)	2.6
Idealised ($\gamma = 1.8$ and 4)	Tides (4m range) and wind (5 and 10 m/s both landward and seaward direction)	2.7
Idealised ($\gamma = 1.8$ and 4)	Tides (4m range), wind (5 and 10 m/s both landward and seaward direction) and waves.	2.8
Idealised ($\gamma = 1.8, 2, 3$ and 4)	Tides (4m range), wind (5 and 10 m/s both landward and seaward direction) and waves.	2.9
Raglan	Tide	2.10
Raglan	Tides (3m range), wind (5 and 10 m/s both landward and seaward direction) and waves.	2.10

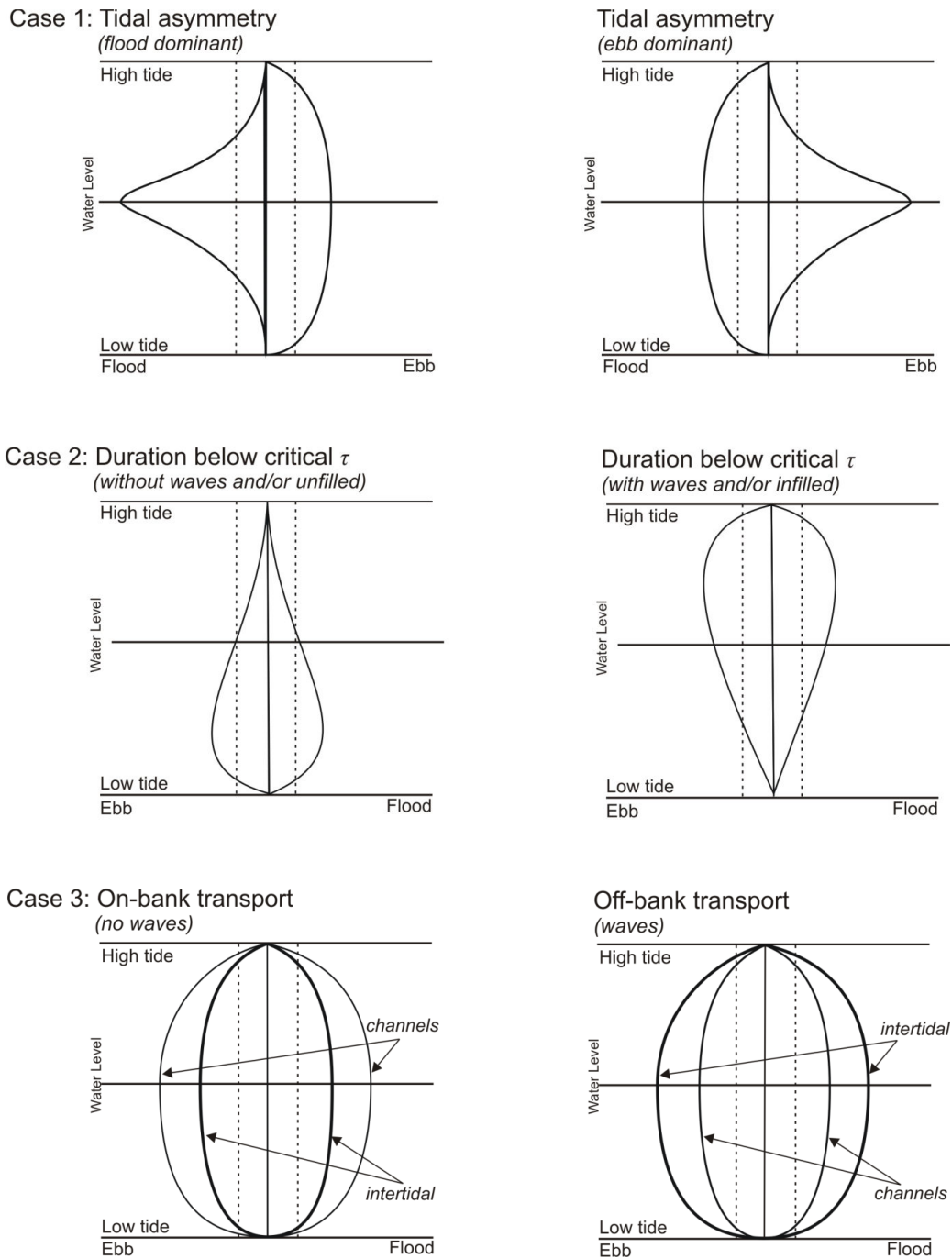


Figure 2.1. Schematic of different tidal asymmetries caused by Lagrangian and Eulerian effects. The schematic shows the distribution of τ caused by tidal currents (case 1 and case 2) and τ_{max} due to wave orbital and tidal currents combined (case 2 and case 3) as the water level changes with the tide. (Shear stresses are assumed to be basin-averaged). In each schematic, ebb and flood τ and τ_{max} are plotted as negative and positive values, respectively. The dashed line represents τ_c , above which sediment suspension occurs.

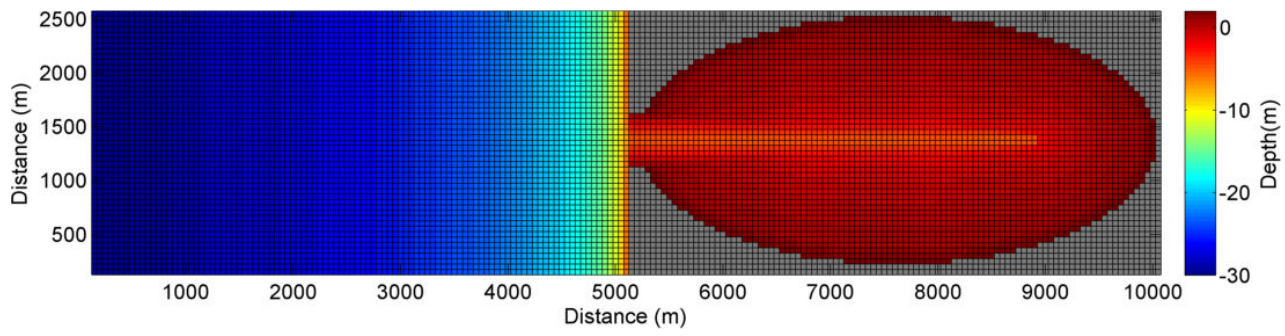


Figure 2.2. Numerical model grid and bathymetry. The model is forced at the single open boundary on the left hand side of the domain. The bathymetry in this figure is for the infilled basin ($\gamma=4.0$).

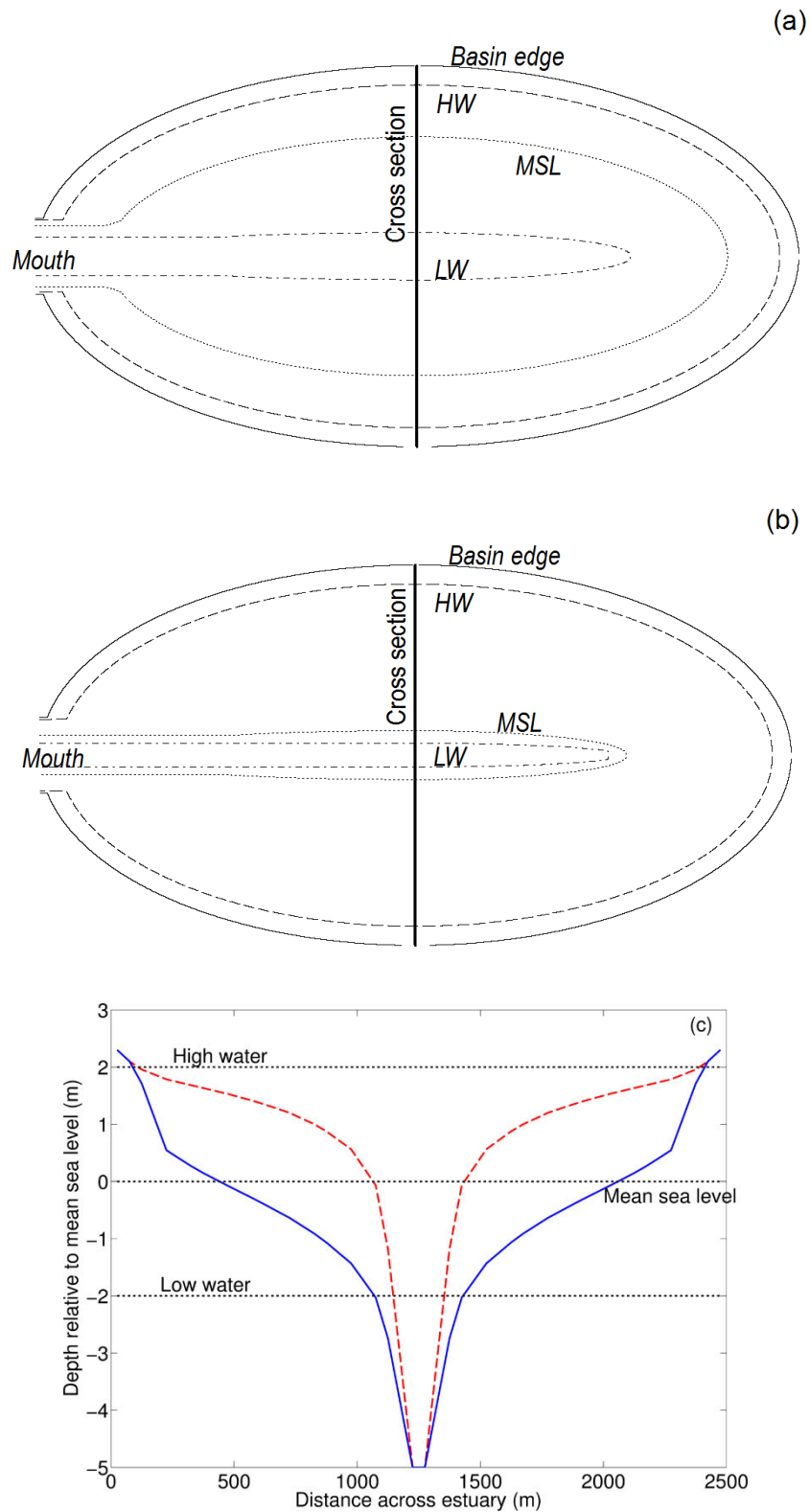


Figure 2.3. Schematic of unfilled (young) (a) and infilled (mature) (b) idealised morphologies showing location of LW, MSL and HW with cross sections taken through centre of basin (c) for unfilled (solid line) and infilled (dashed line) basins.

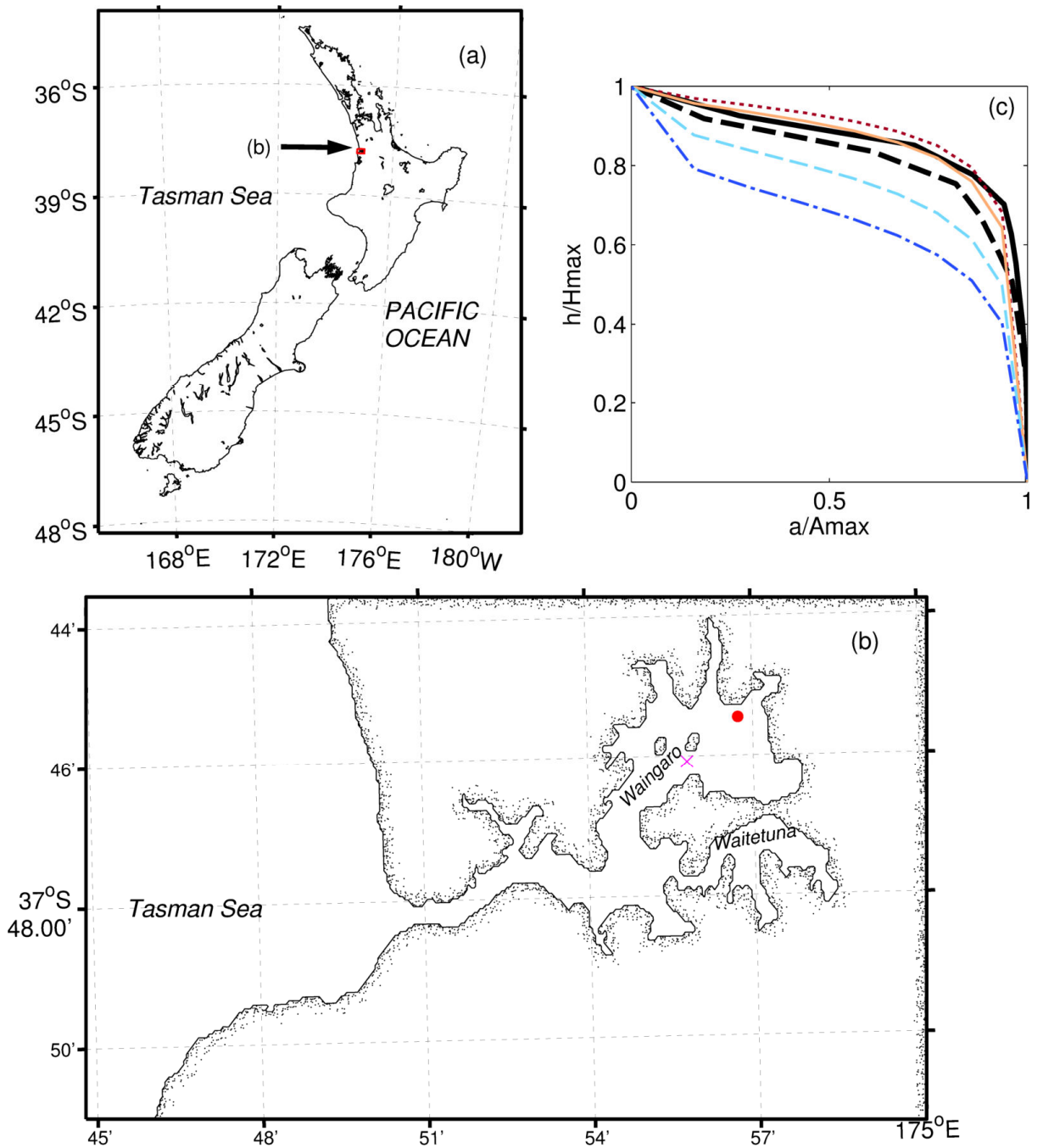


Figure 2.4. Location of Raglan Harbour on the coastline of the North Island, NZ (a) and detail of estuary form (b) showing the locations of field deployments of the intertidal FSI current meter (dot marker) and the subtidal Sontek ADP (cross marker). The morphological form of the northern (Waingaro) and southern (Waitetuna) arms (locations shown in (b)) is summarised and compared with the idealised estuaries as a series of hypsometric curves (c) with $\gamma = 4$ (dot dashed), $\gamma = 3$ (thin dashed), $\gamma = 2$ (thin solid), $\gamma = 1.8$ (dotted), northern (Waingaro) arm (thick dashed) and southern (Waitetuna) arm (thick solid).

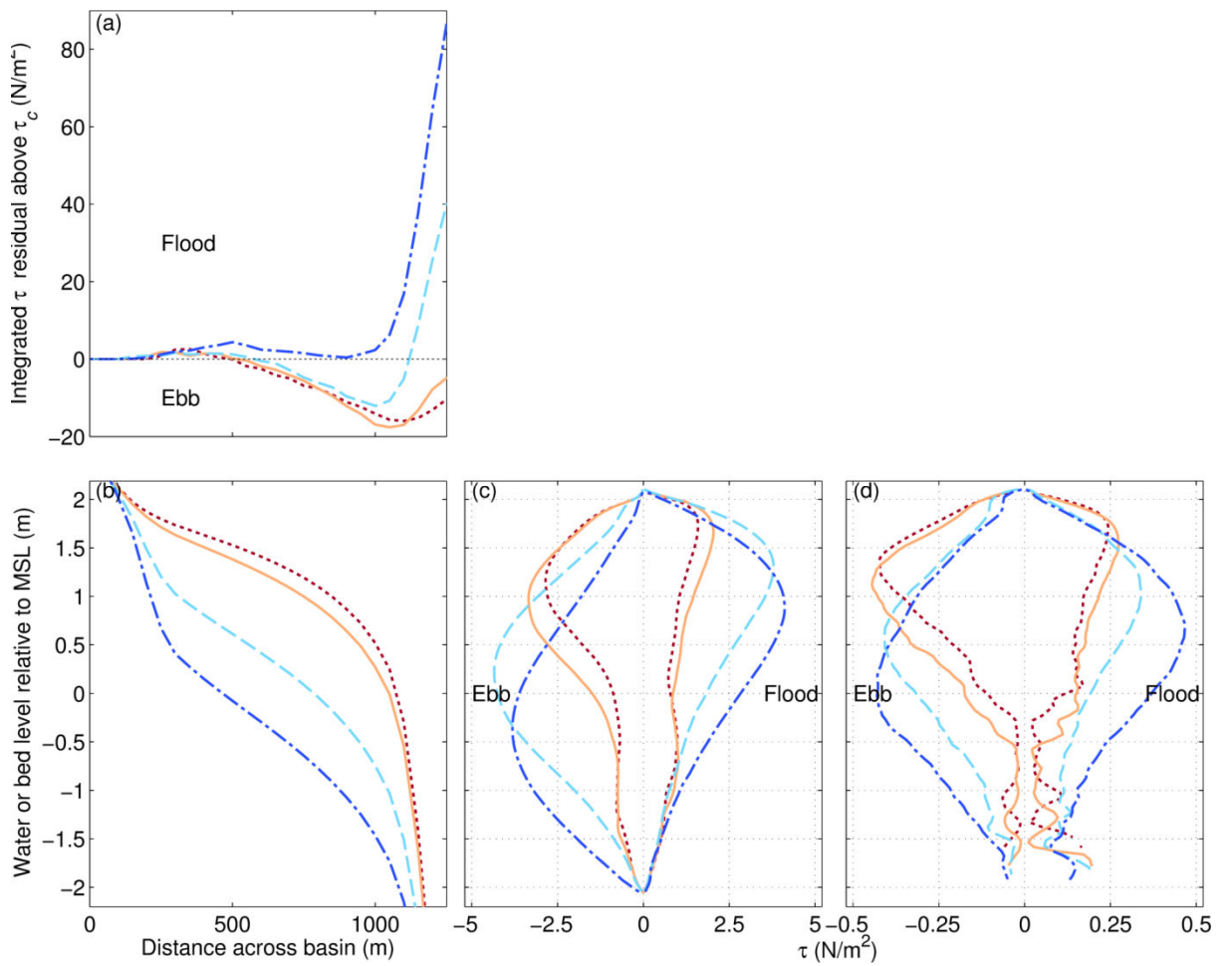


Figure 2.5. Modelling results for the case forced by tides only. (a) $\tau - \tau_c$, integrated over a transect through the centre of the basin perpendicular to the main channel, the transect is half that shown in Figure 2.3c. τ_c is for a 100 micron grain size. Flood and ebb-dominated residuals are positive and negative respectively. (b) Intertidal profile taken along the same transect as in (a). τ spatially averaged over the subtidal (c) and intertidal (d) plotted as a function of water level, where $\gamma = 4$ (dot dashed), $\gamma = 3$ (dashed), $\gamma = 2$ (solid) and $\gamma = 1.8$ (dotted). Averaging is performed separately for flood and ebb tide. Note different x-axis scale between c and d ($\times 10$). See text for details of averaging technique.

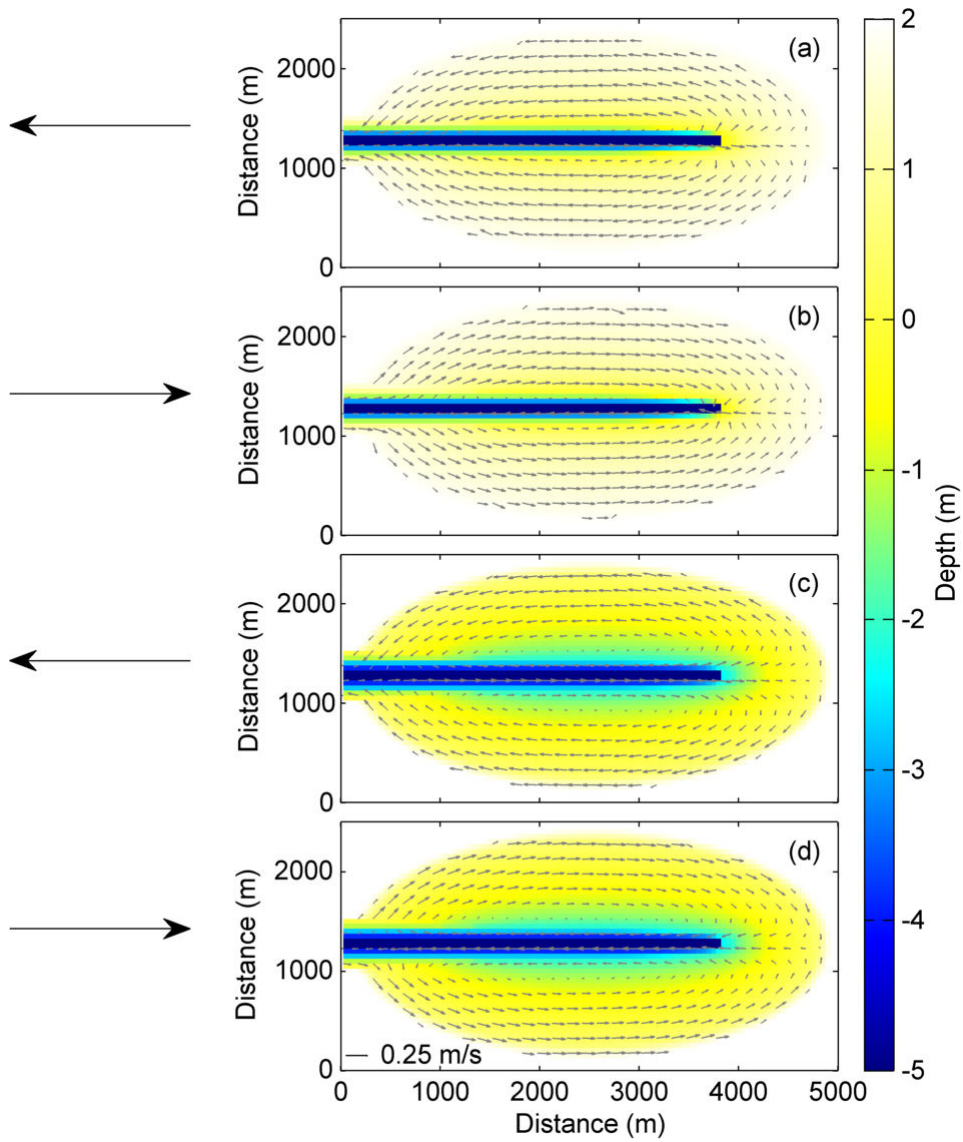


Figure 2.6. Depth-averaged flow residuals during a steady high-water level (no tide) with a spatially uniform and consistent 10 m/s seaward (easterly) (a and c) and 10 m/s landward (westerly) wind (b and d) for an infilled (a and b) and unfilled (c and d) morphology. Large arrows denote direction of wind.

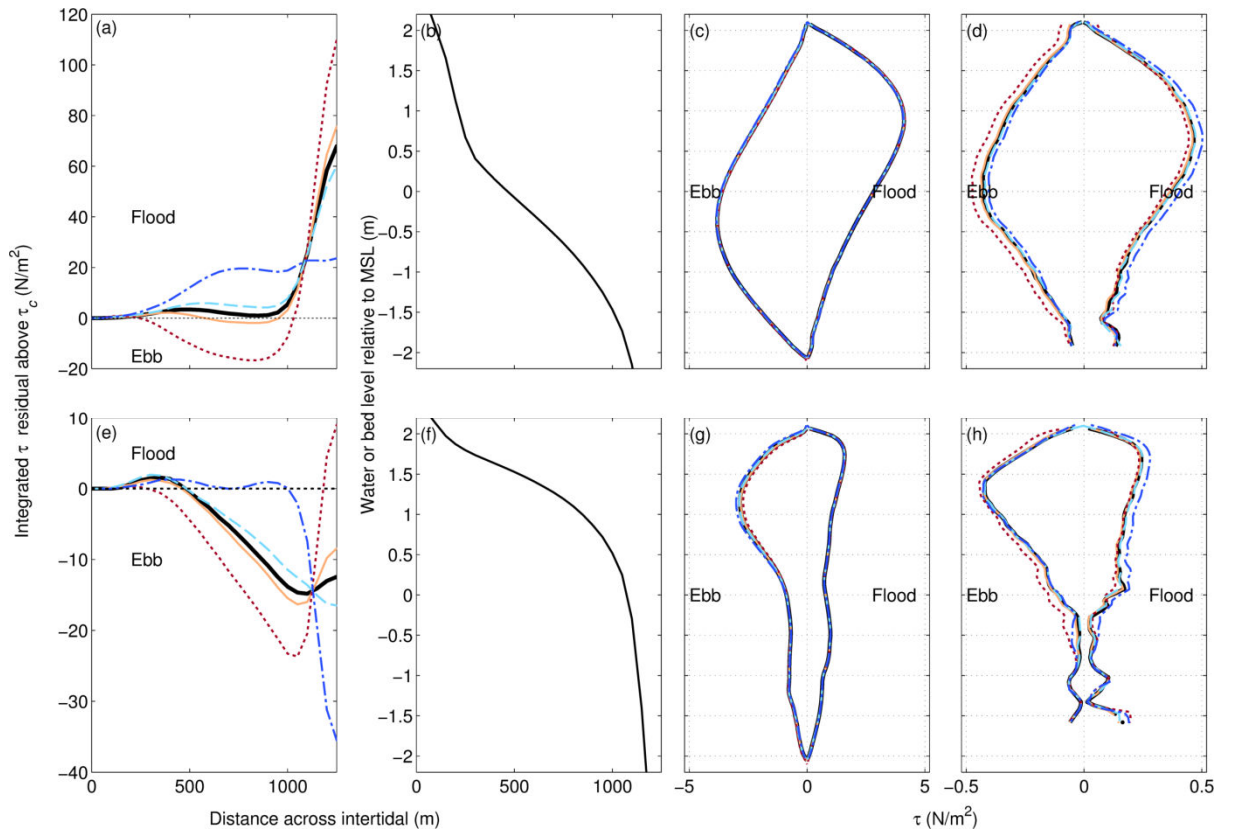


Figure 2.7. Model results for scenarios with tides and winds (no waves), shown for basin morphologies $\gamma = 4$ (a, b, c and d) and $\gamma = 1.8$ (e, f, g and h). Panels (a) and (e) show the $\tau - \tau_c$ (for a 100 micron grain) averaged along a transect through the centre of the basin perpendicular to the main channel (the transect is half that shown in Figure 2.3c), Positive = flood and negative = ebb results. (b) and (f) Intertidal profile shape taken along the same profile as in (a) and (e). Bed shear stress spatially averaged over the subtidal (c and g) and intertidal (d and h) domains for each scenario (dot dashed: 10 m/s westerly; dashed: 5 m/s westerly; thin solid: 5 m/s easterly; dotted: 10 m/s easterly; thick solid: no wind). Averaging is performed separately for flood (plotted as positive) and ebb tide (plotted as negative). Note different scale between (c) and (g) and (d) and (h). Westerly winds are directed into the basin (landward) and easterly winds are directed out of the basin (seaward). See text for details of averaging technique.

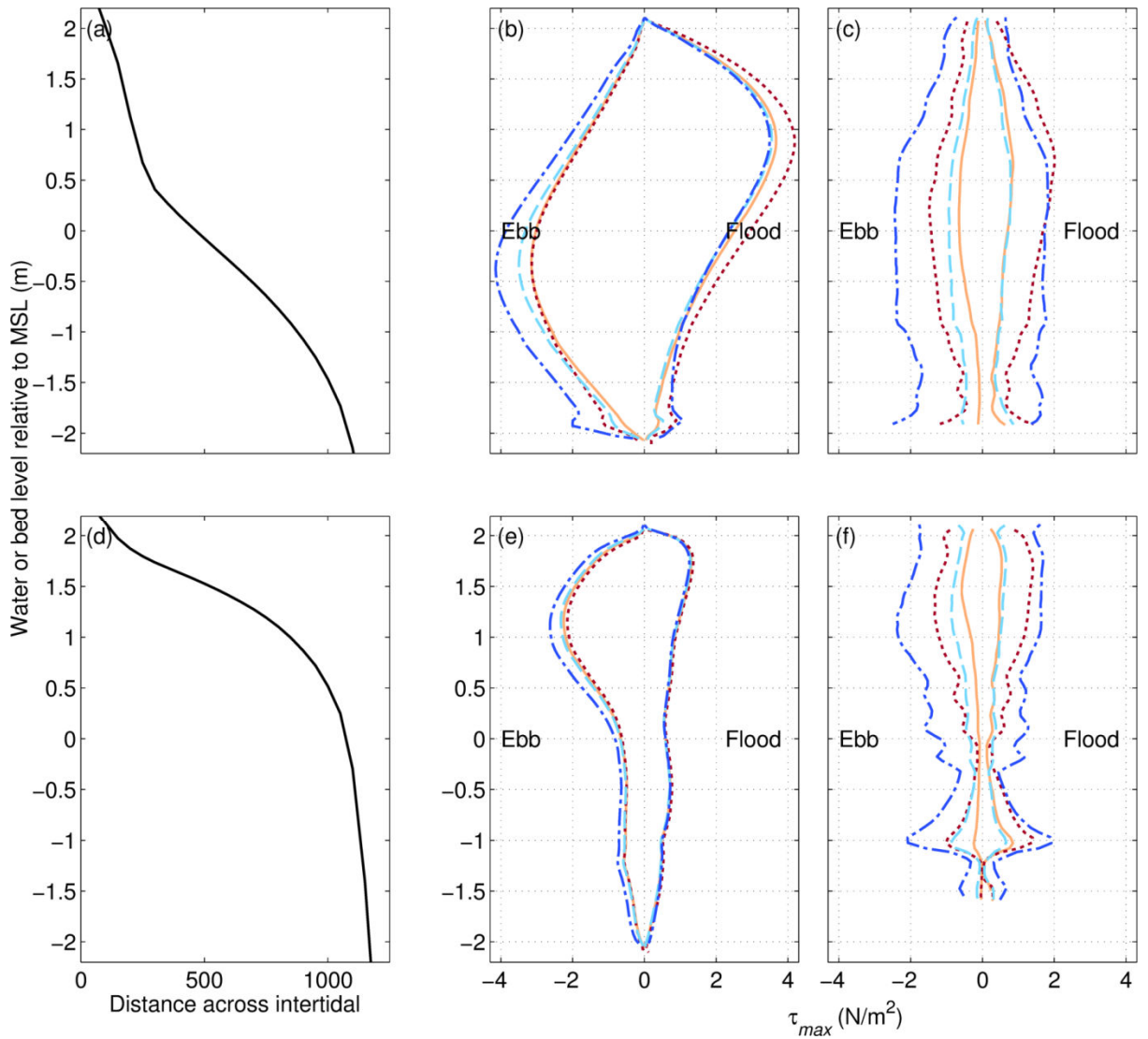


Figure 2.8. Model results for scenarios with tides, winds and waves shown for basin morphologies $\gamma = 4$ (a, b and c) and $\gamma = 1.8$ (d, e and f). Panels (a) and (d): Intertidal profile shape taken along a transect through the centre of the basin perpendicular to the main channel, the transect is half that shown in Figure 2.3c. Panels (b, c, e and f): τ_{max} from currents and waves spatially averaged over the subtidal (b and e) and intertidal (c and f) domains as a function of water level for each scenario (dot dashed: 10 m/s westerly, dashed: 5 m/s westerly; solid: 5 m/s easterly; dotted: 10 m/s easterly). Averaging is performed separately for flood (positive) and ebb tide (negative). Westerly winds are directed into the basin (landward) and easterly winds are directed out of the basin (seaward). See text for detail of averaging technique.

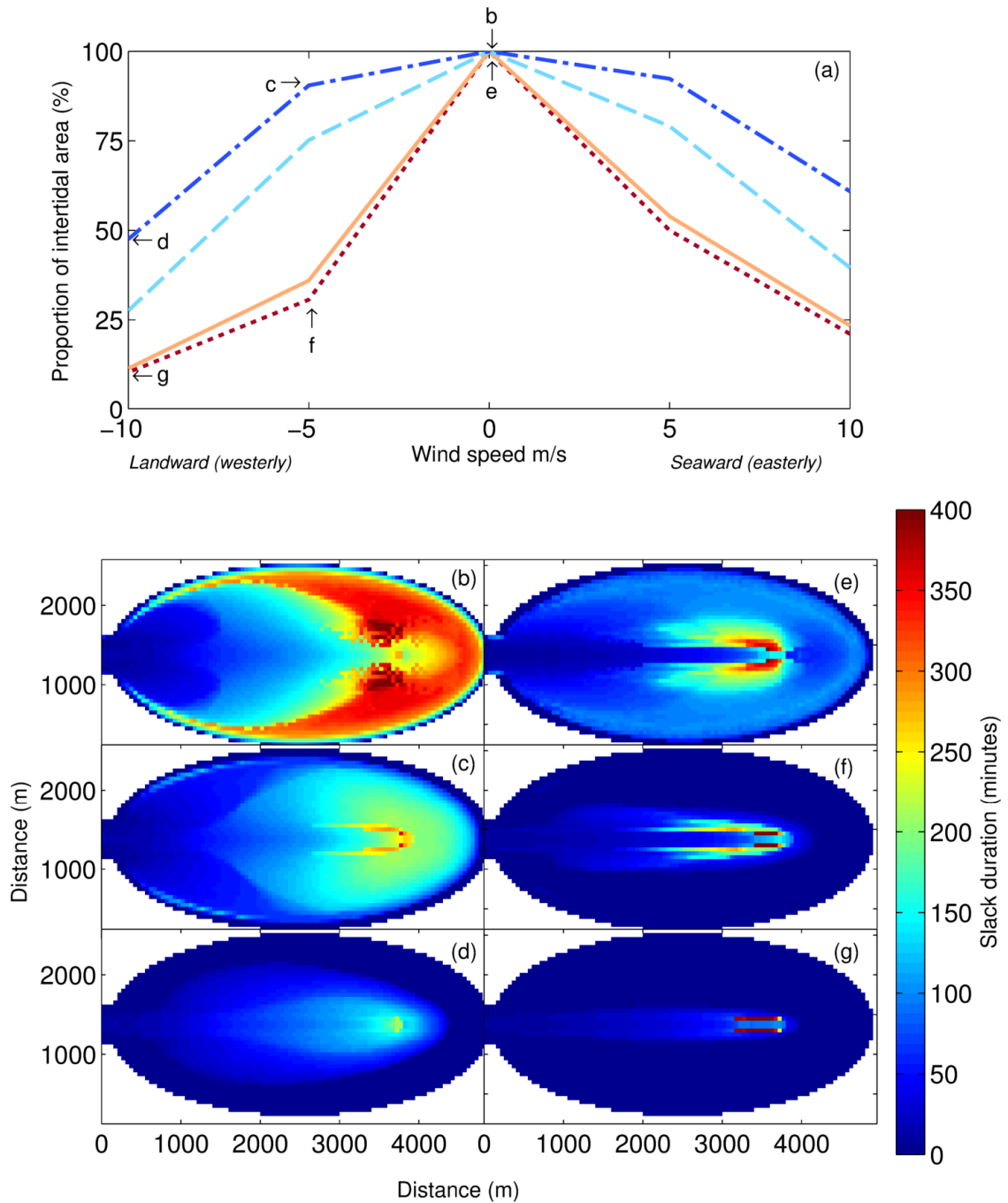


Figure 2.9. Panel a: The potential for deposition in the intertidal presented as the percentage of cells for which $\tau_{\max} < \tau_c$ (for a 100 micron grain) at any moment during the tidal cycle for $\gamma = 4$ (dot dashed), $\gamma = 3$ (dashed), $\gamma = 2$ (solid) and $\gamma = 1.8$ (dotted) morphologies. Panels b-g: spatial distribution of the length of time in minutes for which $\tau_{\max} < \tau_c$ for a tide only scenario (b and e) and a 5 m/s (c and f) and 10 m/s (d and g) landward (westerly) wind and wave event for a unfilled ($\gamma = 4.0$) (b, c and d) and an infilled ($\gamma = 1.8$) (e, f and g) basin. The locations of panels b-g are marked on panel a.

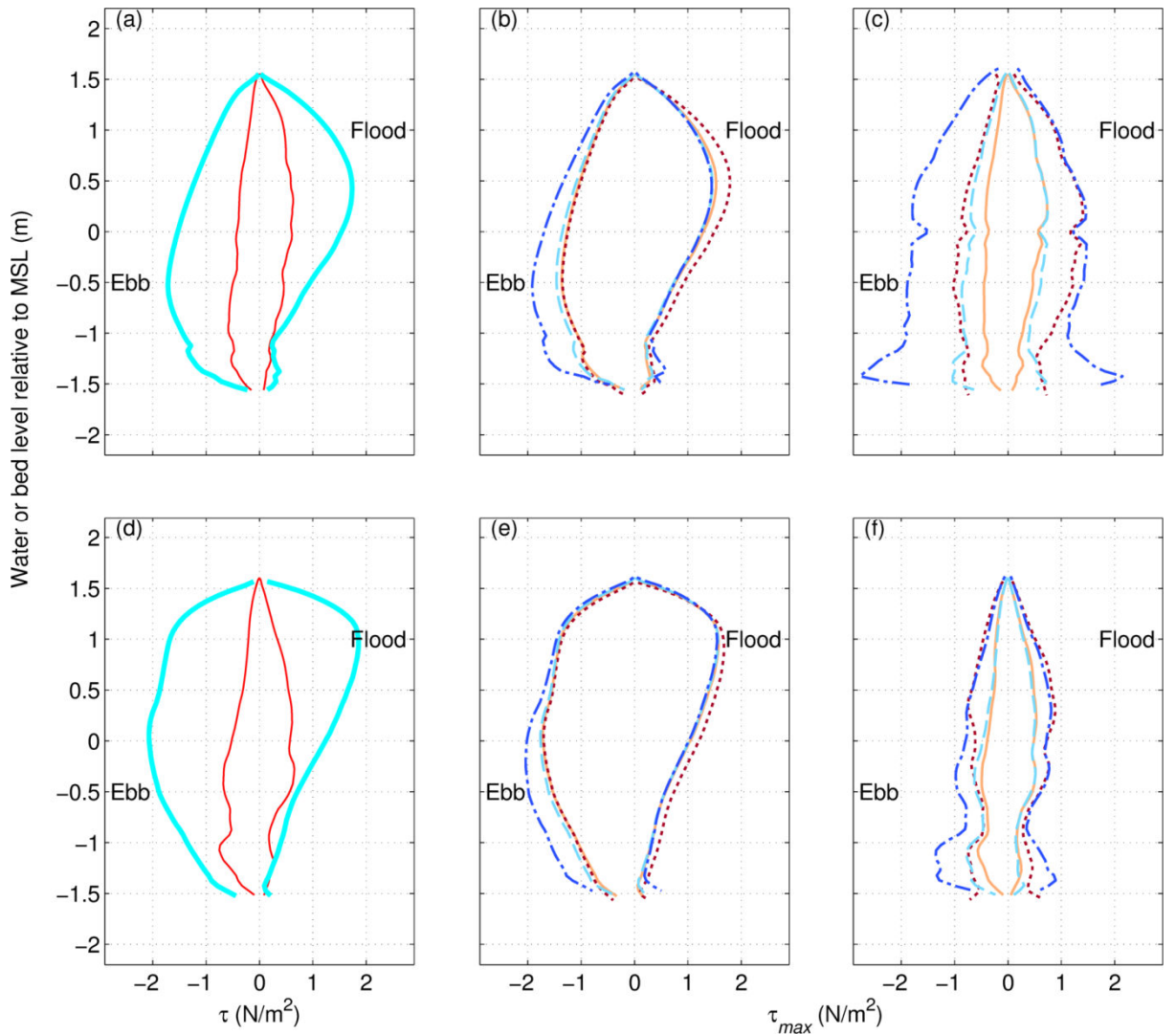


Figure 2.10. Model results from the case study with tides, winds and waves for the less infilled fetch-aligned northern (Waingaro) arm (a, b and c) and the more-infilled non fetch-aligned southern (Waitetuna) arm (d, e and f), see Figure 2.4b for locations. The τ results from the tide only model are shown in (a) and (b) where the thick line is subtidal values and thin line is intertidal values. τ_{max} due to tides, winds and waves averaged over the subtidal (b and d) and intertidal (c and e) domain, where dashed dot: 10 m/s southwesterly; dashed: 5 m/s southwesterly; solid: 5 m/s northeasterly; dotted: 10 m/s northeasterly. Averaging is performed separately for flood (positive) and ebb (negative) tide. Southwesterly winds are directed into the basin (landward) and easterly winds are directed out of the basin (seaward). See text for details of averaging technique.

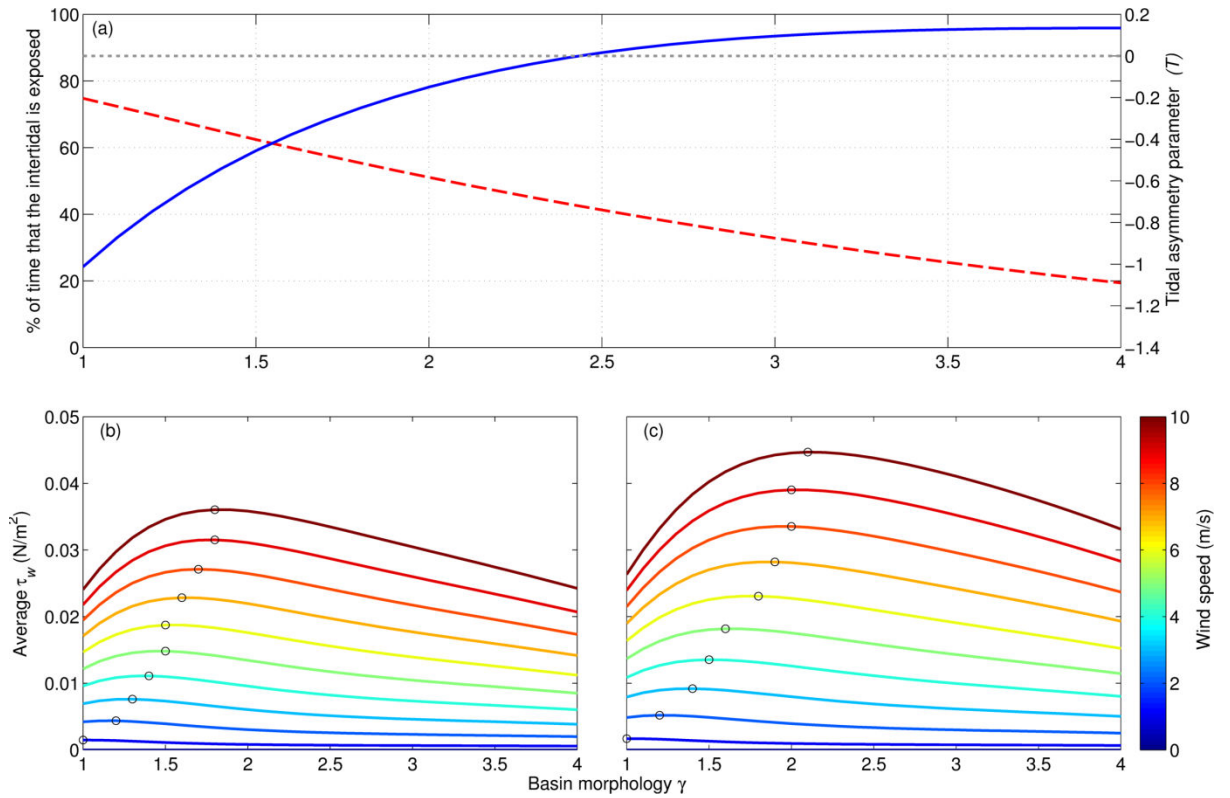


Figure 2.11. Schematic representation of asymmetry-related processes identified using simple analytic relationships (see text). Panel (a) the tidal asymmetry parameter T predicted in equation 2.1 and 2.2 (solid line) and the percentage of time during the tidal cycle that the intertidal is exposed (dashed line). These equations predict that a stable intertidal should occur when $T=0$. Panel (b) τ_w averaged over the intertidal and over a tidal cycle for each hypsometry during a fetch perpendicular (b) and fetch parallel wind direction (c) and wind speeds ranging between 0 and 10 m/s, black circles show the maximum τ_w .

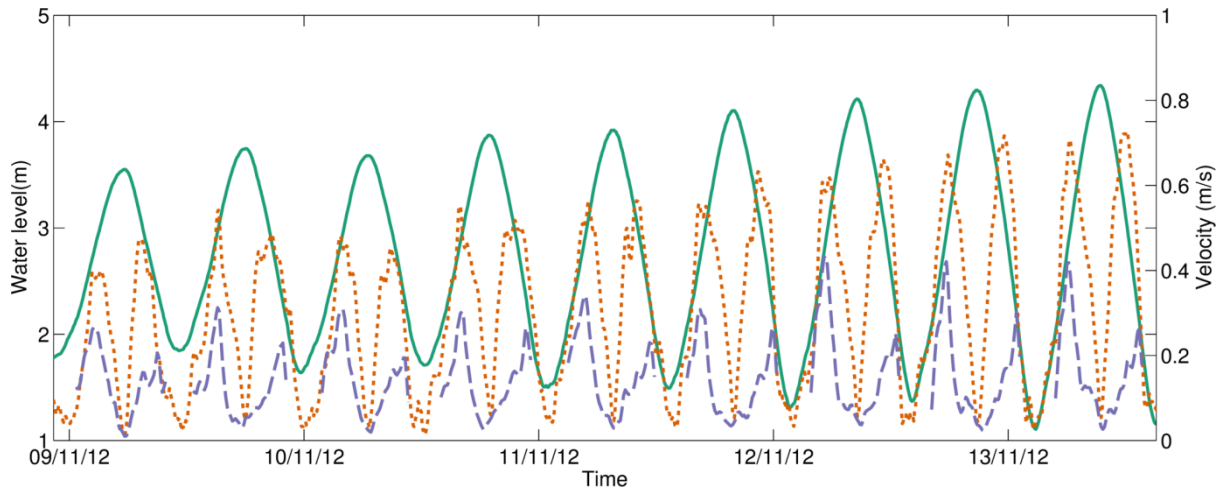


Figure 2.12. Water levels (solid line) and current velocities (dotted line) collected using a Sontek ADP (subtidal) and current velocities (dashed line) collected with a FSI 3DACM Wave recorder showing contrasting tidal asymmetries over the intertidal and subtidal areas of the northern (Waingaro) arm of Raglan Harbour, New Zealand. The locations of deployments are shown in Figure 2.4b

Chapter 3. Observations of asymmetry in contrasting wave- and tidally-dominated environments within a mesotidal basin: implications for estuarine evolution



Upper Waingaro (northern) arm, Whaingaroa (Raglan) Harbour.

3.1 Introduction.

Tides and tidal asymmetry are essential drivers of sediment transport, morphological change and stability in estuarine environments (Friedrichs and Aubrey, 1988, Friedrichs, 2011). A system of non-linear feedbacks links tides and morphology, in which the tidal asymmetry affects sediment deposition patterns, and then the modified morphology further alters the asymmetry by distorting the tidal wave (e.g. Lanzoni and Seminara, 2002, Friedrichs, 2010).

Tidal asymmetry can affect sediment transport in two ways: (i) through an imbalance in maximum flow causing either the flood (flood dominant) or ebb (ebb dominant) currents to be stronger and (ii) through changes in the duration of time around slack water during which sediment can settle out of suspension and deposit on the seabed (Friedrichs, 2011). Intertidal areas in which the average water depth is deep relative to mean sea level (MSL) (such as in the case of a concave-shaped depth profile) will tend to slow the progression of low water (LW) relative to high water (HW). This deep intertidal morphology will create faster currents during the flood (flood dominant peak velocity) and encourage slower water movement around high water due to the deeper water over the intertidal areas (longer HW slack). In contrast, an intertidal area in which the average water depth is shallow (such as in the case of a convex-shaped depth profile) slows the progression of HW relative to LW, creating faster currents during the ebb (ebb dominant) and a shortened slack water period (shorter HW slack; Wang et al., 2002, Friedrichs, 2010).

The wetting and drying of intertidal areas further complicates patterns of tidal asymmetry in the upper reaches of an estuary. Due to a partially-progressive tidal wave (Hunt et al., 2015 and Chapter 2) and channelisation affects (Fagherazzi et al., 2008), the timings of maximum ebb and flood current are delayed when the intertidal regions are shallow, and this delay results in maximum flood currents occurring when the upper intertidal is inundated and maximum ebb currents occurring when the water is constrained in the subtidal channel. This temporal asymmetry means that upper intertidal areas will always be flood dominant regardless of the dominance that may occur in the subtidal channel (Hunt et al., 2015 and Chapter 2). The effect of flood dominance on sediment deposition over

the upper intertidal is strengthened when the duration of slack water at high tide is increased (which extends the time over which sediment can settle out of suspension over the intertidal areas).

Shear stresses created by wave orbital velocities are also highly influential in controlling sediment dynamics over intertidal areas (Green et al., 1997, Fagherazzi et al., 2006, French et al., 2008, Green, 2011) and have been cited as the main mechanism responsible for erosion on tidal flats (Fagherazzi and Wiberg, 2009). Waves create a suspended sediment gradient which can cause advection-driven sediment transport from areas of high to low concentrations (Jansen-Stelder, 2000) and also reduce the amount of time around slack water during which deposition can occur (Hunt et al., 2015 and Chapter 2).

Schematic modelling has provided support for the strong influence of waves on the shape and form of the intertidal morphology (Fagherazzi et al., 2006, Mariotti and Fagherazzi, 2013a, Hunt et al., 2015 and Chapter 2). When changes are forced by tidal processes alone, intertidal areas evolve towards a convex equilibrium shape (Roberts et al., 2000; Waeles et al., 2004, Friedrichs and Aubrey, 1996) in which the intertidal water depth is shallow relative to mean sea level (Fagherazzi et al., 2006, Mariotti and Fagherazzi, 2013a). Conversely, within wave dominated environments, the intertidal profile tends toward a concave shape in which the intertidal water depth is deeper relative to mean sea level (Friedrichs and Aubrey, 1996, Waeles et al., 2004, Bearman et al., 2010, Zhou et al., 2015). As the intertidal depth and extent is a principal control on the tidal asymmetry (Friedrichs, 2011), an understanding of estuarine morphological evolution will require that both waves and tides should be considered in combination (Mariotti and Fagherazzi, 2013a). In addition to generating short period waves, winds also strongly influence circulation patterns (Narváez and Valle-Levinson, 2008, Henderson and Mullarney, 2013) to the extent that they can influence the strength of tidal asymmetry (Hunt et al., 2015 and Chapter 2).

The research summarised above can be split into two categories: (i) detailed measurements of estuarine hydrodynamics over short (days to weeks) timescales and (ii) the theoretical long-term (decadal timescale) evolution of estuary morphology using models forced by wave and tidal processes. The ability of

waves to shape the intertidal or the “morphological significance” of small waves in microtidal environments has been demonstrated previously (Green, 2011). Preliminary modelling work has shown that waves may also play a role in mesotidal estuaries (Hunt et al., 2015 and Chapter 2) where tides are normally considered to dominate and waves play a more minor role. Here, we extend on this work, and use a combination of hydrodynamic measurements and sediment deposition records to determine the conditions under which the observed waves are “morphologically significant” relative to tidal currents in a mesotidal estuary. Field measurements consisted of month-long hydrodynamic measurements of asymmetry and suspended sediment measurements, and were complemented by decadal-scale measurements of bed level, wind conditions, and comprehensive bathymetric information. Our measurements allow for the identification of the various spatial and temporal scales over which hydrodynamic processes operate. Waves are less predictable than tides, and although theory shows that waves can change asymmetries and play an enhanced role in driving morphological change relative to the more predictable tidal processes, such occurrences might be rare. Field measurements were collected in an estuary with two contrasting arms, one in which the dominant fetch is aligned to the typical wind direction and an arm that is not well aligned, and so we hypothesise that infilling will be prevented by waves for the fetch-aligned case, whereas tidal processes and accretion should dominate in the less aligned estuary.

3.2 Study area and field data collection

3.2.1 Study area

Raglan (Whaingaroa) Harbour is situated on the west coast of New Zealand’s North Island (Figure 3.1a). The estuary is a flooded dendritic river valley and the mouth is partially enclosed by sand spits and dunes flanking the Tasman Sea. The estuary is mesotidal, with a spring tidal range of ~3 m (Sherwood and Nelson, 1979). Freshwater is supplied to the estuary from a number of tributaries of which the Waingaro and the Waitetuna are the largest. Total mean freshwater flow from all tributaries ($18 \text{ m}^3/\text{s}$) is low compared to the tidal prism ($46 \times 10^6 \text{ m}^3$ and $29 \times 10^6 \text{ m}^3$ during spring and neap tides, respectively) and therefore tidal processes dominate circulation within the harbour (Heath, 1976).

The dendritic form of Raglan estuary (Figure 3.1b) encompasses two distinct arms of the harbour connected by a confluence of the tidal drainage network; a ‘fetch-aligned arm’ (the Waingaro in the north) and a ‘non-fetch-aligned’ arm (the Waitetuna in the south) relative to the prevailing wind direction (Figure 3.2a). Wind speeds and directions recorded at Taharoa (situated on the open coast 40 km south of Raglan, Figure 3.1a) between 10th August 1978 and 1st January 2013 show that the prevailing northeast and southwest wind directions are aligned along the thalweg of the northern arm with stronger winds from the southwest (Figure 3.2a). Southwest winds are more frequent during the southern hemisphere summer (around December). The contrast between the two arms is clearly apparent when comparing the difference in occurrence of predicted wave height calculated using empirical equations from CERC (1984) with the fetch measured from aerial photography and the wind speeds and directions from Figure 3.2a (Figures 3.2b and 3.2c). Significant wave heights (H_s) in the southern arm (Figure 3.2c) are far lower and rarely exceed 0.3 m even during strong winds from the south west, whereas in the Northern arm, the same weather conditions create waves that exceed 0.5 m and occasionally reach 0.7 m in height (Figure 3.2b).

The bathymetry of Raglan Harbour was measured using LiDAR, bathymetry surveys (a combination of single beam and multibeam surveys) and the navigation chart (LINZ chart NZ4421). The bathymetry is summarised as hypsometric curves showing the dimensionless ratios of area against height for each arm of the harbour in Figure 3.1d. This comparison shows a distinct difference between the two arms of the harbour with the northern fetch-aligned arm (dashed line) exhibiting a slightly more concave form with deeper water levels over the intertidal flats (relative to MSL) and the sheltered southern arm (solid line) showing shallower water levels over the intertidal (relative to MSL) and a more convex intertidal shape. The contrast in the contemporary morphology between the two arms is also reflected in the records of morphological change from cores (Swales et al., 2005) and accretion plates. The southern arm has experienced sedimentation rates ranging from 0.35 mm/yr prior to human settlement increasing to 1.1 mm/yr since 1890 (following catchment deforestation), further increasing to 2.5 mm/yr since the early 1990s (Swales et al., 2005, Bentley et al., 2014) and ~ 3.4 mm/yr between 2003 and 2011. In direct contrast, the northern

arm has experienced almost no contemporary sedimentation for at least the last 150 years (Swales et al., 2005), despite similar changes in catchment land-use. The texture of sediment data collected in Raglan Harbour also shows variability in the distribution of hydrodynamic energy, with the southern arm exhibiting a higher energy environment in the subtidal channels (coarser sediments) and lower energy environment on the top of the intertidal areas (finer sediments) (Sherwood and Nelson 1979). In the northern arm, the reverse is true, with textural patterns showing that often the higher intertidal flats are characterised by coarser sediments as indicative of higher energy environments (Sherwood and Nelson, 1979).

Sediment samples (Needham et al., 2014) have been taken 4 times a year at the same location as the sediment plates and cores. Analysis of these samples indicates that between 2001 and 2007 the sediment at Okete Bay (outside the mouth of the southern arm) and Haroto Bay (in the southern arm) became proportionally muddier, all other locations remained the same. Between 2007 and 2011 mud content was consistent at all sites. These samples indicate that the sediment type in the northern arm will be similar to that recorded by Sherwood and Nelson (1979) as the cores show no deposition in the main body of this arm. It is likely that continuing deposition of fine material in the tidally dominated southern arm has resulted in a greater proportion of fine sediment. Visual inspection of the intertidal flats in the southern arm shows that the bed comprises a mixture of fine mud, sand and shells from dead *Paphies australis* and *Crassostrea glomerata* (Figure 1.1g). The intertidal flats in the northern arm contains the same mix but with proportionally less fines, outcropping areas of rock platform and more living shellfish, possibly due to the reduced sedimentation rate in the northern arm Figure 1.1c, e and f).

3.2.2 Instrumentation and methods

Field measurements were made within Raglan Harbour to examine if there was a contrast in the dominance of wave-induced relative to tide-induced dominance in asymmetry between the two arms (Table 3.1 and Figure 3.1). Currents and water levels in the northern and southern arms were recorded using a Sontek Acoustic Doppler Profiler (ADP) and Sontek Acoustic Doppler Velocimeter (ADV),

respectively (Figures 1 and 3), between the 24th October 2012 and 20th November 2012. The ADV was deployed at the depth of low water (~3 m deep at high tide) at the interface between the intertidal flat and subtidal channel (Figure 3.1b) and wave data were also collected using the ADV pressure sensor.

The intertidal (water depth < 2 m) hydrodynamics over the unfilled (northern) arm were recorded using instruments oriented along a ~200 m shore perpendicular transect (Figure 3.1b). This transect was first placed in an orientation perpendicular to the prevailing wind direction between 16th October and 7th November (T1) and then in an orientation parallel with the prevailing wind direction (T2) between 8th and 26th November 2012 (Figure 3.1b). The rationale behind this approach was to confirm predictions from idealised modelling of the conditions under which waves are the dominant control of bed-shear stress (Hunt et al., 2015 and Chapter 2). The instrumentation (Figure 3.1c) comprised an FSI current meter recording pressure and u and v components of the current, a DOBIE pressure sensor wave recorder and two co-located but vertically-separated OBS sensors mounted at the bed and ~0.4 m above the bed. Weather data (pressure, temperature, wind speed and direction) were collected between 30th April 2012 and 29th September 2013 and the measurements overlapped the hydrodynamic deployments.

The DOBIE and ADV pressure data were corrected for atmospheric pressure (recorded by the weather station) and converted to hydrostatic depth assuming a representative seawater density of 1018 kg/m^3 . The surface wave spectrum was then reconstructed from each wave burst. To correct for the attenuation of higher frequency waves, wave spectra were extrapolated to estimate the energy above the cut-off frequency using an f^{-4} curve, a technique which has successfully been used in similar estuarine environments (e.g. Smith et al., 2001, Jones and Monismith, 2007, Mariotti and Fagherazzi, 2013b). All spectra were truncated and extrapolated at a fixed frequency cut-off of 0.8 Hz through to 5 Hz for the DOBIE and 2 Hz for the ADV (the Nyquist frequency of each instrument). Significant wave height and peak and mean period were then calculated from the spectral moments. Finally, all waves with H_s of less than 0.05 m were discarded

to allow for any potential errors associated with pressure measurements and the analysis (e.g. following Mariotti and Fagherazzi, 2013b).

Bed shear stress due to currents (τ) was calculated using the recorded tidal current speeds and water depths in the equations described in Soulsby (1997) and Whitehouse et al., (2000). For the depth averaged velocities recorded by the ADP, τ was calculated as

$$\tau = \rho C_D \bar{U}^2, \quad (3.1)$$

where the drag coefficient (C_D) is

$$C_D = \left[\frac{0.40}{1 + \ln z_o/h} \right]^2, \quad (3.2)$$

where z_o is the bed roughness length, h is water depth, ρ is density of water and \bar{U} is depth averaged current speed.

For the ADV and the FSI current meter, τ is calculated using current speed at a fixed depth using

$$\tau = \rho u_*^2, \quad (3.3)$$

where u_* is the friction velocity

$$u_* = U \times 0.40 / \ln \left(\frac{z}{z_o} \right), \quad (3.4)$$

in which U is the horizontal component of water velocity at height z above the seabed. z_o is the bed roughness length, which although not measured directly, was chosen using the measured values reported in Soulsby (1997), for the seabed sediment type that was observed at the site depending on the sediment composition.

Bed shear stresses due to the effect of waves alone (τ_w) were calculated using the recorded significant wave height (H_s) and wave period (T) and the following equations (Soulsby, 1997 and Whitehouse et al., 2000):

$$\tau_w = \frac{1}{2} \rho f_w U_w^2, \quad (3.5)$$

where the wave orbital velocity amplitude at the seabed, U_w is

$$U_w = \frac{\pi H_s}{T \sinh kh}, \quad (3.6)$$

and where κ is the wave number and the wave friction factor (f_w) is the larger of either the rough-bed wave friction factor (f_{wr}) or the smooth-bed wave friction factor (f_{ws}) (Soulsby, 1997), i.e.

$$f_{wr} = 1.39 \left(\frac{A}{z_0} \right)^{-0.52}, \quad (3.7)$$

$$f_{ws} = B R_w^{-N}. \quad (3.8)$$

The coefficients B and N were selected based on the wave Reynolds number as recommended by Soulsby (1997),

$$R_w = \frac{U_w A}{\nu}, \quad (3.9)$$

where ν is the kinematic viscosity of water and the orbital amplitude of wave motion at the bed (A) is given by

$$A = U_w T / 2\pi. \quad (3.10)$$

For $R_w \leq 5 \times 10^5$, $B = 2$, $N = 0.5$ (laminar flow) and for $R_w > 5 \times 10^5$, $B = 0.0521$, and $N = 0.187$ (smoothly turbulent flow).

Finally, bed shear stresses due to tides and currents combined (τ_{max}) were also evaluated using methods described in Soulsby (1997) and Whitehouse et al., (2000):

$$\tau_{max} = [(\tau_m + \tau_w \cos \phi)^2 + (\tau_w \sin \phi)^2]^{1/2}, \quad (3.11)$$

in which

$$\tau_m = \tau \left[1 + 1.2 \left(\frac{\tau_w}{\tau + \tau_w} \right)^{3.2} \right] \quad (3.12)$$

where τ_m is the mean bed shear stress during a wave cycle under combined waves and currents, and ϕ is the angle between current direction and direction of wave travel. Wave data from the DOBIE pressure sensor is non-directional and

therefore wave travel direction was assumed to be the same as the wind-direction recorded at the Raglan weather station situated < 10 km from the DOBIE pressure sensors (Figure 1b). Waves refract as they propagate over intertidal flats. To test whether the use of wind direction is suitable as a proxy for intertidal wave direction, a SWAN-Delft3D model was run, calibrated using the data collected here. The mean difference between τ_{max} calculated from the model and τ_{max} used here differ on average by only 0.038 N/m² at Transect 1 and 0.026 N/m² at Transect 2. Moreover, linear regression comparing the two calculated timeseries of τ_{max} shows good agreement between the two methods at both Transect 1 ($r^2 = 0.99$ and RMSE = 0.065 N/m²) and Transect 2 ($r^2 = 0.96$ and RMSE = 0.050 N/m²).

3.3 Results

The data recorded by the instruments are summarised in Figure 3.3. The tidal stage diagrams for τ are shown in Figure 3.4, which compares the magnitude and duration of τ through the ebb stage (negative τ values) and flood stage (positive τ values) of the tide highlighting the timing, strength and direction of tidal asymmetry. The tidal stage plots for the northern part of the estuary exhibit no clear tidal asymmetry in the subtidal channel (Figure 3.4a, solid blue line) with only a very weak dominance during the ebbing part of the tide at a water level of 3 m. This pattern of tidal asymmetry would result in no net direction of sediment transport with almost equal τ during the flood and ebb. However, during the intertidal T1 deployment (location on Figure 3.1b) the τ (Figure 3.4a, dotted line) indicate flood dominance on average with higher maximum τ occurring during the flood stage of the tide. The deeper T2 deployment (Figure 3.4a, dashed line) also shows a clear pattern of strong flood dominance with a marked strengthening of the τ maximum during the flood tide; this flood dominance tends to strengthen during springs and weaken during neaps (not shown).

The difference in tidal asymmetry between the subtidal and intertidal areas occurs due to a temporal asymmetry between the timing of maximum ebb and maximum flood flow, which is evident in measurements from the T2 deployment (Figure 3.4a dashed line), in which the flood maximum occurs when the water level is at 2.8 m and the ebb maximum occurs when the water level is at 2.4 m. Overall

these asymmetries cause the maximum flood current to occur when the water occupies the intertidal area and the maximum ebb to occur when the water is below the intertidal surface. Therefore flood-dominant asymmetry always occurs over the shallow intertidal areas in this situation regardless of the relative strengths of the maximum flood and ebb velocities in the subtidal channels. The subtidal deployments in the northern and southern arm show a strong rectilinear tidal pattern that is parallel with the orientation of the subtidal channel. In contrast the intertidal currents are less rectilinear but in general exhibit a cross shore orientation at T2 and an alongshore orientation at T1.

In the absence of waves, the tidal currents clearly control the pattern and strength of suspended sediment concentrations with higher concentrations occurring during the flood stage of the tide (Figure 3.5a and 3.5b). The suspended sediment concentration decreases during slack water when sediment can fall out of suspension and deposit on the seabed. Following high tide, the suspended sediment level increases again during the ebb but by a lower magnitude than that during the flood (Figure 3.5b) resulting in a net sediment flux in the landward direction. This net landward transport of sediment is contrary to the lack of accretion in the sediment records.

The southern sheltered arm of the harbour shows a clear trend of ebb dominance with stronger currents during the ebb phase of the tide (Figure 3.4b). The ebb dominant hydrodynamics in the subtidal area of the southern arm should indicate a system that exports sediment; however, sediment plate data and sediment cores of historical deposition indicate an accretional regime (Swales et al., 2005). Velocity data from the southern arm show a marked temporal asymmetry with the timing of maximum velocity delayed during both the flood and ebb stages of the tide. This delay means that the maximum flood velocity (and τ) occurs closer to high water and the upper part of the intertidal area ($>\sim 2$ m above LW) will be flood dominant whilst subtidal currents remain ebb dominant.

The observed H_s at transects T1 and T2 can be clearly related to the fetch at each location. Figure 3.6a shows the recorded significant wave height from the DOBIE pressure sensor and the corresponding wind direction recorded at the Raglan weather station during the T1 and T2 deployments. Figure 3.6b shows wind

directions and speeds during the T1 and T2 deployments recorded at the Raglan weather station. During the T1 deployment, the largest waves occur with winds from the west-southwest (WSW) to the northwest (NW) sectors (Figure 3.6a); this direction coincides with the strong winds from these sectors but not directly with the prevailing winds from the SW (Figure 3.6b) due to the sheltering effect of the peninsula to the west of the deployment (Figure 3.1b). At T2, the largest waves occur during the prevailing winds from the SW due to the large fetch exposure from this direction. The largest H_s occurs at T2 despite the lower wind speeds measured during this deployment, due to the exposure at T2 to the largest fetch direction (which is also the prevailing wind direction).

Three tidal cycles were selected to illustrate how the patterns of bed shear stress and suspended sediments are modified during wave events (Figures 3.5c – h) compared to the previously described tide-only ($H_s < 0.05$ m). During wave events (Figures 3.5c – h), the flood-directed suspended sediment flux on the intertidal that occurred when tidal processes dominated (Figures 3.5a and b) is reversed by the increase in suspended sediment concentrations both during the ebb stage of the tide and during slack water. For example, during a wind speed of 5.7 m/s from 246° during a spring tide, τ_w progressively increased throughout the tidal cycle due to a lengthening fetch with the incoming tide (Figure 3.5c). Measurements from aerial photography show that the potential fetch from this wind sector is 3.74 km at HW. Maximum τ_w occurs during the ebb stage of the tide as a result of a balance between fetch length and the amount of time over which the wind has been blowing over this fetch. This modified pattern of bed shear stress prevents deposition at high water creating a greater flux of sediment during the ebb tide. During a higher wind speed (7.6 m/s) over a similar wind direction (258°), the fetch length (3.56 km at HW) becomes less important and so τ_w and τ_{max} increase rapidly during the flooding tide (Figure 3.5e) and the large suspended sediment concentrations at high water (Figure 3.5f) show that wave conditions completely halt any deposition that would have occurred during slack water. During neap tides (Figures 3.5g and h), a lower wind speed (4.6 m/s) from 246° creates a similar pattern of peak suspended sediment concentration to that in Figures 3.5e and 3.5f, albeit of a lower magnitude. The marked reduction in slack water duration observed during these scenarios is due to reduced attenuation of

orbital velocities in shallower waters, meaning that shallow water depths are sensitive to frequent, smaller waves that inhibit sediment deposition around high water. Although no suspended sediment data were available for the T1 deployment, the patterns of τ , τ_w and τ_{max} (Figure 3.7) support those shown by the T2 deployment (Figure 3.5) for both larger wave events (Figure 3.7c) and smaller wave events during both a spring (Figure 3.7b) and a neap tide (Figure 3.7c).

Analysis of the wave data showed that the wave climate at site T1 was more susceptible to changes in wind direction than at site T2. This heightened sensitivity of waves to wind at site T1 results from the site's exposure to different combinations of fetch length and wind direction (Figure 3.1a). In contrast, T2 is generally exposed to the largest overall fetch length that remains coincident and aligned with the prevailing wind direction. This result implies that the region most affected by waves (in terms of sediment movement or 'geomorphological significance') may not be the region with the longest fetch (and therefore the largest waves) but is the region with the most exposure to a range of fetches that generates waves with sufficient energy to mobilise sediment. Although T2 experienced higher H_s , T1 had higher τ_w , which can be attributed to the shallower water depths at T1 and resultant reduced attenuation of orbital velocities (Figure 3.1e).

The influence of wind on general circulation patterns can also be seen at the T2 deployment where a wind from the west (blowing up-estuary) reduces τ during the flood and increases τ during the ebb (Figure 3.5e). To identify the significance of any links between tidal asymmetry and wind circulation, the strength of tidal asymmetry (defined here as the ratio between mean ebb and mean flood current speeds) was compared to wind strength. This comparison shows, a correlation at the T2 ($r^2 = 0.50$, $F = 25.69$, $p < 0.01$) deployment, a weak correlation in the ADP observations ($r^2 = 0.05$, $F = 3.06$, $p = 0.09$) and no correlation during the other deployments. As the higher wind speeds are associated with the fetch aligned winds from the SW and W (Figure 3.2a), the wind driven current should weaken flood currents and / or strengthen ebb currents at the T2 and ADP deployment site. These results indicate that wind-driven circulation is most important over the downwind intertidal areas of the estuarine system.

Within the southern arm, the ADV did not record any waves higher than 0.06 m; most waves (99.5% of the record) were below the significance threshold of 0.05 m meaning that the majority of the record is indistinguishable from the errors introduced in this type of analysis. Therefore any waves within the southern arm of the estuary were too small to be characterised accurately by the ADV. In addition to the small size of measured waves, there was almost no correlation between the wave size and the wind speed or wind direction. The small wave height and lack of correlation with the wind is attributed to the short fetch distance available in any direction for wave generation when compared to the longer and straighter northern arm (Figure 3.2c).

In summary, the flood dominant tidal asymmetry over the intertidal northern arm does not explain the lack of recorded deposition in the sediment plate and sediment cores. Instead, the waves have been observed to reverse the flood dominance in shear stress asymmetry, provided that the water levels are shallow enough and the fetch axis coincides with the prevailing wind direction. The distribution of bed shear stress and suspended sediment concentration shows landward sediment flux (accretion) when driven by tides alone and seaward sediment flux (erosion) when waves and tides occur together. In the sheltered southern arm, no waves were recorded and the historical accretion is likely to be due to the tidally-dominated environment since the timing of maximum velocities makes ebb dominance over intertidal areas unlikely regardless of the strength of the ebb tidal current within the subtidal channel.

3.4 Discussion

3.4.1 Contrasting stable states in the two arms

Absolute long-term morphological stability or “stationarity” (Woodroffe, 2002) is unlikely in any estuary because the hydrodynamic and sedimentological processes that control the pathway to equilibrium are themselves not stable over long timescales. Instead a dynamic equilibrium exists and the perception of stability will depend on the timescale considered. Stable estuarine morphology over a >10 year and <100 year timescale is critical for the development of habitats such as mudflats, mangroves, saltmarsh, seagrass and shellfish beds with the shape of the

stable-form being dependent on the hydrodynamics, sediment supply and any non-linear interactions between these variables (McGlathery et al., 2013). The analysis of hydrodynamic and sedimentological records supports the existence of two alternative pathways to morphological equilibrium within the different arms of a mesotidal, dendritic estuarine system (Whaingaroa Harbour, in New Zealand). Most importantly, the difference in the tidal asymmetry between these two arms does not explain the observed differences in patterns of erosion and accretion. Instead, this work shows that this difference is due to the prevailing wind direction relative to the estuarine morphology, and alignment of the longest fetch. Waves generated on a fetch-aligned morphology promote erosion of intertidal sediments.

Prior research has predicted the net tidal asymmetry (and consequently the pathway to establishing a stable shape) within an estuary from the geomorphological parameters that describe the basin (Friedrichs and Aubrey, 1988, Dronkers, 1986). This approach is advantageous as it allows the quick classification of an estuarine system without detailed hydrodynamic measurements or numerical modelling. However, the analysis in this study shows that the direction of tidal asymmetry and sediment flux can be highly variable throughout an estuary. Therefore, the tidal asymmetry recorded within the main channel does not necessarily provide insight into patterns of erosion and accretion over the intertidal. This result is supported by previous numerical modelling studies of idealised estuarine environments (Robins and Davies, 2010, Hunt et al., 2015 and Chapter 2). The intertidal areas can form a large proportion of an estuarine basin and therefore are a critical consideration when determining if an estuary is a net source or sink for sediments. For example, ebb-dominant channel asymmetry could indicate that the estuary is exporting sediment as a whole, or it could indicate that the estuary is developing channel networks where the tidal channels are eroding at the same time as the tidal flats are infilling. This discrepancy between intertidal and subtidal processes, the spatial variability in tidal asymmetry and the critical role that waves play, can result in the use of a single descriptor of tidal asymmetry for an entire estuary being misleading.

The empirical evidence from this study demonstrates that when conditions are dominated by tidal processes (such as in the southern arm), accretion over the intertidal areas continues despite ebb-dominance in the subtidal channel. We show that accretion is likely to be a direct consequence of the flood dominance that occurs when the intertidal area is inundated at high tide, directing the net flux of sediment landward with settling of sediment on the intertidal during high tide slack water. Flood dominance over the intertidal occurs due to a delay in the onset of maximum flow and can arise if a tidal wave is partly progressive and the timing of the current maxima and water level maximum are somewhere between in phase and in quadrature (Bowers and Al-Barakati, 1997, Hunt et al., 2015 and Chapter 2). The timing in the onset of the maxima in ebb and flood velocity (and τ) is also affected by channelisation and the delay in the propagation of the tidal signal within the intertidal area (Fagherazzi et al., 2008). Modelling using a series of idealised estuarine basins showed how increased sediment infilling and reduced water depths over the intertidal areas of an estuary enhances this intertidal flood dominance (Hunt et al., 2015 and Chapter 2). Hence, in the cases where flood-dominant intertidal occurs, there is no evidence of erosion in the basin as a whole caused solely by the influence of the tide. When there is no net export of sediments from the tidal flats, intertidal stability can only be reached through infilling to a point where either tidal currents are too weak to transport sediments further landward or when mangroves and saltmarshes stabilise the intertidal regions at a species-favourable elevation. The high intertidal areas enhance ebb-dominance in the incised subtidal main channel; this ebb dominance would flush any sediment not deposited on the intertidal out into the adjacent estuary and open coast (van Maanen et al., 2013a). This morphological form is similar to that proposed by Mariotti and Fagherazzi (2013a) and to the convex-up estuary form proposed by previous researchers (Roberts et al., 2000; Waeles et al., 2004, Friedrichs and Aubrey, 1996; Friedrichs, 2011, Kirby, 2000; Kirby, 2002; Mehta, 2002; Bearman et al., 2010, Zhou et al., 2015).

In contrast, the wave-dominated environment (northern arm) shows continued periodic erosion despite stronger tidal currents during the flood stage of the tide. In this case, stability is likely to be reached when opposing forces of erosion (from waves) and accretion (from tides during calm periods) balance to form an

intertidal area over which the water is deeper relative to the tidally dominated environment. Erosion from waves occurs due to a reduction in the time during which water is slack at high tide (preventing deposition) and an increase in suspended sediment concentrations over the intertidal area relative to the channels, thus creating a seaward gradient in sediment flux. Idealised modelling in a series of basins with the same fetch as the northern arm but with varied amounts of intertidal sediment infilling shows that the reduction in slack water at high tide and the increase in average bedshear stress over the intertidal relative to the subtidal are augmented with larger amounts of intertidal infilling (Hunt et al., 2015 and Chapter 2). The contrast in patterns of SSC observed here between spring and neap tides also show that attenuation of orbital velocities with water depth is rapid and very sensitive to subtle changes in depth. The depth at which the intertidal flat stabilises will theoretically be around the depth where the most common wave event attenuates at high water. This wave attenuation allows the deposition of sediment during slack water; the resulting deposition reduces the water depth. When the water becomes shallower, the wave orbital velocities can more easily reach the bottom, thus halting deposition, causing erosion and returning the bed to a lower elevation. Thus, there exists a stable elevation which is determined by a subtle balance between the estuarine fetch and average wind strength (Fagherazzi et al., 2007).

The contrast in intertidal morphology and hydrodynamics between the two instrument transects indicates that increased concavity of the intertidal profile results in reduced erosion and therefore is the stable profile that evolves under the influence of wave processes. The morphology of the northern arm has been summarised as a hypsometric curve (Figure 3.1d) but a comparison of the intertidal profile collected along each instrument transect (Figure 3.1e) shows local morphological variation and a clear contrast between the shape of the two profiles where measurements were collected. At transect T1, the intertidal slope is linear whereas at T2 the slope is more concave in shape; this greater concavity at T2 is indicative of the greater wave exposure at this site. The concave profile at T2 results in a deeper intertidal compared to the profile shape at T1; this greater water depth considerably reduces τ_w and τ_{max} due to the increased attenuation of wave orbital velocities (Figures 3.5 and 3.7). However, the bed substrate may

also contribute to the intertidal shape with T2 being more readily erodible and T1 featuring patches of exposed rock platform and oyster beds.

Modelling of the evolution of idealised funnel-shaped estuarine morphology (Lanzoni and Seminara, 2002) has shown that long-term intertidal stability is reached through estuarine infilling to the point at which no tidal sediment transport is possible as opposed to a switch from flood to ebb dominance ('dynamic equilibrium') as theorised elsewhere (e.g. Pethick, 1994, Friedrichs, 2010). Instead, our observations show that the main hydrodynamic mechanism for controlling the switch between infilled and unfilled intertidal morphologies is provided by short period wind waves (as suggested by Mariotti and Fagherazzi, 2013a). Consequently the amount of sediment infilling over intertidal areas is better explained by the frequency and magnitude of wave generation, with tidally dominated intertidal environments tending to be shallow and accretional and wave dominated intertidal environments tending to be deeper and erosional. Therefore, perhaps somewhat counter intuitively, stochastic wave and wind processes control the intertidal form of the estuary rather than the strength of tidal forcing. Overall, the evidence from this study shows two contrasting pathways to stability in estuarine systems, one in which tides create a stable intertidal morphology through accretion and infilling, and another in which waves create a stable intertidal morphology through opposing processes of erosion (from waves) and accretion (from tides). The ability of waves to maintain this stable equilibrium will also be influenced by sediment supply (Fagherazzi et al., 2006 and Fagherazzi et al., 2007) and in regions with an exceptionally large sediment supply such as the Suriname Coast between the Amazon and Orinoco Rivers, accretion has been recorded despite the erosive affects of wave action (Wells and Coleman, 1981, Augustinus, 1980).

3.4.2 Timescale of processes

The hydrodynamic processes recorded in this research operate over a range of temporal scales. The cumulative temporal effect of these processes is to drive the pathway to a presumed dynamic equilibrium which is different in the two arms of the harbour. A comparison of the timescales over which each hydrodynamic process operates shows a range from frequent, accretional low magnitude changes

through to infrequent, erosional high magnitude changes (Table 3.2). Tides are the most regular of these timescales, creating hydrodynamic process that operate on a semi-diurnal frequency. The tidal asymmetries recorded here suspend less sediment than waves but because they are regular, have been shown by models to become morphologically significant over a long timescale (Lanzoni and Seminara, 2002).

Normally wave conditions are considered to be episodic, but here there is evidence of a consistent daily sea-breeze (~ 5 m/s) (Figure 3.3e and Figure 3.8) whose effect on intertidal sediment suspension will depend on whether the maximum sea breeze coincides with the maximum fetch-depth conditions that maximise wave bed shear stress. Thus, the stable intertidal depth that occurs in fetch-aligned estuaries will be modulated by the interaction between the sea-breeze and the spring-neap cycles. Proportionally, these moderate daily wind events tend to have a greater morphological impact than tides because although they are slightly less frequent, wave action stirs up more sediments than tides alone. The stage of the tidal cycle with which the wind coincides is critical to determine the modification of SSC patterns due to τ_{max} , especially over the intertidal areas, a factor which is often neglected in numerical modelling studies which tend to use a constant breeze over the tidal cycle (e.g. Talke and Stacey, 2008). The size of the waves generated within an enclosed body of water is dependent on the interplay between the fetch and the wind speed. With higher wind speeds, fetch becomes a less critical factor in generating waves (Mariotti and Fagherazzi, 2013b) and waves capable of moving sediment could theoretically be created over even small fetches. During this observation period, only wind events with a speed $\sim < 10$ m/s) were observed and so the potential for wave generation during stronger wind events could not be examined. A higher wind speed (> 10 m/s) may be capable of generating waves even in the sheltered southern arm of the harbour; however, such an event would be infrequent (during only 0.002 % of the long term record) and therefore presumably of low morphological significance. Studies of estuarine environments using field observations and analytical models have shown that local winds create a superimposed residual current (Wong, 1994, Sanay and Valle-Levinson, 2005; Narváez and Valle-Levinson, 2008, Hunt et al., 2015 and Chapter 2). In the shallow areas adjacent to

the main channel, the acceleration from wind drift increases the flow in the same direction as the wind raising the water level downwind and forming a pressure gradient. This pressure gradient returns water against the wind down the channel resulting in a flow that opposes the wind (Wong, 1994; Sanay and Valle-Levinson, 2005; Narváez and Valle-Levinson, 2008, Hunt et al., 2015 and Chapter 2). When modelled in a series of elliptical idealised basins with a similar fetch to the northern arm the current circulation patterns caused by changes in wind direction relative to the estuaries orientation were more apparent than recorded here and strengthened or weakened currents over the intertidal and subtidal either side of a stable node (Hunt et al., 2015 and Chapter 2). Here, the correlation between wind speed and current velocities is not strong, probably because the variability in current speeds depend on the patterns of wind speed and direction but will also depend on spring and neap cycles and the timing of the wetting and drying of morphology around intertidal features such as mussel and oyster beds which are located throughout the fetch aligned (northern) arm of the harbour.

3.4.3 Defining morphologically-active wind conditions

The wind speed threshold at which waves entrain sediment on the intertidal to a greater extent than in the channels (causing a seaward gradient in sediment flux) can be considered to be the point at which waves become “morphologically significant” and can be inferred by comparing τ in the subtidal channel (ADP) to τ_w over the intertidal areas (T2 and T1). When $\tau_w > \tau$, more sediment will be in suspension over the intertidal areas and the advection gradient will be seaward. Furthermore, an increased value of τ_w during slack water will inhibit the deposition of sediments over the intertidal areas. For example, when tidal processes dominate and τ (channel) $>$ τ_w (intertidal) (Figure 3.5a and 3.5b), there are higher concentrations of suspended sediment during the flood tide compared to the ebb. The higher concentrations are partly due to local resuspension by the stronger flood tide and partly due to suspended sediments advected into the study area from the more energetic subtidal channel and the lower intertidal flats following the turbid tidal edge (Mariotti and Fagherazzi, 2012a). In this scenario, suspended sediment is brought onto the intertidal flats during the flood tide and deposited during slack (high) water. This sediment transport process is the effect

that is known as settling lag, and is associated with the landward fining of sediments that is common in many estuaries (Zhou et al., 2015). When waves are included and τ (channel) $<$ τ_w (intertidal), suspended sediment levels are greater over the more energetic intertidal flats and therefore more sediment is transported seaward during the ebb stage of the tide (Figures 3.5d, 3.5f and 3.5h). Waves also shorten slack water preventing the usual deposition of sediments at high water (Figures 3.5d, 3.5f and 3.5h).

Although waves reduce the period of slack water duration and therefore inhibit the deposition of sediments, it is known that wave dissipation can also occur causing sediment to fall out of suspension. However, wave dissipation is restricted to the shallowest parts of the intertidal flats (Green, 2011) and therefore the degree to which fine sediment can accumulate in the upper intertidal in a wave dominated environment depends on the shape of the intertidal and how much space there is between the turbid fringe and the shoreline. If this area is small, it is inundated for such a short time that the sediments do not have a chance to fall out of suspension. When the estuary basin is wave dominated and more concave (such as in the northern arm of the study site) the shallower areas where dissipation is likely cover a smaller proportion of the basin and therefore the possibility of fine sediment accumulation under waves is only small over a wave dominated concave intertidal area. Furthermore, dissipation over the shallow upper intertidal areas will only occur once waves reach a certain size. Smaller waves that will form regularly under even low wind speeds have been shown to be effective at eroding bed sediments even over these shallow areas (Green, 2011) and therefore the shallow areas of a wave dominated environment cannot be considered as exclusively depositional.

Although it is difficult to pinpoint the precise wind threshold at which the change from landward to seaward flux occurs owing to the limited number of wind events recorded here (typically $<$ 10 m/s), we can estimate this threshold by calculating H_s , T_p and τ_w for wind speeds ranging between 1 and 15 m/s using empirically based equations (CERC, 1984 and Soulsby, 1997). The intertidal profile and variability in fetch length (maximum of 5 km) used in this calculation was based

on transect T2 (Figure 3.1b and 3.9b) and the water levels and τ were taken directly from the ADCP. Three representative events were chosen based on a neap (Figure 3.9e), a spring (Figure 3.9d) and an intermediate tidal cycle (Figure 3.9c). Significant wave heights less than 0.05 m and water depths of less than 0.1 m were removed from the calculations so the results could be compared directly to those recorded by the DOBIE wave gauge (Figure 3.9a). These calculations do not consider the contribution of intertidal currents (i.e. τ_w only as opposed to τ_{max}), which is a robust assumption for the purposes of this experiment as τ_w was found to contribute the greatest proportion of τ_{max} during the field deployment (Figures 3.5 and 3.7).

The majority of the intertidal flat experiences a reversal of the advection gradient between the intertidal and the channel when wind speeds reach ~ 10 m/s regardless of the tidal state (Figure 3.9a), thus defining a wind threshold for ‘morphologically-active’ conditions. This threshold varies during either spring or neap tidal conditions due to the relative strength of τ in the channel. A partial reversal, with $\tau_w > \tau$ around slack water is also possible, with ~ 5 m/s required to initiate a noticeable increase in τ_w (Figures 3.9a, c, d and e) relative to τ . Over the deeper parts of the intertidal profile, a wind event that creates a partial reversal (at slack water) during an intermediate tide (Figure 3.9c, when the solid light blue line is greater than the solid thick black line) may create an almost complete reversal if it occurs during neap tides when current speeds in the subtidal channel and water depths over the intertidal are low (Figure 3.9e, compare solid light blue line and solid thick black line). A complete reversal of the sediment gradient is predicted during a wind speed of 5 m/s for all tidal states at the shallower end of the profile (Figures 3.9c, d and e, dashed lines), because the orbital velocities are readily able to reach the seabed. This pattern of greater levels of τ_w over the shallower areas indicates that the upper part of the intertidal will be prone to more frequent erosion even during the weaker wind events. Overall, when winds are weak (~ 5 m/s) the reduction in sediment deposition is controlled primarily by water depth and the timing of the wind event relative to the spring – neap tidal cycle. When winds are stronger (> 10 m/s) the depth or tidal state are no longer an important control and erosion will occur throughout the intertidal profile.

To explore the dependence of the morphologically significant wind conditions on fetch length, the calculation is now repeated for an estuary with the same intertidal profile and wind conditions but a shorter maximum fetch of 2 km (Figure 3.10). This fetch length is similar to the maximum fetch length in the southern arm of the study site. The shorter fetch results in a dramatic reduction of τ_w for all water depths, tidal states and wind speeds, with a stronger wind speed required to create the comparable level of τ_w calculated within the estuary with the longer fetch. The reduction in τ_w is especially apparent for the deeper parts of the intertidal profile which rarely exceed the τ within the main channel (Figures 3.10c, d and e, solid and dotted coloured lines). In this reduced fetch scenario, the deeper parts of the intertidal are rarely disturbed by wave action (low τ_w) and will infill until a shallower depth is reached at which erosion is initiated by waves (high τ_w). This shallowing of the lower intertidal would change the profile from concave to more convex as is observed in the southern arm of the case study site. The generation of small waves capable of increasing τ_w over the shallower intertidal areas is less limited by fetch length; especially at wind speeds > 10 m/s (compare τ_w for dashed lines in Figures 3.9c, d, and e with 3.10c, d and e). Therefore, these waves will theoretically only become “morphologically significant” over the shallow upper intertidal in any estuary independent of the fetch length, or the prevailing wind direction relative to the fetch, when winds exceed 10 m/s.

Previous research has identified links between coastal morphology and the wind climate which is in turn related to the strength of El Niño and La Niña events (e.g. Ranasinghe et al., 2004). Here, sedimentary and climate records were analysed to identify any similar trends of morphological variability in an estuarine environment. If the sediment processes in the contrasting arms of the harbour (Figure 3.1) depend on the differing exposure to wind, then the bed level records in the fetch aligned northern arm should show a long-term correlation with variability in wind direction and speed whereas the bed levels in the southern arm will not. To analyse the longer term climate patterns, records of wind direction and speed covering the bed level measuring period were obtained for the Taharoa weather station from NIWA and the Oceanic Niño Index was obtained from NOAA. The Oceanic Niño Index (ONI) shows the strength of either an El Niño (warm) or La Niña (cool) event in the tropical Pacific using a three-month

running-average of the sea temperature anomaly. NOAA defines an El Niño event as when the temperature anomaly exceeds 0.5°C and a La Niña event when the anomaly falls below -0.5°C . The Taharoa wind data (long record) was modified using Raglan (short record) by determining the fit of the U and V components where the data coincided and applying this fit to the rest of the Taharoa record. The wave generation criteria is based on the wave, wind and suspended sediment data obtained during the fieldwork period and is defined as a wind direction between 180 and 270° (also the longest fetch distance in the northern arm), these events were then binned according to speed and expressed as a percentage of all the records taken during each proceeding 3-month window.

The wind record (Figure 3.11a) shows that south westerly winds are at their most frequent (dark blue line) during the summer season and at their least frequent during the winter season. The strength of the El Niño / La Niña cycle from the ONI (Figure 3.11a, black line) shows that there is a pattern between the strength of the ONI and the frequency of south westerly winds with a strong El Niño event during December increasing the frequency of winds from the sector between 180 and 270° by $\sim 10 - 20\%$ ($r^2 = 0.52$, $F = 19.47$, $p < 0.01$). The seasonality in SW winds and the correlation with the ONI during the summer is only apparent when considering bins that include the lower wind speeds (> 1 , > 2 , > 3 and > 4 m/s). When the morphologically significant wind threshold is exceeded (> 5 m/s, Figure 3.11a, green line) there is no correlation between ONI and wind frequency and no seasonal signal, instead the occurrence of these wind speeds is relatively consistent throughout the record. Winds > 8 m/s are extremely rare ranging between 0 and 6.5% of the record. Overall the winds between $\sim 5 - 8$ m/s are critical as they are not only morphologically significant in the fetch aligned arm (Figure 3.9) but are frequent and consistent enough to generate waves over a regular and non-seasonal scale. At these wind speeds the tidal stage is extremely important due to the magnitude of τ in the subtidal channel and the depth over the intertidal flats, with more erosion during neaps and more accretion during springs (Figure 3.9a).

Although some seasonality is apparent within the sediment record at Whatitirinui Island (Figure 3.11b) where the bed level tends to drop in the winter and rise in

the summer, it was not possible to statistically correlate the south westerly wind frequency and the magnitude of bed change with an acceptable level of significance or confidence due to the poor temporal resolution of the bed-level dataset and the lack of seasonality of morphologically significant (> 5 m/s) winds. The bed level records show two distinct sedimentary environments with the southern tidally dominated arm (Figure 3.1b) progressively infilling with limited periods of erosion. This sedimentation pattern is indicative of gradual sedimentation during slack water, interspersed with erosion from rare wave events during storms where wind speeds are strong enough to overcome the limited fetch. The accretion rate recorded over the sediment plates ranged between 2.4 and 5.3 mm/year with an average of 3.39 mm/year; these rates are close to the long term estimate from sediment cores which estimated 2.5 mm/year since the early 1990s (Swales et al., 2005, Bentley et al., 2014). In contrast, the bed levels within the exposed part of the northern arm are more variable over time but less variable between the plates, with periods of erosion followed by accretion and a net trend of stability or erosion overall. This pattern is indicative of a stochastic or seasonal process, with periods of deposition (tides only) followed by periods of erosion (waves) which depend on the overall wind climate. Previous research in microtidal environments has also demonstrated the morphological significance of frequent small waves compared to occasional storm events where tidal processes are considered to be negligible (Green, 2011). Here we show that waves can also be morphologically significant in mesotidal systems but most importantly that the interactions between wind, tides and waves are of crucial importance when defining this significance within these environments.

Often attempts are made to predict the future morphology of estuaries using a calibrated hydrodynamic process-based numerical model focusing predominantly on the predictable and repeatable pattern of tides. Future changes in sea level from ice melt and thermal expansion can be incorporated into such models by adjusting the tide by the amount predicted by global climate change models (van Maanen et al., 2013b, van Maanen et al., 2015) and relative sea level rise can be accounted for by using the projected local rate of subsidence or uplift based on geological and GPS records. However, the analysis presented here demonstrates that the estuary morphology is also highly sensitive to the wave climate to the

extent that the observed morphological change can be better explained by waves rather than tides and therefore waves need to be considered in predictions of long-term morphology in estuaries. Overall, waves can be considered as a “morphologically significant” process where the prevailing wind direction is oriented to create a sufficient fetch to generate waves under frequently occurring wind speeds.

3.5 Conclusions

The aim of this research has been to investigate the relative morphological significance of tidal, wind and wave processes in a mesotidal estuary using a combination of sedimentological, hydrodynamic and climatic records. The threshold of this morphological significance depends on a combination of magnitude and frequency whereby the generated waves can influence tidal and suspended sediment flux asymmetry on a regular enough basis to control the subsequent infilling over longer timescales. Here, we have shown that waves occur due to winds operating over two distinct timescales, daily (sea breeze) and episodic (storms) and the fetch length is critical when considering the magnitude of morphological response to these wind events. Overall, waves are shown to be more morphologically significant in areas with longer fetches because weaker, more frequent daily winds can generate waves. Conversely the morphological significance over shorter fetch lengths depends on the less frequent perturbations caused by storm events. In the absence of waves, tides invariably cause accretion due to flood dominant currents and deposition around slack water. Therefore, fetch limited systems will accrete except during storm events when wave size is not fetch limited. Water depth is also a critical control on sedimentation, as the short-period waves generated within estuaries are attenuated rapidly with increasing water depth and this water depth varies throughout the spring-neap cycle. Therefore, morphologically significant wave conditions occur under weaker winds in the shallower parts of the estuary and this influence deepens with increased wind speeds.

Morphological predictions made with tidal processes alone are complex with widely diverging morphologies emerging depending on the model and its setup (van Maanen et al., 2013a, Coco et al., 2013); factors such as initial conditions,

sediment grain size or erosion thresholds can greatly impact the predicted morphological form. Including the effects of the wind-wave climate within this already complex modelling approach will be extremely difficult to achieve and will require careful application of the modelling results. The complexity is not only due to the variation in setup parameters (e.g. grid resolution, sediment parameterisation) but also due to the uncertainty of wave impacts on morphology and of future changes to climatic patterns such as those predicted to occur on the west coast of New Zealand. It is likely that future changes in wave generation and wind-driven circulation will need to be incorporated into predictions of estuarine morphology.

Table 3.1 Summary of instrumentation, deployment dates and parameters measured. See Figure 3.1 for locations of instruments.

Instrument	Map ID (Figure 3.1)	Deployment date	Retrieval date	Parameters	Sampling interval (s)	Sampling rate (Hz)	Sampling duration (s)	Averaging duration (s)
Weather Station (Taharoa)	●	10th August 1978	1st January 2013	Wind				
Weather Station (Raglan)	*	30th April 2012	29th September 2013	Wind				
Sontek ADV	◇	24th October 2012	20th November 2012	Currents and water levels	600	1	120	120
				Waves	1800	4	256	NA
Sontek ADP	X	24th October 2012	20th November 2012	Currents and water levels	300	1	120	120
FSI current meter	+ (T1 profile)	16th October 2012	7th November 2012	Currents and water levels	600	5	60	60

Dobie gauge	○ (T1 profile)	16th October 2012	7th November 2012	Waves and water levels	600	10	205	NA
OBS	Δ (T1 profile)	16th October 2012	7th November 2012	Suspended sediment	5	1	1	60
FSI meter	+ (T2 profile)	8th November 2012	26th November 2012	Currents and water levels	600	5	60	60
Dobie gauge	○ (T2 profile)	8th November 2012	26th November 2012	Waves and water levels	600	10	205	NA
OBS	Δ (T2 profile)	8th November 2012	26th November 2012	Suspended sediment	5	1	1	60

Table 3.2: Influences of different hydrodynamic forcing due to frequency, type and magnitude of affect (SSC is suspended sediment concentration).

Frequency	Semi-diurnal	Diurnal	Diurnal	Seasonal
Physical process	Tides	Sea breeze (circulation)	Sea breeze (waves)	Storms
SSC	Small	Small	Large	Very large
Speed of change (based on SSC)	Gradual	Gradual	Rapid	Very rapid
Magnitude of change (relative to frequency, based on SSC)	Small	Small	Moderate	Large
Morphological impact	Accretion	Accretion or erosion	Erosion	Erosion

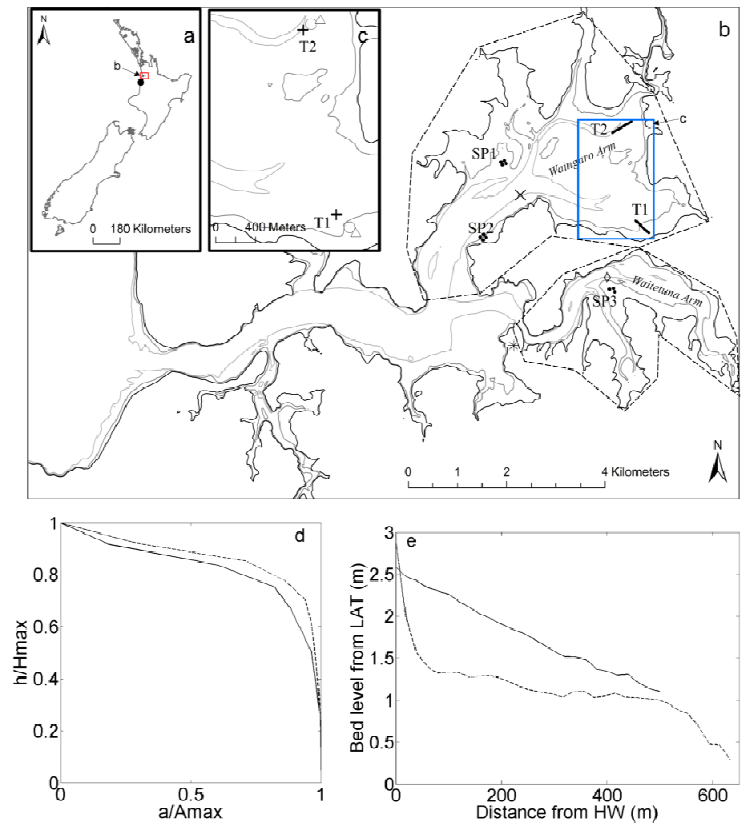


Figure 3.1: Location map showing location of Raglan (red square) and the Taharoa weather station (●) (a) and the field measurement locations (b). Inset (c) shows the area indicated by the blue box. The black, grey and light grey lines show the Highest Astronomical Tide, Mean Sea Level and Lowest Astronomical Tide depth contours. Dots show locations of sediment plate measurements SP1, SP2 and SP3. T1 and T2 show locations of instrument transects consisting of Optical Backscatter (Δ), current meter (+) and Dobie wave gauge (\circ). An Acoustic Doppler Velocimeter (\diamond) was deployed in the southern arm and an Acoustic Doppler Profiler (x) in the northern arm. A weather station was deployed in the main part of the estuary near the mouth of the southern arm ($*$) and the arrow above the scale bar shows the strongest prevailing wind direction (from the SW). The dashed polygons define the approximate limits of each arm and the areas considered in the hypsometry calculations. (d) Hypsometric curves comparing area to height distribution for the northern (dashed thick line) and the southern (solid thick line) arms. (e) Depth profiles at the T1 (solid line) and T2 (dashed line) transects.

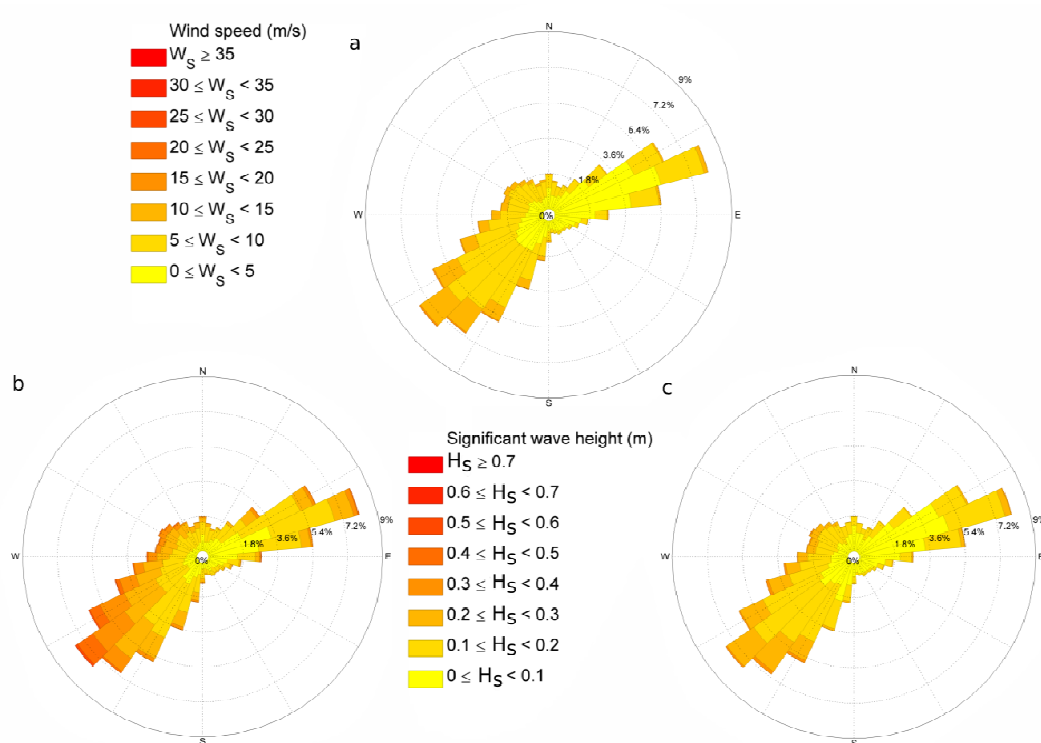


Figure 3.2: Wind rose showing the wind speed (denoted by colour), the wind direction (direction from, denoted by the orientation of the bars) and the frequency of occurrence (denoted by the length of each bar) (panel a), wind data are from Taharoa (see Figure 1a for location) collected between (10th August 1978 and 1st January 2013). Using fetch distances at high water from aerial photography, the wind records are converted into the distribution of predicted wave conditions for the northern (Waingaro) (panel b) and the southern (Waitetuna) (panel c) arms. Significant wave height, wind direction and the frequency of occurrence are denoted by the colour, orientation and length of each bar, respectively.

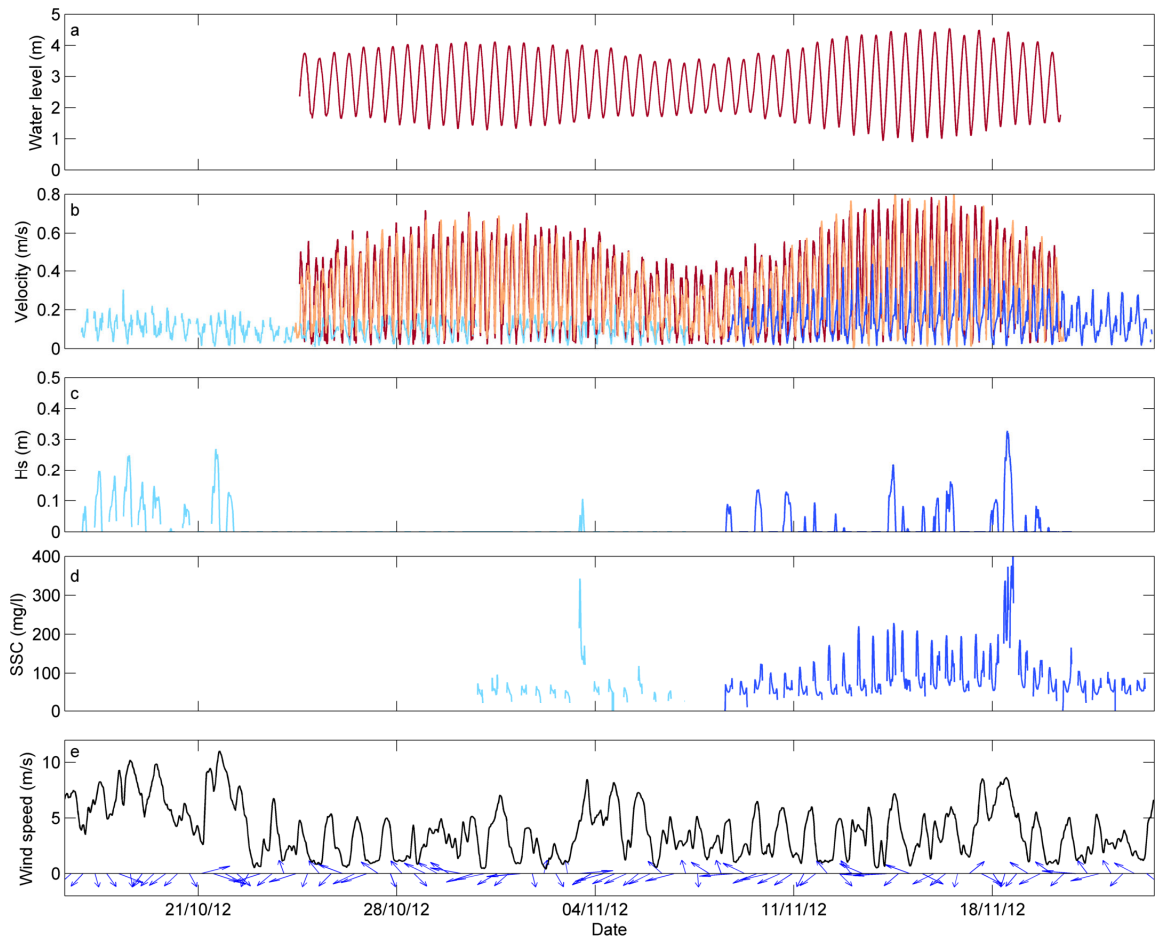


Figure 3.3: Timeseries collected during the field deployment. Locations of instruments are shown in Figure 3.1. Panel a shows water levels from the Acoustic Doppler Profiler (northern arm). Panel b shows depth averaged velocities from the northern arm (Acoustic Doppler Profiler in dark red and T1 and T2 in light and dark blue, respectively), and the Southern arm (Acoustic Doppler Velocimeter orange line). Panel c shows significant wave height at T1 (light blue) and T2 (dark blue). Panel d shows suspended sediment concentration measured using the lower sensor at T1 (light blue) and T2 (dark blue). Panel e shows the wind conditions measured at the Raglan weather station with speed (black line) and direction from (arrows).

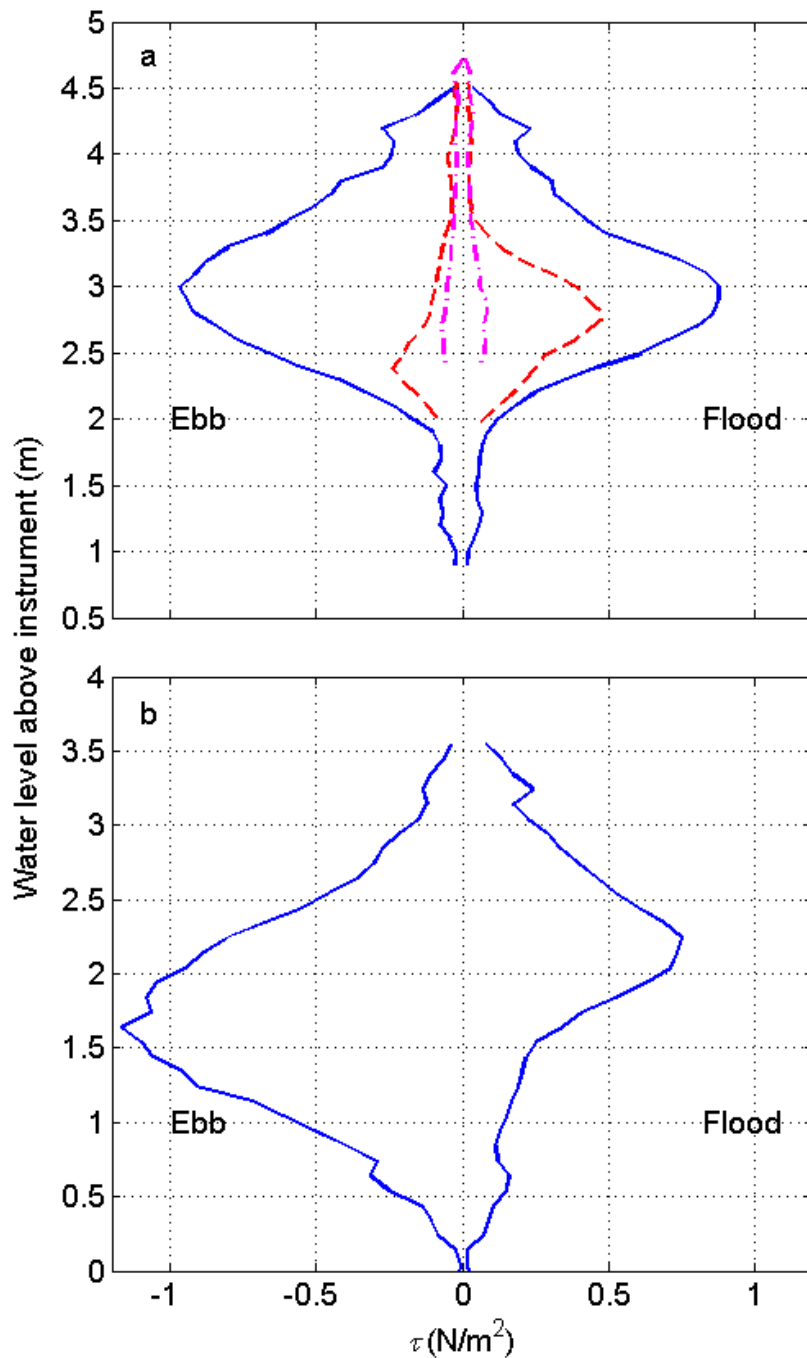


Figure 3.4: Tidal stage figures showing τ (bin averaged over entire deployment, with 0.1 m vertical resolution) plotted for each water level for the northern arm (a): Acoustic Doppler Profiler (solid line), T1 (dash-dotted line) and T2 deployments (dashed line); and the southern arm Acoustic Doppler Velocimeter (b).

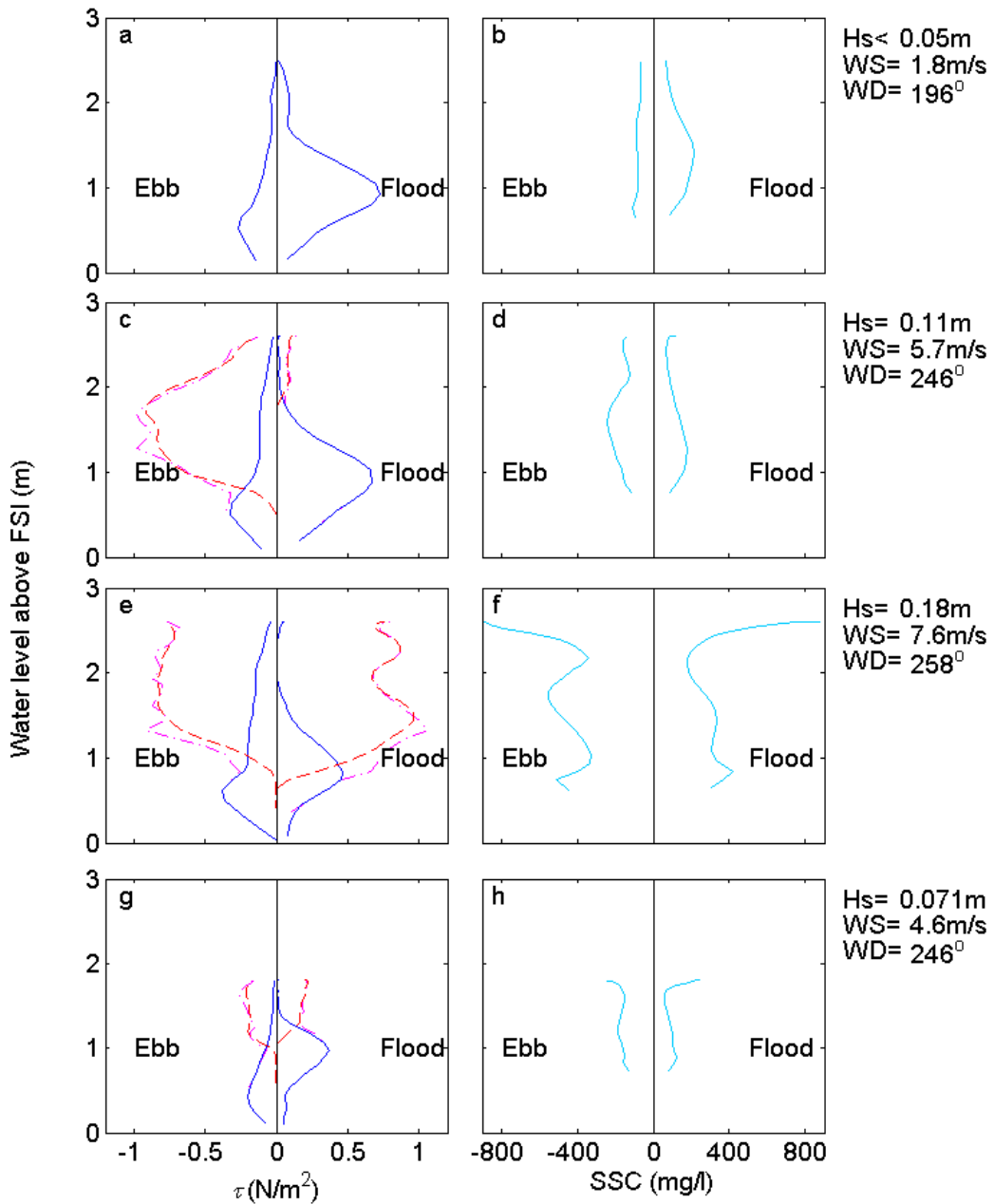


Figure 3.5: Tidal stage figures for (fetch-aligned) T2 deployment showing τ (solid line), τ_w (dashed line), τ_{max} (dash-dotted line) and suspended sediment concentrations (SSC). Cases are shown for a tidal cycle with no waves (a and b), a tidal cycle during a spring tide and a moderate wind speed (c and d), a spring tide and a high wind speed (e and f) and a neap tide with a moderate wind speed (g and h). Mean significant wave height (H_s), wind speed (WS) and direction (WD) are shown for each case.

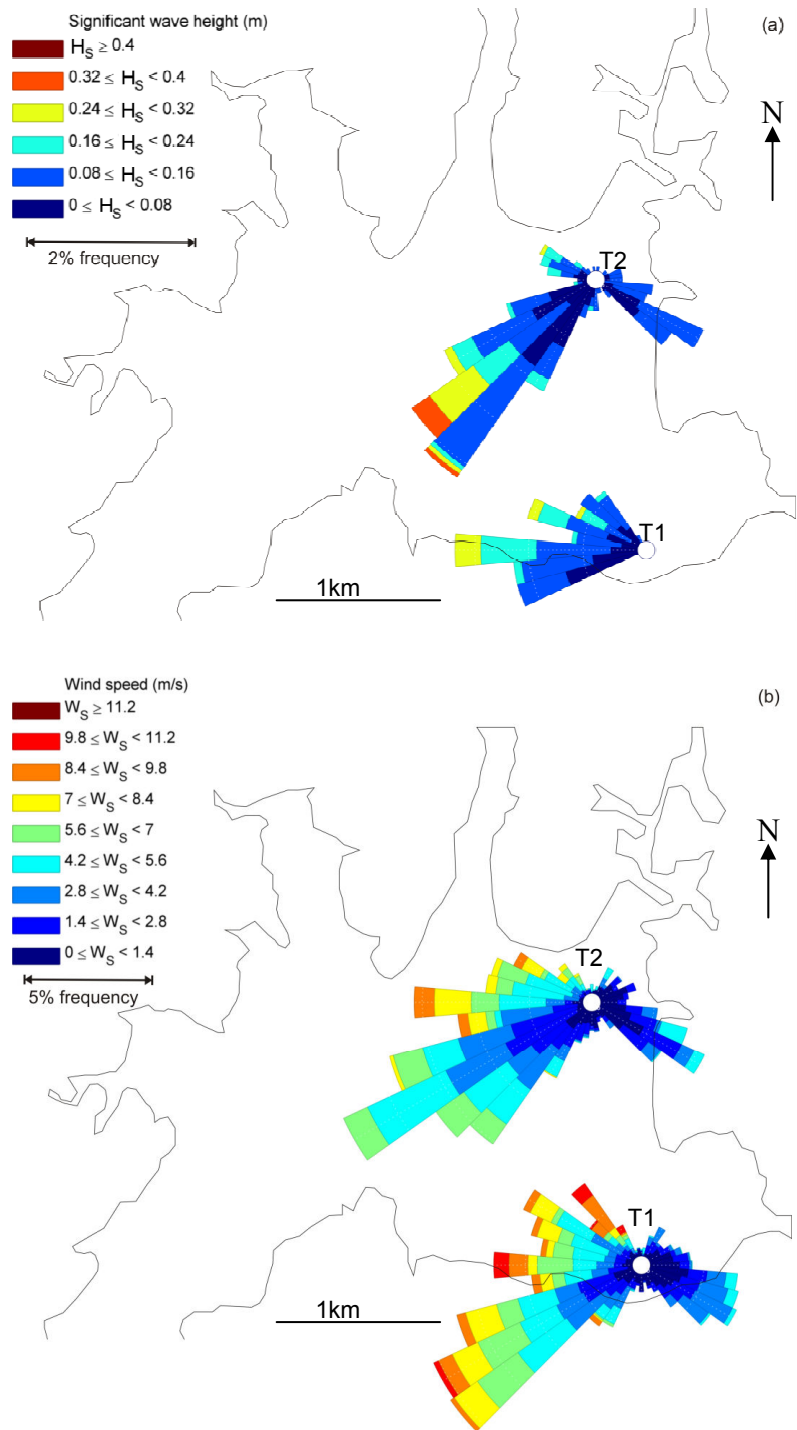


Figure 3.6: Panel a shows significant wave height (denoted by the colour) and frequency of occurrence (denoted by the length of each column relative to the scale bar) for each Dobie deployment. The direction of wind blowing during each wave event is taken from the Raglan weather station and is shown by the orientation of each column. Panel b shows the magnitude, frequency and direction of wind recorded at the Raglan weather station during each deployment.

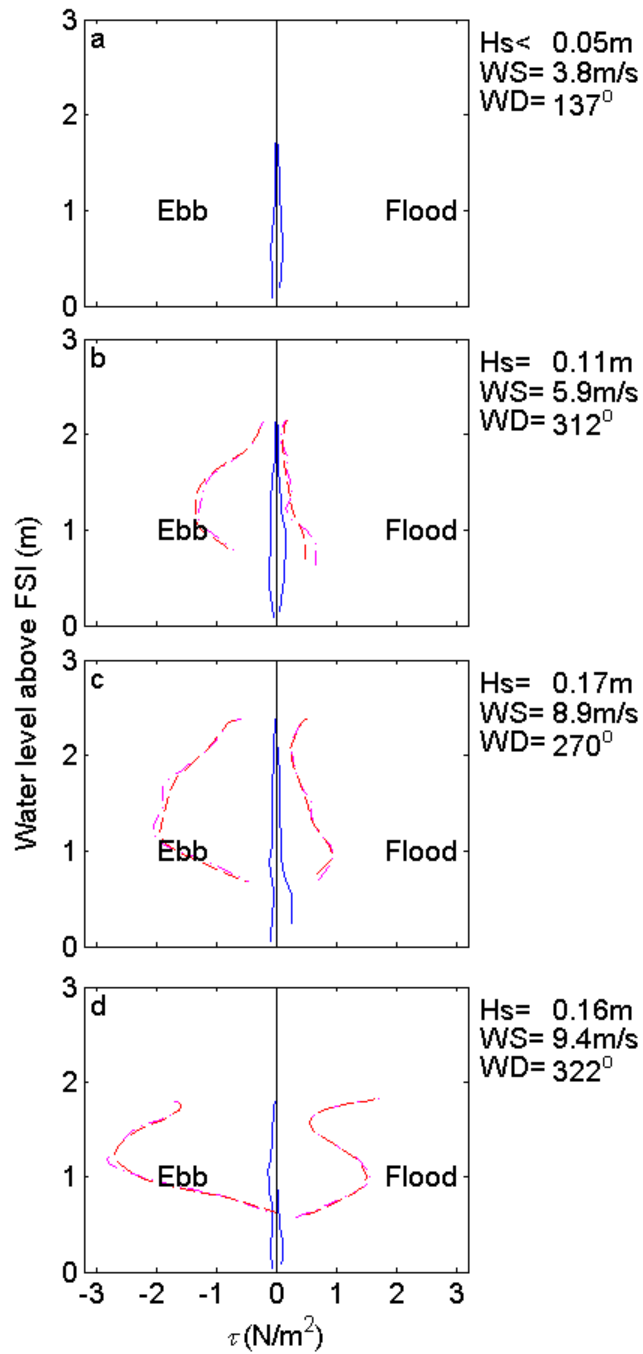


Figure 3.7: Tidal stage figures for the T1 deployment showing τ (solid line), τ_w (dashed line) and τ_{max} (dash-dotted line). Cases shown are for a tidal cycle with no waves (a), a tidal cycle during a spring tide and a moderate wind speed (b), a spring tide and a high wind speed (c) and a neap tide with a moderate wind speed (d). Significant wave height, wind speed and direction are shown for each case. No suspended sediment concentrations are available for the T1 deployment due to instrument malfunction.

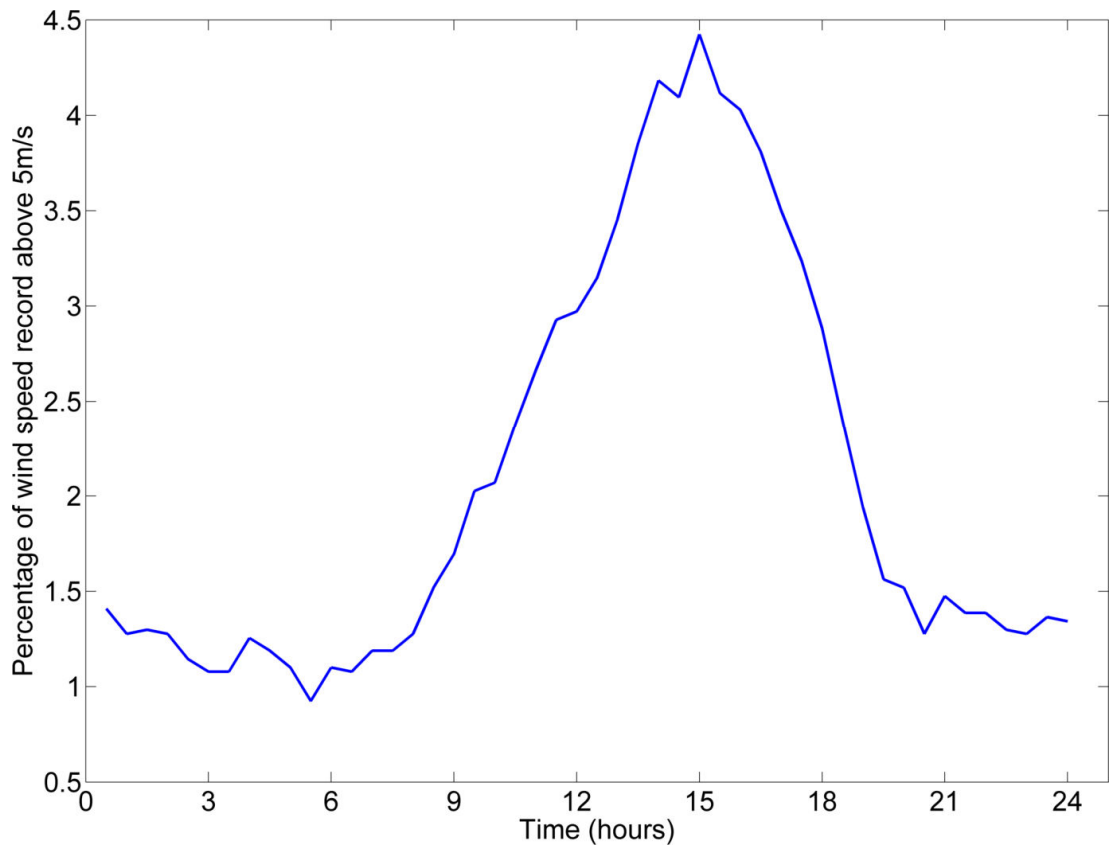


Figure 3.8: Occurrence of wind speeds above 5m/s between 30th April 2012 and 29th September 2013 presented as percentage function of time of day.

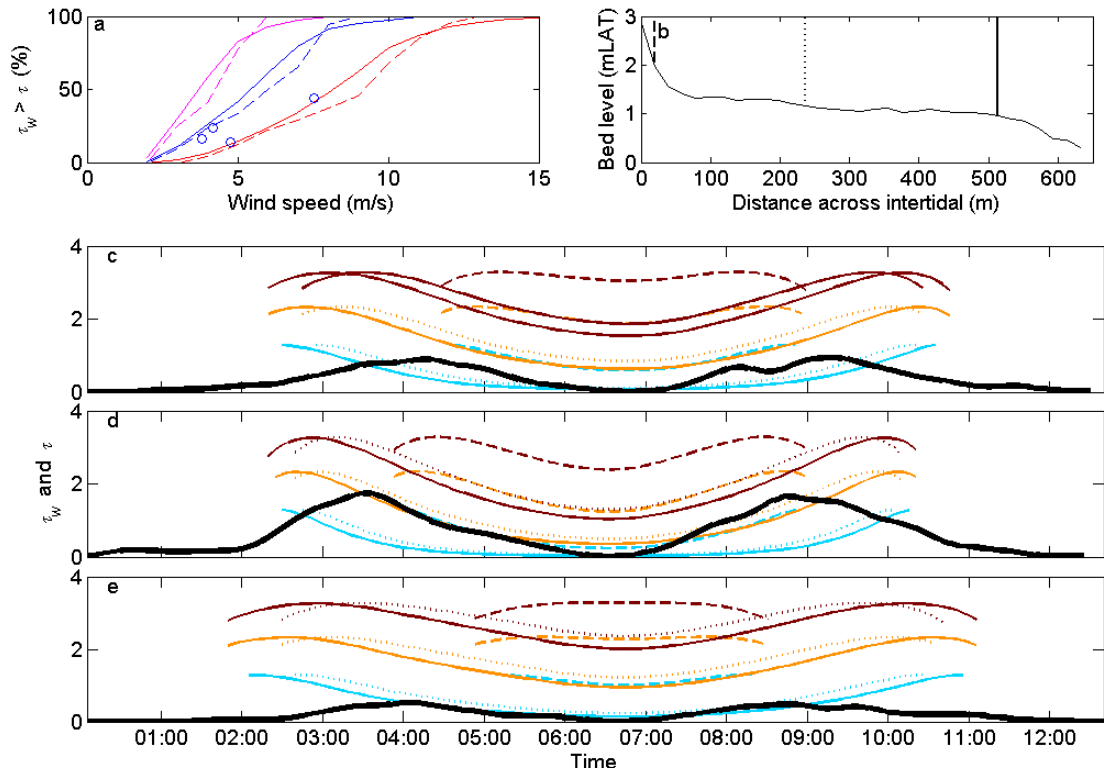


Figure 3.9: (a) Percentage of time when $\tau_w > \tau$ over the entire intertidal area (solid lines) and at the location of the Dobie wave gauge (dashed lines) for neap (magenta), intermediate (blue) and spring (red) tides within an estuary with a maximum fetch of 5 km. Observations from the Dobie wave gauge are shown as circles. (b-d) Timeseries of τ in the channel (solid thick black line) against calculated τ_w (thin coloured lines) for intermediate (c), spring (d) and neap (e) tidal states. Wind speeds shown are 5 m/s (light blue), 10 m/s (orange) and 15 m/s (dark red) at the upper (dashed line), mid (dotted line) and lower (solid line) areas of the intertidal. The lower line is at the same location as the Dobie wave gauge, and the locations of the data points within the intertidal profile are shown in b.

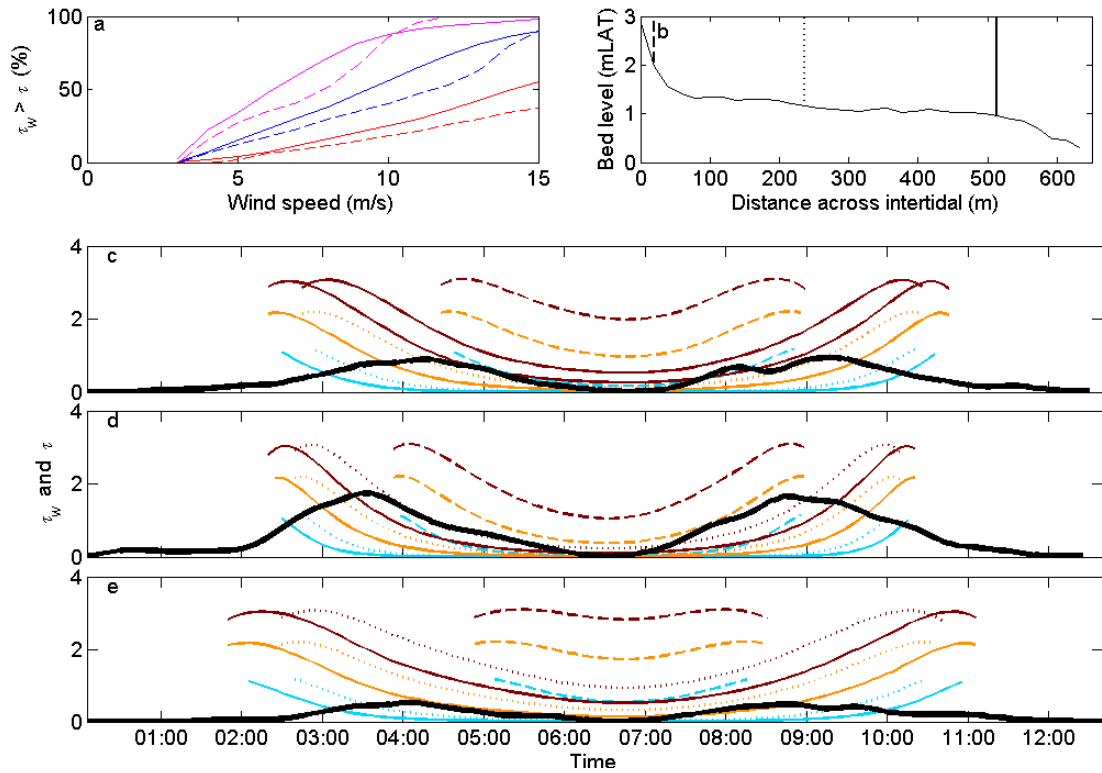


Figure 3.10: (a) Percentage of time when $\tau_w > \tau$ over the entire intertidal area (solid lines) and at the location of the Dobie wave gauge (dashed lines) for neap (magenta), intermediate (blue) and spring (red) tides within an estuary with a maximum fetch of 2 km. (b-d) Timeseries of τ in the channel (solid thick black line) against calculated τ_w (thin coloured lines) for intermediate (c), spring (d) and neap (e) tidal states. Wind speeds shown are 5 m/s (light blue), 10 m/s (orange) and 15 m/s (dark red) at the upper (dashed line), mid (dotted line) and lower (solid line) areas of the intertidal. The locations of the data points within the intertidal profile are shown in b.

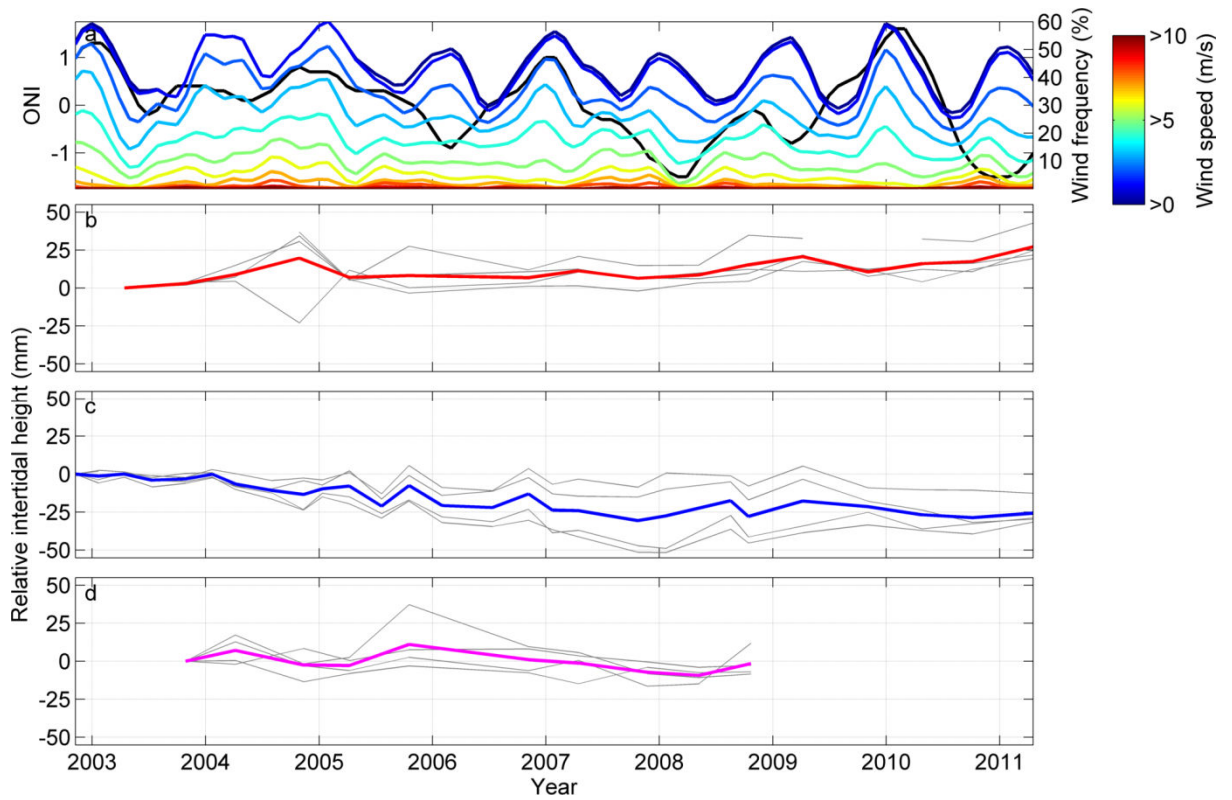


Figure 3.11: Three month running average of NOAA Oceanic Niño Index (ONI, black line), occurrence of south westerly winds (coloured by speed) as a percentage (panel a). Positive ONI denotes El Niño and negative denotes La Niña and the index is considered significant by NOAA when >0.5 and <-0.5 . Sediment plate data showing relative sediment depth (adjusted relative to first measurement) at each plate with coloured line showing mean of results for SP3, southern arm (panel b), SP1 (panel c) and SP2, northern arm (panel d). Wind data are from Taharoa weather station (see Figure 1a for location) modified according to the wind data collected in the Raglan Harbour.

Chapter 4. The effect of wind waves on spring-neap variations in sediment transport in two mesotidal estuarine basins with contrasting fetch.



Upper Waingaro (northern) arm waves, instrument transect T1, Whaingaroa (Raglan) Harbour.

4.1 Introduction

Tides are often considered to be the morphologically significant hydrodynamic process operating within estuaries, controlling the transport and distribution of sediment through tidal asymmetry (Friedrichs and Aubrey, 1988; Friedrichs, 2011). Tidal asymmetry operates through a non-linear feedback process in that the tidal currents are modified by the morphology to change the relative dominance of the ebb and flood tide. This in turn results in more sediment being transported by the ebb (or flood) tide, which consequently means the morphology accretes (or erodes) — the morphological effect of which is to change the ebb-flood dominance, completing the feedback cycle. Sediment fluxes over a tidal cycle can be controlled by three forms of imbalance between processes exporting or importing sediment (tidal asymmetry) (reviewed in Chapter 2, Figure 2.1 and Hunt et al., 2015). Firstly, a difference in the duration of either the ebb or flood part of the tidal cycle can create a greater or more sustained maximum velocity and consequently a larger volume of sediment being transported into (flood dominant) or out of (ebb dominant) an estuary. Secondly, changes to the duration of slack water at high or low tide can affect the amount of fine sediment deposition over the intertidal (high water slack) and subtidal (low water slack) of an estuary. Finally, spatial variations in bed shear stress (τ) can result in a gradient of fine suspended sediment and advection either towards subtidal areas ($\tau_{intertidal} > \tau_{subtidal}$) or towards intertidal areas ($\tau_{subtidal} > \tau_{intertidal}$). All of these tidal asymmetry mechanisms can result in disproportionate erosion or deposition over the intertidal areas relative to the subtidal areas. This variation in sedimentation rates changes the morphology and distorts the progression of high water relative to low water thereby causing further tidal asymmetries. This feedback mechanism is hypothesised to allow estuarine morphology to reach a semi-stable intermediate state between the extremes of unstable flood and ebb dominant states.

Evidence shows that locally-generated wind waves can also exert a significant control on estuarine morphology (Fagherazzi et al., 2007, Mariotti and Fagherazzi, 2013a, Hunt et al., 2015 and Chapter 2, Zhou et al., 2015). Waves are able to directly modify the underlying tidal asymmetry by firstly reducing slack water duration and secondly increasing $\tau_{intertidal}$ relative to $\tau_{subtidal}$ (where the

bed shear stress includes both the effect of tides and waves). Analytical and numerical models have shown that the profile of a wave-dominated intertidal flat will be concave (Friedrichs and Aubrey, 1996, Waeles et al., 2004, Bearman et al., 2010, Zhou et al., 2015) whereas a tide-dominated flat will be convex (Friedrichs and Aubrey, 1996, Roberts et al., 2000; Waeles et al., 2004) and there is some empirical evidence within the South San Francisco Bay to support this theory (Bearman et al., 2010). Previous research has used the concept of a “morphologically significant wind speed” to describe the meteorological conditions required to generate waves of sufficient magnitude and occurrence to change estuarine morphology (Fagherazzi and Wiberg, 2009, Hunt et al., 2016 and Chapter 3). Although strong winds during storms can produce larger waves than are generated during calmer periods, these energetic events occur less frequently. In comparison, although smaller wave events may suspend smaller amounts of sediment over intertidal flats, these smaller events occur frequently and therefore may have a greater impact over a longer time period. Overall, the degree of wave influence has been shown to be highly dependent on estuarine depth, shape and infilling and the orientation of the basin’s fetch relative to the prevailing wind direction (Fagherazzi and Wiberg, 2009, Hunt et al., 2015 and Chapter 2, Hunt et al., 2016 and Chapter 3).

The influence of waves on estuarine morphology has generally been studied in microtidal environments where tidal processes are weak in comparison to wave processes. The presence of waves explains the characteristic bi-modal distribution of depths and distribution of saltmarshes within these environments (Fagherazzi et al., 2007) and even small waves have the ability to affect sediment transport (Green, 2011). Within mesotidal estuaries, the conditions are more complex (Green et al., 1997, Hunt et al., 2015 and Chapter 2, Hunt et al., 2016 and Chapter 3). The tides are proportionally stronger, rarely symmetrical and are capable of transporting considerable volumes of sediment. The larger tidal ranges encountered in mesotidal estuaries also cause substantial variations in fetch and therefore wave size throughout a tidal cycle (Green et al., 1997).

In a tide-only case, it might be expected that more sediment would be mobilised during the higher energy spring tides than during neap tides and therefore spring

tides would be more morphologically significant (Rinaldo et al., 1999, Fagherazzi et al., 2007). However the presence of waves modifies these processes substantially. Wave orbital velocities are attenuated with water depth and conceptual models suggest that the variability in water levels within a mesotidal environment can result in a marked contrast in patterns of erosion and deposition between spring and neap tidal events (Hunt et al., 2016 and Chapter 3). Therefore greater erosion might be expected during a wave event coinciding with a neap tide where orbital velocities over the intertidal are greater and tidal currents in the channel are weak and therefore $\tau_{intertidal} > \tau_{subtidal}$. Conversely during a wave event coinciding with a spring tide, erosion is less likely because the orbital velocities are weakened over intertidal areas due to deeper water and the subtidal currents are greater and therefore $\tau_{subtidal} > \tau_{intertidal}$ (Hunt et al., 2016 and Chapter 3). This switch between erosion and accretion during neap and spring tides has not been described elsewhere and is in direct contrast to previous studies in wave-dominated microtidal estuaries which found more erosion during springs relative to neaps (Fagherazzi et al., 2007). Here, we use field data and numerical modelling to investigate both the spring-neap modulation and the interplay between waves and tidal asymmetry within a mesotidal system to determine whether morphodynamic changes are more likely to occur during spring or neap cycles.

4.2 Study area and numerical modelling

To test how the distribution and magnitude of τ varies in response to changes in wind waves caused by the wind climate, a calibrated numerical model of an estuary with two basins with differing fetch was forced with a range of wind and tidal events. The chosen wind events were based on historic wind data and the orientation of the estuary relative to the wind. The aim of this approach is to understand the probability of occurrence of morphologically significant events, and to determine what type of event (regular versus stronger wind events ('wind events')) is most important in controlling morphological development. The scenarios were designed to incorporate both the most severe (in terms of wave generation) and the most common wind directions.

4.2.1 Case study area

Raglan Harbour is a dendritic flooded river valley situated on the west coast of New Zealand (Figure. 4.1a); tidal ranges are macrotidal during springs and mesotidal during neaps. The tidal prism is $46 \times 10^6 \text{ m}^3$ during springs and $29 \times 10^6 \text{ m}^3$ during neaps (Heath, 1976), both larger than the mean freshwater input to the estuary ($18 \text{ m}^3/\text{s}$, Heath, 1976). Evidence from sediment distribution (Sherwood and Nelson, 1979), sediment cores (Swales et al., 2005), sediment plates (Hunt et al., 2016 and Chapter 3) and hydrodynamic measurements (Hunt et al., 2016 and Chapter 3) has demonstrated the existence of two contrasting morphological environments: the northern (Waingaro) arm and southern (Waitetuna) arm, and that this distinction is entirely related to the degree of wave exposure rather than differing tidal processes. Within the northerly arm (Figure 4.1b), the longest fetch is orientated with the prevailing winds from the southwest (and therefore waves are frequently generated in this part of the harbour), whereas the southern arm (Figure 4.1b) is sheltered from the prevailing winds and consequently wave generation in this part of the estuary is rare (Hunt et al., 2016 and Chapter 3). The distribution of sediments in the northern arm shows coarser sediment grains over intertidal areas and finer sediments within the subtidal channel, and within the southern arm the sediment gradient is reversed (Sherwood and Nelson, 1979). This gradient in sediment size is related to the dominance of either wave or tidal processes with the northern arm experiencing greater hydrodynamic energy at high water (largest fetch and slack water) and the southern arm experiencing greater hydrodynamic energy during the time when flows are restricted to the main channel (smallest fetch and peak tidal velocity). Cores and sediment plates show that the wave-dominated northern arm has experienced almost no contemporary sedimentation for at least the last 150 years, whereas the southern arm has experienced sedimentation rates ranging from 0.35 mm/yr prior to human settlement increasing to 1.1 mm/yr since 1890 (following catchment deforestation), further increasing to 2.5 mm/yr since the early 1990s (Swales et al., 2005, Bentley et al., 2014) and $\sim 3.4 \text{ mm/yr}$ between 2003 and 2011 (Swales et al., 2005).

4.2.2 Field data and numerical model.

The hydrodynamics within the case study area were modelled using the Delft3D open source numerical model. Tidal processes were modelled using the hydrodynamic module and the wind waves were modelled using SWAN (Simulating WAVes Nearshore). Intertidal elevations were measured using LiDAR (recorded by Waikato Regional Council in 2010) and the subtidal depths were measured during a series of bathymetry surveys (single beam, collected in 2008 and 2009 and multibeam, collected in 2014) and navigation charts (LINZ chart NZ4421). The model was run in 2D mode and a rectangular grid with a resolution of 50 m was used. Tides in the model were forced using tidal constituents along the western seaward boundary from the Manu Bay tide gauge (Figure 4.1b) and the waves and wind driven currents were forced using time-series of wind speeds and directions collected during the field experiment detailed below. Freshwater input was very small compared to the tidal prism, and so is not considered significant in comparison to tidal effects (Heath, 1976) and therefore was not included in the model. To model the non-monotonic distribution of τ_w with water depth (Fagherazzi et al., 2006, 2007, Mariotti and Fagherazzi, 2013a, b) wave energy dissipation due to bottom friction, depth induced breaking and whitecapping were included within the model.

To calibrate the model, waves, water levels and tidal current magnitudes were compared to field data (Figure 4.1 and Table 4.1) collected in October and November 2012 (Hunt et al., 2016 and Chapter 3). Within the northern arm of the harbour, waves and currents were recorded over the intertidal using a Dobie wave gauge and a Falmouth Scientific Instruments (FSI) current meter deployed at the Paritata Peninsula (T1) between 16th October and 7th November and then near the Waingaro River Mouth (T2) between 8th – 26th November 2012 (Figure 4.1). All other instruments were deployed between 16th October 2012 and 20th November 2012. Currents and water levels in the subtidal parts of the harbour were recorded using a Sontek Acoustic Doppler Profiler (ADP) in the centre of the northern arm and two InterOcean S4 current meters at the entrance to the arm. In the southern arm waves and currents were recorded using a Sontek ADV

deployed on the edge of the intertidal flat (at the same elevation as low water) and an S4 current meter in the entrance to the Southern arm (the ‘Narrows’).

For the model calibration, the model was run over the same time period as the instrument deployments in the harbour using tidal constituents from the tidal record at Manu Bay tide gauge using T-Tide (Pawlowicz et al., 2002) and a time-series of wind speed and direction recorded at the Raglan weather station (location in Figure 4.1b). A range of uniform bottom roughness (Manning’s roughness coefficients, ranging from 0.15 to 0.40) were tested and the ability of the model to replicate the hydrodynamics was quantified using the hydrodynamic model skill using the ‘index of agreement’ (Willmott, 1981, Warner et al., 2005, Liu et al., 2009, Elias et al., 2012):

$$WS = \frac{\langle (m-o)^2 \rangle}{\langle (|m-\langle o \rangle| + |o-\langle o \rangle|)^2 \rangle} \quad (4.1)$$

where m and o are modelled and observed time-series, respectively, and $\langle \rangle$ denotes a mean. A perfect match between the observed and modelled results would result in $WS = 1$. Comparisons between modelled and observed water levels, current speeds and significant wave height (H_s) and peak period (T_p) showed that an appropriate roughness coefficient was 0.20. For a roughness coefficient of 0.20, WS values within the area of interest ranged between 0.88 and 0.98 for water depths, 0.93 and 0.97 for currents, 0.95 for H_s and 0.68 and 0.73 for T_p . Due to the resolution of the measured data, calibration of wave periods < 0.5 s was not possible.

4.2.3 Analysis of wind data and fetch.

The wind used in the numerical modelling scenarios was based on the historic rate of occurrence and chosen to represent a range of different events from low magnitude high frequency through to high magnitude and low frequency. Local wind data were collected between 30th April 2012 and 29th September 2013 at Raglan Harbour (Figure 4.1b) and a longer wind record (10th August 1978 and 1st January 2013) was obtained from the Taharoa metrological station situated on the open coast 40 km south of Raglan (Figure 4.1a). The similarity between the short-term local wind data and the long-term record was established through

linear regression of the u and v components at each deployment. The Taharoa record was then adjusted using the slope and intercept to achieve the best possible fit between the two records for both u ($r^2 = 0.7802$, $F = 6737.4$, $p = 0$) and v ($r^2 = 0.5107$, $F = 1.980.7$, $p=0$) components. This approach provided the long-term wind record from which the modelled scenarios were selected. The Raglan (Figure 4.2a), Taharoa (Figure 4.2b) and modified Taharoa (Figure 4.2c) records were then binned according to direction (bin size of 10°) and speed (bin size of 1 m/s) and the probability of occurrence within each bin was calculated. The calculations show a strong bimodal distribution with less frequent stronger winds from the southwest (centred on 235°) and more frequent but weaker winds from the east (centred on 80°).

Wind events were then selected for the numerical model scenarios based on this frequency distribution (Table 4.2) in addition to two scenarios chosen to represent less common wind events (wind directions 135 and 315° , which are perpendicular to the longest fetch in the northern arm and the main wind direction, respectively). Tidal conditions along the seaward boundary of the model were described using astronomical constituents derived from the Manu Bay tidal gauge record using the T-tide Matlab function (Pawlowicz et al., 2002). Each wind scenario was simulated in Delft3D over a spring-neap tidal cycle between 6th November 2011 and 16th November 2011, thereby giving a realistic envelope of tidal conditions for the analysis.

Although the assumption that winds would blow consistently for an entire spring – neap cycle is unrealistic, the patterns of wind-driven circulation and wave generation break down as the large intertidal areas are drained with each ebbing tide and therefore the effects of the wind on the hydrodynamics are not cumulative and this approach is considered sufficiently robust for the purposes of this study. Modelling of wind circulation patterns in idealised estuary basin supported by observations from Raglan Harbour indicates that wind circulation is dependent on the depth contrast between intertidal and subtidal areas (Hunt et al., 2015 and Chapter 2, Hunt et al., 2016 and Chapter 3). Acceleration from wind drift increases the flow in the same direction as the wind over the shallower intertidal areas, raising upwind water levels and causing a return current that

flows down the deeper subtidal area in a direction opposing the wind. When the shallow intertidal area drains on the ebbing tide, the circulation pattern breaks down before reforming on the subsequent flooding tide. Furthermore, numerical modelling of a fixed water depth (high tide) and a fixed wind speed (10 m/s) in an idealised basin (Hunt et al., 2015 and Chapter 2) showed that the circulation pattern was rapidly established, with depth-averaged velocities reaching a steady state within 6 hours, considerably shorter than the total duration of uniform wind-forcing (2 days). The steady state of this wind induced circulation current shows that even if the wind circulation pattern did not break down with each tidal cycle, the wind circulation currents do not strengthen in a cumulative fashion with a constant wind speed over time. Waves in an estuary are also highly modified by the flooding and drying of the intertidal areas and the subsequent change in fetch length (e.g. Green et al., 1997). Waves respond rapidly to this change in fetch with maximum wave heights occurring at high tide (and maximum fetch length) and smallest wave heights occurring at low tide (and minimum fetch length) (Hunt et al., 2015 and Chapter 2, Hunt et al., 2016 and Chapter 3). This relationship between wave height and the tidal cycle (and consequently fetch) means that even with a constant breeze, wave height will not increase indefinitely but will be limited firstly by total fetch and secondly by the reduction in fetch caused by the exposure of the intertidal flats during the ebbing tide. The fetch for the selected wind directions at each stage of the tide was measured for all grid cells in ArcGIS using the wind fetch tool developed by the USGS (Rohweder et al., 2012) (Figure 4.3).

4.3 Results

To show the variation in patterns of wave and tidal asymmetry at different stages of the spring-neap cycle, results have been presented for a representative mean (12 hour period) tidal range (~3m, Figure 4.4), neap tidal (~2m, Figure 4.5) and spring tidal range (~4m, Figure 4.6) tides. The results are presented here as a series of tidal stage diagrams (Figures 4.4–4.6); these diagrams show variations in basin-averaged combined wave and current bed shear stress (τ_{max}) plotted as a function of water level for both intertidal (Figures 4.4, 4.5 and 4.6, a and b) and subtidal areas (Figures 4.4, 4.5 and 4.6, c and d) of the harbour in the northern

(Figures 4.4, 4.5 and 4.6, a and c) and the southern (Figures 4.4, 4.5 and 4.6, b and d) arms. In the intertidal regions, a larger proportion of the intertidal area is inundated at high tide relative to the low tide, so that the average τ at high tide is calculated over a greater area at high tide than low tide. These tidal stage diagrams allow the identification of changes in patterns of the three types of tidal asymmetry caused by wind and waves. Firstly, asymmetries in τ and τ_{max} can be identified by comparing maximum velocities during the flood to those during the ebb. Secondly, the length of slack duration can be assessed by comparing the value of τ_{max} around slack high water to the threshold of sediment transport for a given sediment fraction. Finally, suspended sediment gradients between the channels and the intertidal regions, and therefore potential of advection of sediment in either a seaward or landward direction, can be identified by comparing the simultaneous value of τ_{max} over the intertidal and subtidal regions of the model.

In this work, changes to suspended sediment gradients have been entirely attributed to differences in τ_{max} . Suspended sediment concentrations can also be affected by other factors such as the location of a turbidity maximum, water quality and processes of flocculation and deflocculation. Although we do not have measurements to justify neglecting these effects, the catchments and freshwater inputs into the two arms of our case study are very similar, and there is no suggestion in any monitoring reports that the water quality would be any different, yet the morphological changes within the estuaries are very different.

4.3.1 Tides only

When tidal forcing is considered in isolation, the changes to relative size of the flood and ebb tides are entirely driven by the effect of morphology on distorting the tide within the numerical model. In this case, the northern arm (Figures 4.4, 4.5 and 4.6, a and c) exhibits an almost equal spatially-averaged τ during the ebb and the flood tide over both the intertidal and subtidal areas. The southern arm (Figures 4.4, 4.5 and 4.6, b and d) shows a stronger τ during the ebb (ebb dominance) within the subtidal channel. In both arms, the flood maximum occurs closer to high tide and ebb maximum occurs closer to low tide; this effect is more pronounced in the southern arm. This delay in timing occurs when the tide is not

completely standing, but has a small progressive component. This change in asymmetry with stage of the tide means that the upper parts of the intertidal (above ~1.m in the northern arm and above ~0.3 m in the southern arm) are on average always flood dominant in the absence of waves and this change is most apparent in the mid and spring tidal cycles (Figures 4.4 and 4.6).

4.3.2 Tides, winds and waves

Within the subtidal part of the model in both arms (Figures 4.4 - 4.6, panels c and d), the magnitude of τ_{max} is predominantly controlled by the tide rather than the strength or direction of the wind; larger τ_{max} occurs during spring tides (Figures 4.6c and 4.6d) and smaller τ_{max} during neap tides (Figures 4.5c and 4.5d) for all scenarios tested. There are some increases in the subtidal τ_{max} from wind-driven circulation due to set-up at the downwind part of the basin which creates a return current along the subtidal channel against the wind direction (80° and 235° scenarios, Figures 4.4c, 4.5c, 4.6c and 4.6d). These increases in τ are most apparent in both arms when the wind is blowing from the SW (235°). This wind direction pushes the water against the upper edge of the basin, creating a pressure gradient and driving a return flow (Figures 4.4-4.6, cyan line). Although the magnitude of intertidal τ_{max} is partly controlled by the spring-neap cycle, the biggest variations occur due to waves generated over the relatively shallower water depths. For all tidal ranges, the largest intertidal value of τ_{max} occurs during the strongest winds over the longest fetch. For the northern arm, this wind direction is 235° (Figure 4.3a), and 315° for the southern arm (Figure 4.3b). The variability and overall difference of τ_{max} magnitude between each wind direction is smaller within the southern arm than within the northern arm. The orientation of the southern arm (not aligned to the dominant wind direction) results in limited fetch for all of the wind directions modelled here and hence there is little variation in τ_{max} between scenarios (Figure 4.3b).

Overall, the tidal stage diagrams show a distinct separation between the hydrodynamic processes that control the magnitude of τ_{max} in the subtidal (Figures 4.4c, 4.4d, 4.5c, 4.5d, 4.6c and 4.6d) and intertidal parts of the estuary (Figures 4.4a, 4.4b, 4.5a, 4.5b, 4.6a and 4.6b). The magnitude of intertidal τ_{max} is controlled mainly by the waves, whereas the magnitude of subtidal τ_{max} responds

mainly to the spring-neap cycle with some smaller contributions from wind-driven circulation. The temporal asymmetry in each arm delays the onset of maximum tidal velocity and therefore the upper intertidal areas are flood dominant during the spring and mid-point tidal cycle.

4.4 Discussion

Our results show that in a mesotidal basin, the variations in depth range between spring and neap tides are more important than the accompanying fetch changes in controlling the magnitude of τ_{max} and hence the likelihood of erosion or accretion over intertidal areas. When averaged over the intertidal area, any reduction in τ_{max} due to a loss of fetch during a neap tide is insignificant (there is very little difference between the dashed lines in Figure 4.5a and Figure 4.6a), so although the overall fetch provided by the basin orientation and wind direction is important when controlling the magnitude of τ_{max} , the small differences in fetch between the spring and neap cycle are not (Figure 4.3a). This factor along with the minimal contribution made to τ_{max} by tidal currents over the intertidal area (black line in Figures 4.4 - 4.6, panels a and c) means that, for a given wind speed and direction, τ_{max} is approximately the same regardless of whether it occurs during the spring or the neap part of the tidal cycle. For example, the maximum magnitude of τ_{max} over the intertidal is approximately the same during a wind speed of 5 m/s and a wind direction of 235° for both a spring (Figure 4.6) and a neap (Figure 4.5) tidal event in the northern arm. However, larger currents in the subtidal channel result in greater magnitudes of τ_{max} during spring tides so the largest sediment gradient will occur during a wave event (large τ_{max} over the intertidal) and a neap tide (small τ_{max} in the subtidal). Furthermore, the period of slack water at high tide (when sediment should settle from suspension) is reduced more during a neap tide relative to a spring tide, as the shallower water depths at high water allow greater orbital velocities, thus preventing deposition of sediments on the intertidal area when waves are present. Conversely, during spring tides the water depth is deeper and even the larger waves generated as a result of the increased fetch are not sufficiently large to overcome this increased depth. Consequently τ_{max} falls around slack water, increasing the potential for sediment deposition around high water slack during springs. Therefore the greatest potential for reduced deposition

and sediment erosion across the intertidal under wave conditions is during the less energetic neap part of the tidal cycle rather than the stronger tidal currents during springs. The change in regimes between erosive neap and accretional spring events has been previously hypothesised using point measurements and empirical equations (Hunt et al., 2016 and Chapter 3). The present research supports this understanding of this process by considering the effects on the entire basin using realistic wind scenarios.

The magnitude of the sediment flux caused by a gradient between the intertidal and subtidal areas increases with wind speed, so the likelihood of a wind event contributing to morphological change depends on a combination of the frequency of the wave event and the magnitude of its affect. Due to the modulation affect between spring and neap tidal cycles outlined above, a 10m/s wind event during a neap tide is capable of shortening the slack duration and creating a suspended sediment gradient in both arms of the harbour regardless of the wind direction. However, Figure 4.2c shows that the likelihood of a wind > 10 m/s wave from any sector is only 0.002% and therefore is extremely infrequent. When considering a wind event of 5m/s, the overall dimensions of the basin and how they control the fetch length becomes critical when determining whether the intertidal will erode when the wind is from a given direction. In the 5 m/s wind case, erosion is only likely in the northern arm with a 235° wind and a neap or mid-tide. Under all other wind speed scenarios (i.e. ≤ 5 m/s and not from a direction of 235°), the combination of wind speed and fetch is insufficient to cause significant intertidal erosion in the northern arm.

Often the study of coastal environments focuses on high energy events such as spring tides and storm events as they can produce dramatic changes to suspended sediment flux and coastal morphology. However, the research presented here questions this focus in two different ways. Firstly, neap tides rather than spring tides provide conditions that are more favourable to intertidal erosion during wave events. Secondly, large wind (storm) events are less frequent and therefore the influence may be limited when integrated over an annual or decadal scale. Here, the relationship between wind speed and fetch shows that only the rarer higher wind (10 m/s) events will be able to overcome the restriction of limited fetch and

create wave activity that is able to influence the morphology in both arms of the harbour. Although these high wind events may cause a temporary change in morphology, the history of continuous accretion in the fetch-limited southern arm indicates that that these high wind events cannot be considered to be morphologically significant over a decadal timescale. Therefore, waves can only play a role if the fetch is sufficient to allow the generation of waves during more frequent wind conditions such as in the northern arm and a 235° wind direction shown here.

The distribution of basin area above a given elevation is presented as hypsometric curves for each arm of the harbour in Figure 4.7. To allow a direct comparison between basins, the hypsometry is scaled by dividing the basin area above each elevation (a) by the total area (A). Importantly, these hypsometry curves demonstrate that the morphology (Figure 4.7) of the intertidal is such that there is only a small difference in fetch (also shown in Figure 4.3) between the HWN and HWS because of marked steepening of the intertidal above HWN. This morphological form explains why the predicted levels of τ_{max} increase more in response to the shallower water depths encountered during neaps rather than the greater fetch (but deeper water depths) experienced during springs. Furthermore, the hypsometric curves show that the part of the intertidal where the northern arm is deeper than the southern arm coincides with the hypothesised region of reduced deposition during neap tides and waves. The hypsometries of the northern and southern arm are not unusual (Hunt et al., 2015 and Chapter 2) and fall within the ranges quoted elsewhere (e.g. Boon and Byrne, 1981, Moore et al. 2009). This variability in hypsometry provides a link between the modelled potential for enhanced erosion during neaps and the contemporary morphological differences between the two arms. This flattening of the curve between HWN and LWN also has the effect of increasing the concavity of the profile in the northern arm as previous analytical models indicate might occur in such wave-dominated cases (Friedrichs and Aubrey, 1996, Waeles et al., 2004, Zhou et al., 2015), which is also supported by lack of accretion in sedimentological observations from the northern arm (Bearman et al., 2010). It is possible that a positive feedback exists whereby reduced wave activity from a small fetch, increases deposition and the convexity of the intertidal, as seen in the southern arm. This convexity further

reduces the steepness of the intertidal and therefore also the fetch during neap tides, leading to an accelerating process of infilling within a tidally-dominated environment.

The greater likelihood of erosion caused by the combination of waves and neap tides found here is in direct contrast to previous studies in microtidal environments which found that erosion was more likely when waves were combined with spring tides (Fagherazzi et al 2007). This contrast between microtidal and mesotidal systems can be attributed to the differences in tidal range and morphology encountered in these environments. With a smaller tidal range, the hypsometry in microtidal estuaries may be ‘flatter’ and therefore the gains in fetch length during a spring tide are not offset by the relatively small increase in water depth due to the small tidal range. Furthermore, the tidal currents within the subtidal channel of a microtidal estuary are generally smaller than those encountered in a mesotidal estuary. Therefore in a microtidal estuary during wave events, the values of τ_{max} over the intertidal during springs are more likely to be higher than τ in the subtidal channel resulting in a seaward flux of sediment. Moreover, the small tidal range in a microtidal estuary and the low current speeds mean that the ebb currents during a neap tide are unlikely to be sufficient to transport sediment away from the intertidal area whereas spring tidal currents may be strong enough to do so (Fagherazzi et al., 2007).

To generalise these results, a simple model has been created to show the relationship between fetch length, wind speed and water depth. Empirical equations were used to estimate H_s and T_p (CERC, 1984) and calculate τ_w (Soulsby 1997). In Figure 4.8, values of τ_w are presented for wind speeds ranging between 0 and 15 m/s, fetch lengths ranging between 0 and 20 km with two fixed single water depths of 1.5 (representing high water during a neap tide, Figure 4.8a) and 3 m (representing a high water during a spring tide, Figure 4.8b). For reference, the fetch length of 5km and a spring τ_{ref} of 0.4 N/m² and a neap τ_{ref} of 0.2 N/m² have been marked on Figures 4.8a and 4.8b, respectively. These reference points represent the maximum fetch in the northern arm of the harbour (vertical lines) and approximate maximum subtidal basin-averaged values of τ (horizontal lines). When the level of $\tau_w > \tau_{ref}$ then a seaward flux of sediment is

likely for each water depth. A comparison with the Delft3D numerical modelling results shows a good agreement, in that wind speeds of $\sim 5\text{ m/s}$ and 11 m/s are required to initiate seaward transport of sediment during a neap and spring tides, respectively. This calculation clearly shows the importance of reduced water depth in controlling the levels of τ_w relative to τ and the enhanced erosion potential during a neap rather than a spring tide. For a wind speed of 5 m/s to create a seaward flux of sediment during the deeper spring tide case, a basin fetch of $\sim 17\text{ km}$ would be required, whereas in the shallower neap case a fetch of only $\sim 4\text{ km}$ would be necessary.

Similarly, to understand the role of depth changes in controlling τ_w , in Figure 4.9 values of τ_w are presented for fetch lengths ranging between 0 and 20 km for water depths ranging between 0 and 4 m for three wind speeds of 10 m/s , 5 m/s and 2 m/s (Figure 4.9a,b and c). Again, reference lines are plotted to mark maximum fetch encountered in the northern arm of the harbour (vertical dashed lines, Figures 4.9a and 4.9b) and approximate maximum basin averaged values of τ as would be encountered in the subtidal channel during a neap (horizontal dashed lines, Figures 4.9a and 4.9b) and a spring (horizontal dotted lines, Figures 4.9a and 4.9b). In the lowest wind speed of 2 m/s (Figure 4.9c), the values of τ_w are very low regardless of the fetch length, with the largest values occurring during the lowest water depth. The levels of τ_w are so low that only very small sediments would be entrained, any disruption to slack water duration would be limited to the shallowest areas of an estuary and the occurrence of a seaward flux of sediment is unlikely. For the moderate wind speed of 5 m/s (Figure 4.9b), a distinction can be made between the values of τ_w calculated for shallow and deep water cases. For depths $> \sim 2\text{ m}$ the curves are concave in appearance, showing a very slow increase in τ_w with increasing fetch. Even with a fetch of 20 km the calculated values of τ_w are still low in comparison to those found in the subtidal part of the study area during a spring tide. In contrast, for water depths $< \sim 2\text{ m}$ the shape of the curve is more convex with a rapid increase in τ_w as the fetch increases, therefore the magnitudes of τ_w exceed neap subtidal τ for a fetch of $> \sim 5\text{ km}$ and depths $< \sim 1.5\text{ m}$. For the 10 m/s wind speed case (Figure 4.9a) the curve shapes are similar to those for the 5 m/s case with a threshold depth again of around $\sim 2\text{ m}$. Below this depth the curves tend to be more concave and above this depth the

curves tend to be more convex. The critical difference between the 5 m/s and the 10 m/s cases relates to the overall magnitude of τ_w for the equivalent water depth, which is far higher than in the 5 m/s case.

Orbital velocities and τ_w attenuate with depth, and so are generally greater in shallower water in our simple modelling. However, the relationship between τ_w and water depth is non-monotonic in that, as wind speeds get stronger, and waves get larger, the peak in τ_w occurs at a progressively deeper water depth due to frictional dissipation in very shallow water. To show this, τ_w has been plotted against water depth for fetch distances ranging between 0 and 20 km during a 10 m/s (Figure 4.10a), a 5 m/s (Figure 4.10b) and a 2 m/s (Figure 4.10c) wind event. Although Fagherazzi et al., (2006, 2007) and Mariotti and Fagherazzi, (2013a, b) have used a slightly different formulation for estimating τ_w , our results show the same decrease in τ_w in very shallow water.

This non-monotonic response is also exhibited in Figure 4.9 where during a wind speed of 10 m/s (Figure 4.9a) and a fetch of 5 km (indicated by vertical dashed line) waves generated at depths $< \sim 0.4$ m reach a lower maximum τ_w than those waves generated in depths > 0.4 m despite an increase in fetch. This affect is less pronounced for the lower wind speeds of 5m/s (Figure 4.9b) and only influences depths $< \sim 0.2$ m. The affect of the non-monotonic response is considered within the Delft3D model and is restricted to the shallowest depths, which are in general shallower than much the basins in our case study in Raglan (Figure 4.7), and so the non-monotonic variation of τ_w with depth probably plays very little role in modifying the morphology. Figure 4.10 shows that there is a very notable difference in τ_w between large and small fetch estuaries (Figure 4.10 a.) for strong wind events, whereas the difference is small in the case of light winds (Figure 4.10c). Moreover, the range of depth over which τ_w is large enough to influence morphology is far greater during the stronger wind conditions.

Overall, the conceptual picture presented in Figures 4.8 – 4.10 demonstrates that in a mesotidal basin with moderate wind speeds of around 5 m/s the difference between erosion and accretion during neap and spring tides is likely to occur in basins with fetches ranging between 5 and 20 km in length. The threshold depth between erosion and accretion is ~ 1.5 m, which corresponds to the threshold

between spring and neap tidal ranges in our case study. In mesotidal basins with lower wind speeds or less fetch, waves may have a limited local effect on fine sediments in shallow water but cannot be considered morphologically significant. For winds over 10 m/s the spring to neap switch between accretion and erosion will be less apparent as waves are a significant process in water depths up to 2.5 m with a 5 km fetch. For a fetch of ~ 8 km and a wind speed of 10 m/s waves will be morphologically significant for all water depths and tidal states in the examples tested here.

Finally, we simulate the effect of wind-set up in the estuary (which is included in the Delft3D numerical model) by modifying the water depths used in the analytical model. We have not considered regional storm surge at all in our case study numerical model or in the analytical model since storm surges are generally small along this coastline. Moreover, the effect of a generally-elevated water level can be inferred from the results of our analytical model. Local wind set-up is calculated assuming a simple constant wind stress along the main axis of the estuary and takes into account wind speed and fetch length (e.g. CERC, 1984, Wong, 1994 and Hsu et al., 1997), and we are assuming that our τ_w calculations are for the down-wind side of the estuary, and so we neglect spatial variations in set-up. The calculation initially uses two fixed water depths of 1.5 (neaps, Figure 4.11a) and 3 m (springs, Figure 4.11b) with wind speeds ranging between 0 and 30 m/s and fetches ranging between 0 and 20 km to calculate τ_w (Figure 4.11, solid lines). The calculation was then repeated for the set-up using the water depths that have been modified to incorporate this wind set-up effect (Figure 4.11, dashed lines). Overall the increase in τ_w from the large wind speeds is mitigated slightly by the greater water depths from wind set-up and this reduction in τ_w increases with both wind speed and fetch (and greater wind set-up). However, the reduction in τ_w is unlikely to significantly impact sediment transport because the rate of decrease in τ_w from wind set-up would be greatly offset by the increased wave activity with values of τ_w well above those required for sediment transport.

This research shows the importance of water depth in controlling τ_w , especially during moderate wind speeds of ~ 5 m/s; the timing of wind and water level changes is critical and requires consideration when modelling an estuarine system.

However, because the timing of the interaction between winds and tidal states is complex and depends on a combination of sea breeze, weather and climatic patterns (Hunt et al., 2016 and Chapter 3) joint probability analysis would be required in engineering and environmental studies. The requirement for a joint probability analysis could be estimated in the early stages of a project through a comparison of wind speeds and directions with fetch lengths. The evidence and analysis presented here suggests that in a mesotidal estuary a fetch > 5 km with a wind speed of ~ 5 m/s is sufficient for waves to be considered as a morphologically significant process alongside tides.

4.5 Conclusions

Mesotidal estuaries can exhibit considerable variations in tidal range between spring and neap tidal cycles. These variations modify both wave fetch and water depth and these two parameters are crucial in determining τ_w as orbital velocities decay with depth but increase with fetch length. When comparing wave generation during spring and neap tidal stages, the changes in depths are more important than fetch. Therefore the shallower neap water depths over the intertidal along with lower currents in the subtidal channel make erosion from waves more likely and deposition less likely during neap events as opposed to the more tidally active spring events.

The morphological, meteorological, hydrodynamic and sedimentary evidence presented here shows that given an adequate fetch length and a frequent wind of a sufficient speed waves should be considered as a morphologically significant process. Based on the analysis presented here a fetch threshold of 5 km and a wind speed threshold of ~ 5 m/s is suggested; at and above these thresholds waves will form a dominant morphological process in mesotidal estuaries.

Table 4.1: Modelled wind scenarios.

Wind sector in record	Wind speed in record	Percentage of wind record	Modelled wind direction	Modelled wind speed
65 – 95	1-3	15.27	80	2
	4-6	1.86	80	5
	9-11	0.031	80	10
215 -255	1-3	9.4	235	2
	4-6	9.26	235	5
	9-11	0.085	235	10
N/A	N/A	N/A	135	2
	N/A	N/A	135	5
	N/A	N/A	135	10
N/A	N/A	N/A	315	2
	N/A	N/A	315	5
	N/A	N/A	315	10

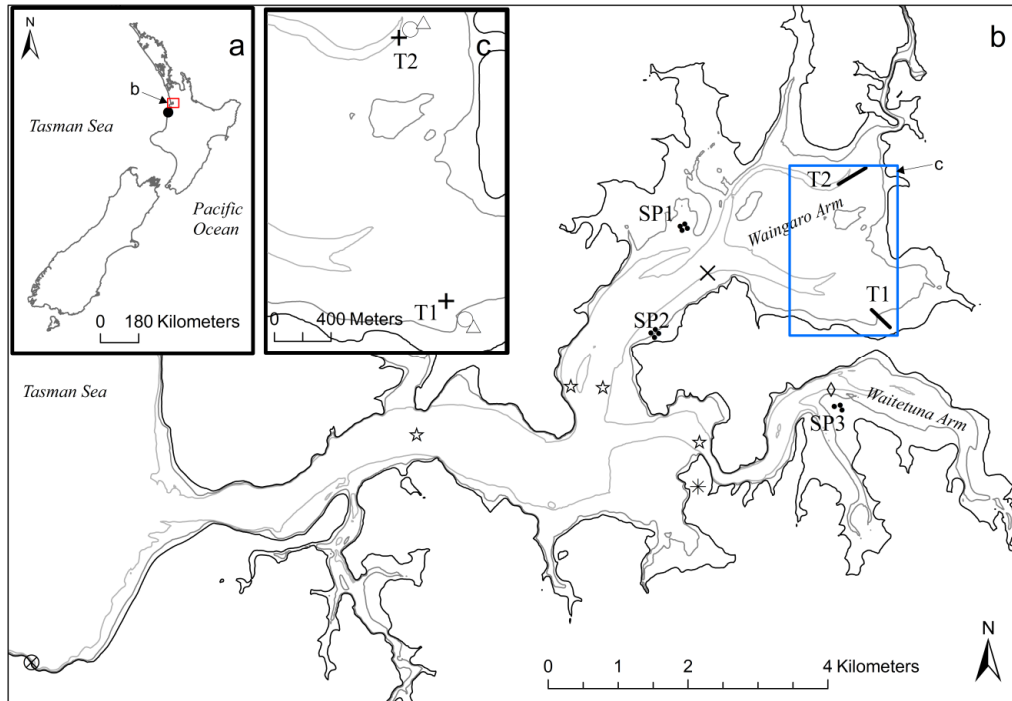


Figure 4.1: Location map showing location of Raglan (red square) and the Taharoa weather station (●) (a) and the field measurement locations (b). Inset (c) shows the area indicated by the blue box. Model extent is same as b (red box in a). The black, grey and light grey lines show depth contours of the Highest Astronomical Tide, Mean Sea Level and Lowest Astronomical Tide. Dots show locations of sediment plate measurements SP1, SP2 and SP3. T1 and T2 show locations of instrument transects consisting of Optical Backscatter (Δ), current meter (+) and Dobie wave gauge (\circ). An Acoustic Doppler Velocimeter (\diamond) was deployed in the southern arm and an Acoustic Doppler Profiler (x) in the northern arm. S4 current meters were deployed in the main part of the estuary and at the mouth of the northern and southern arms (\star). Boundary tidal conditions were taken from constituents extracted from observation from the Manu Bay tidal gauge (\otimes).

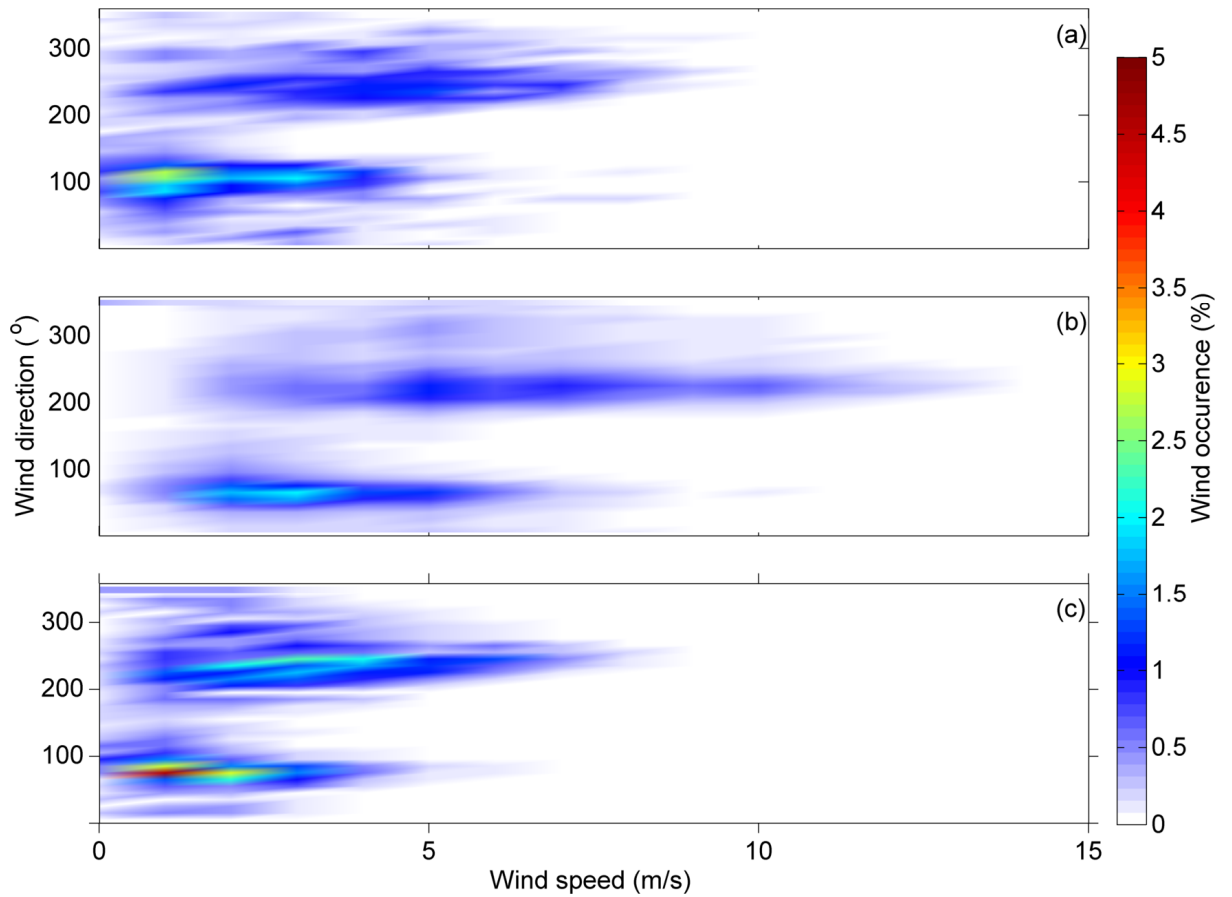


Figure 4.2: Frequency distribution of wind using the observations collected at Taharoa (see Figure 1a for location) recorded between 10th August 1978 and 1st January 2013 (a) and at Raglan (see Figure 1b for location) recorded between 30th April 2012 and 29th September 2013 (b). The long term record used to describe wind conditions within the model simulations was based on a linear relationship between records at Taharoa and Raglan (c), see text for details.

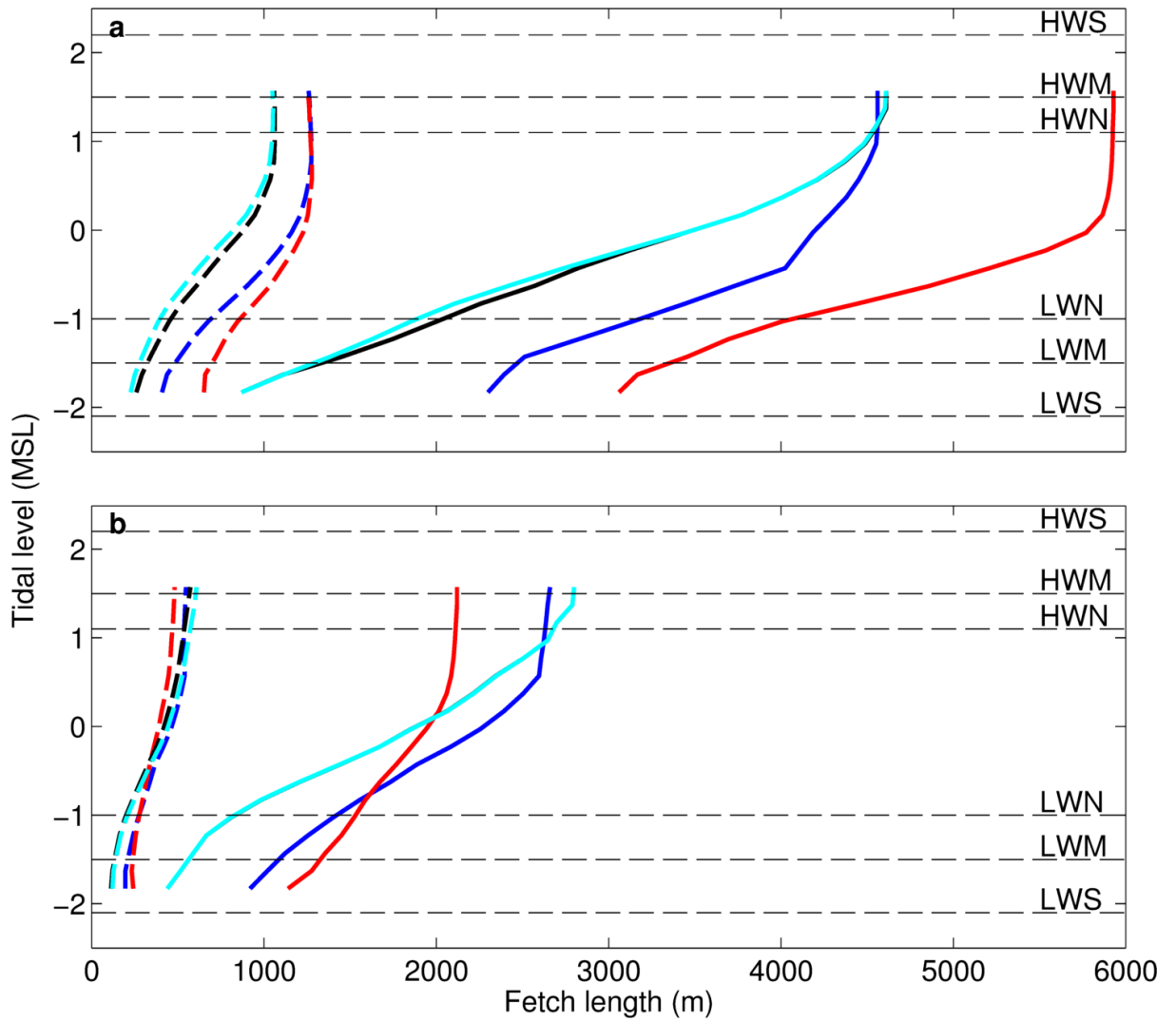


Figure 4.3: Fetch distribution with depth within the northern (Waingaro) arm (a) and the southern (Waitetuna) arm (b) for wind directions of 80° (blue line), 235° (red line), 135° (black line) and 315° (cyan line). Solid lines show maximum fetch within each basin and dashed lines show average fetch over entire basin. Horizontal dashed lines show tidal heights in Figures 4.4, 4.5 and 4.6.

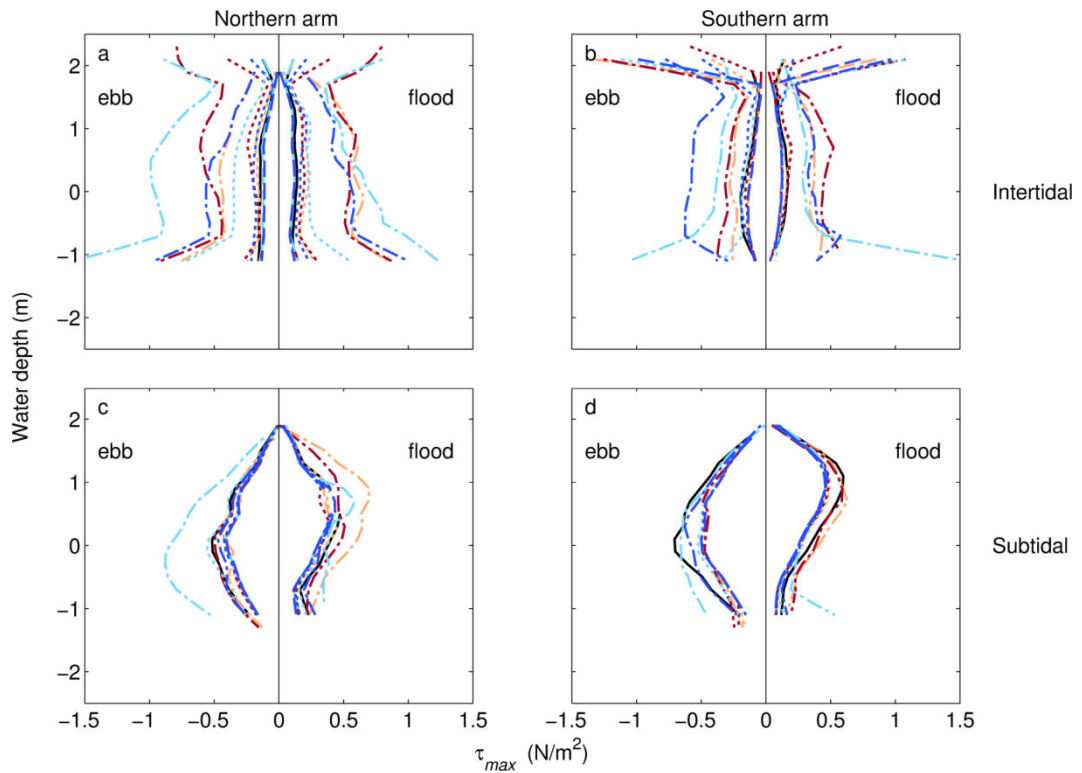


Figure 4.4: Tidal stage diagrams for a tide only scenario (black line), an 80° (orange line), 135° (dark red line), 235° (cyan line) and 315° (dark blue line) wind direction and a 2 (dashed lines), 5 (dotted lines) and 10 m/s (dash-dot lines) wind speeds. The tidal state shown here is for a single tidal cycle midway between a spring and a neap. The level of τ is averaged over the intertidal (a) and subtidal (c) in the northern (Waingaro) arm and the intertidal (b) and subtidal (d) in the southern (Waitetuna) arm.

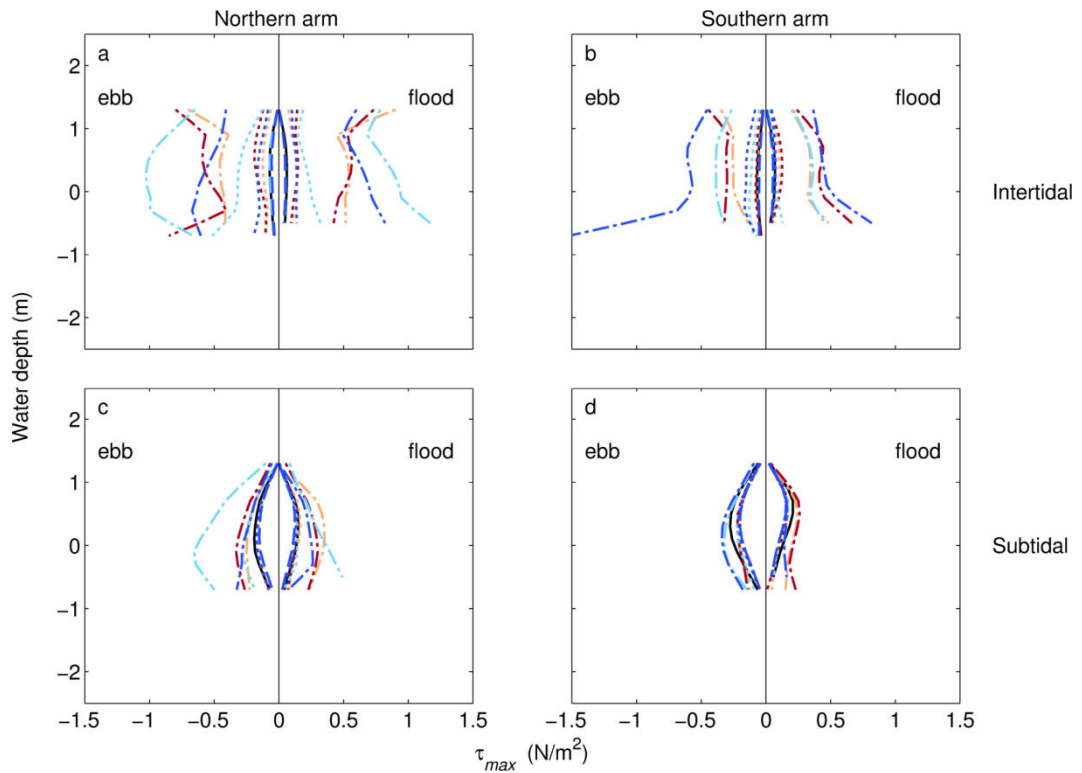


Figure 4.5: Tidal stage diagrams for a tide only scenario (black line), an 80° (orange line), 135° (dark red line), 235° (cyan line) and 315° (dark blue line) wind direction and a 2 (dashed lines), 5 (dotted lines) and 10 m/s (dash-dot lines) wind speeds. The tidal state shown here is for a single neap tidal cycle. The level of τ is averaged over the intertidal (a) and subtidal (c) in the northern (Waingaro) arm and the intertidal (b) and subtidal (d) in the southern (Waitetuna) arm.

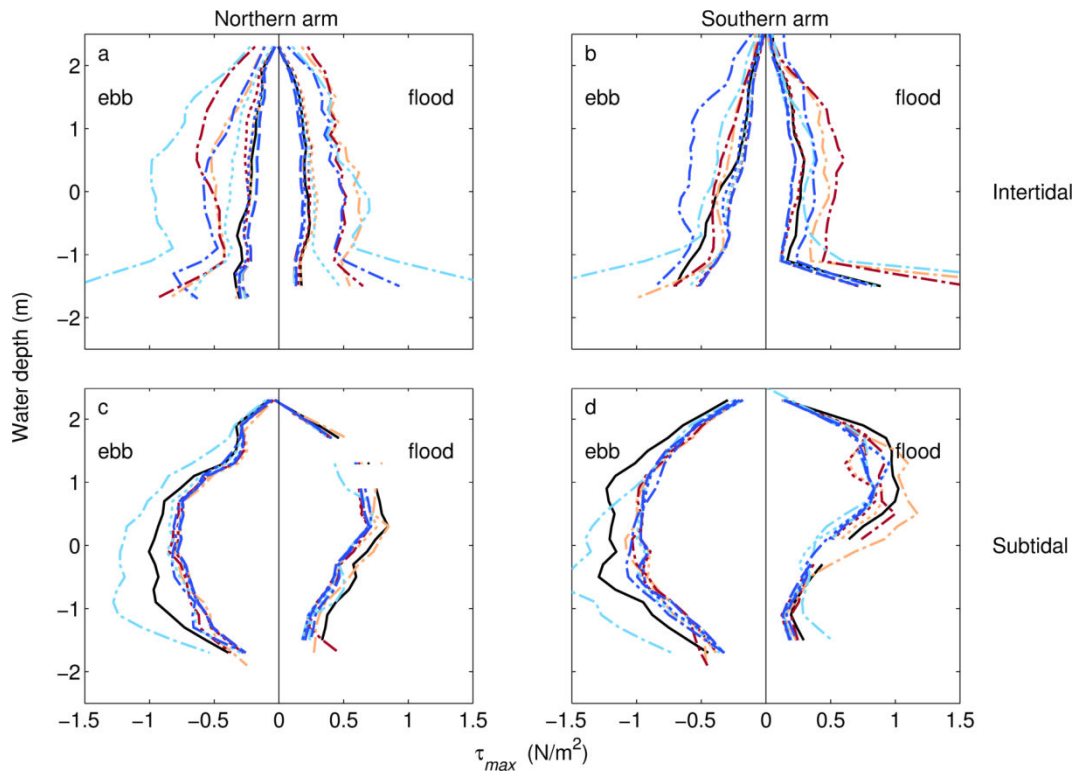


Figure 4.6: Tidal stage diagrams for a tide only scenario (black line), an 80° (orange line), 135° (dark red line), 235° (cyan line) and 315° (dark blue line) wind direction and a 2 (dashed lines), 5 (dotted lines) and 10 m/s (dash-dot lines) wind speeds. The tidal state shown here is for a single spring tidal cycle. The level of τ is averaged over the intertidal (a) and subtidal (c) in the northern (Waingaro) arm and the intertidal (b) and subtidal (d) in the southern (Waitetuna) arm.

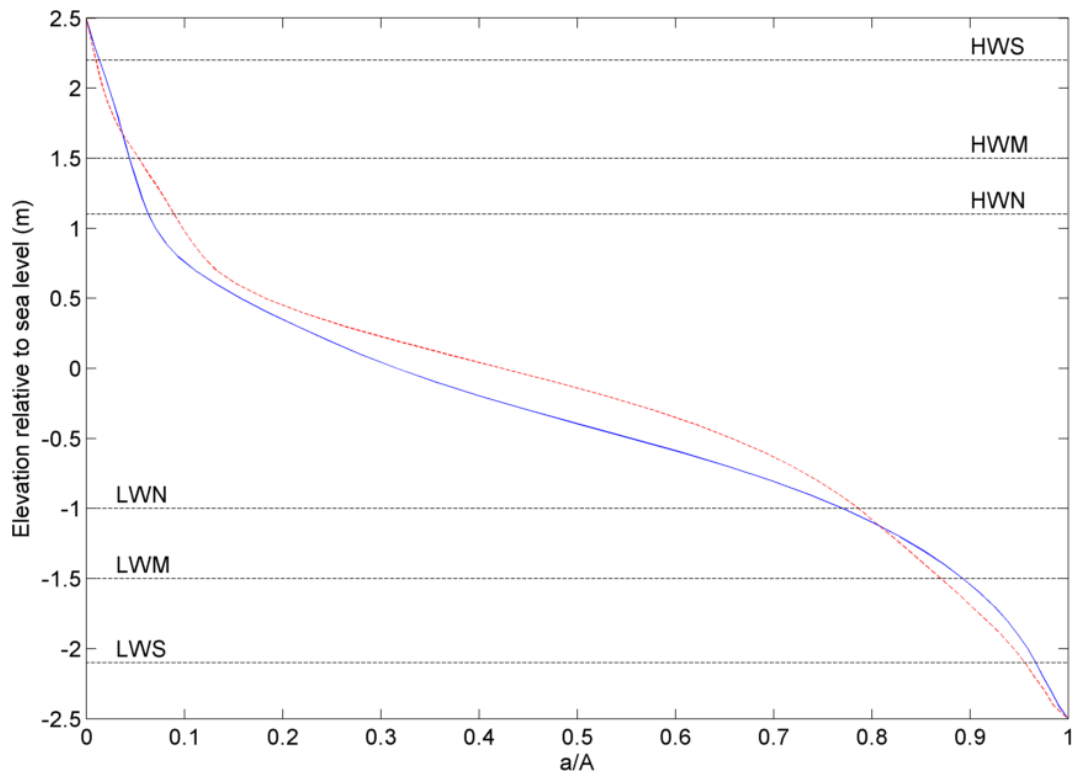


Figure 4.7: Hypsometry of the northern arm (Waingaro: solid blue line) and the southern arm (Waitetuna: dashed red line) between 2.5 and -2.5 mMSL. To enable comparison between the different-sized arms the area is scaled by dividing area above specified elevation (a) by maximum overall basin area (A). Horizontal dashed lines show the locations of high water springs (HWS) and low water springs (LWS) in Figure 6; high water mid (HWM) and low water mid (LWM) in Figure 5; high water neaps (HWN) and low water neaps (LWN) in Figure 4.4.

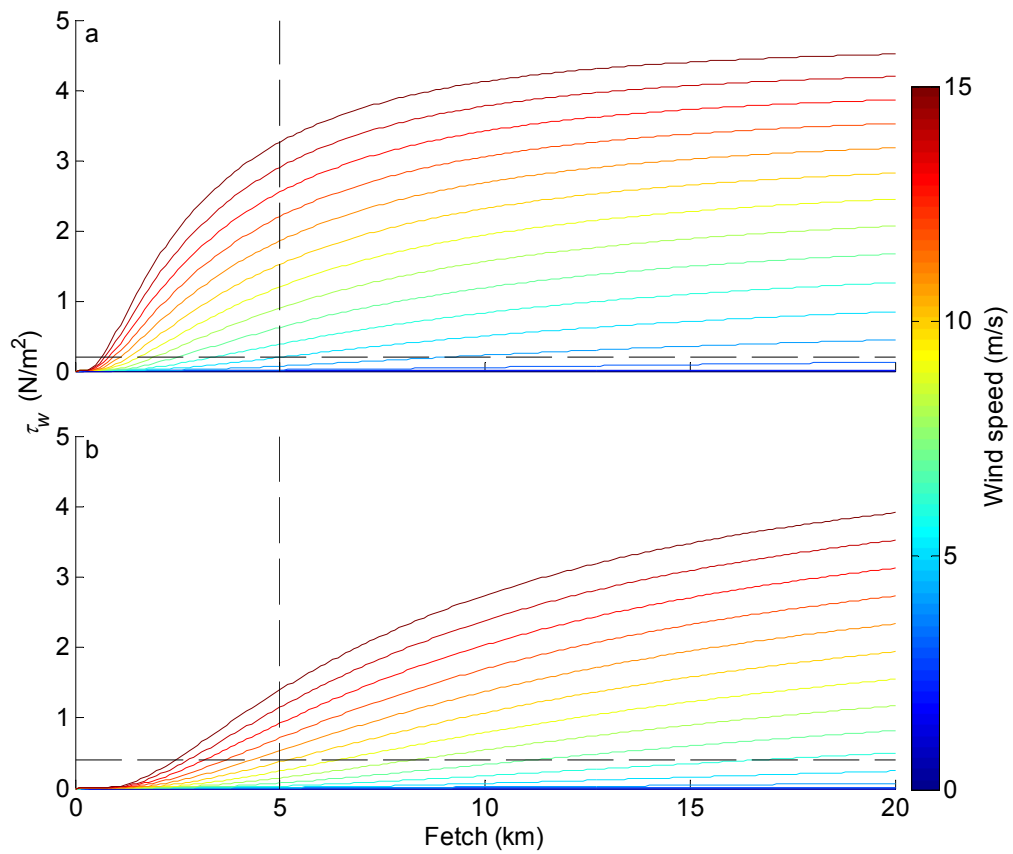


Figure 4.8: Values of τ_w for a range of wind speeds and fetches for a single fixed typical neap (1.5 m, a) and spring (3 m, b) water depth. The vertical black dashed lines represent maximum fetch length in the northern arm of the case study site. The horizontal black dashed lines represent approximate maximum basin averaged values of τ in the subtidal channel from the Raglan Harbour numerical model.

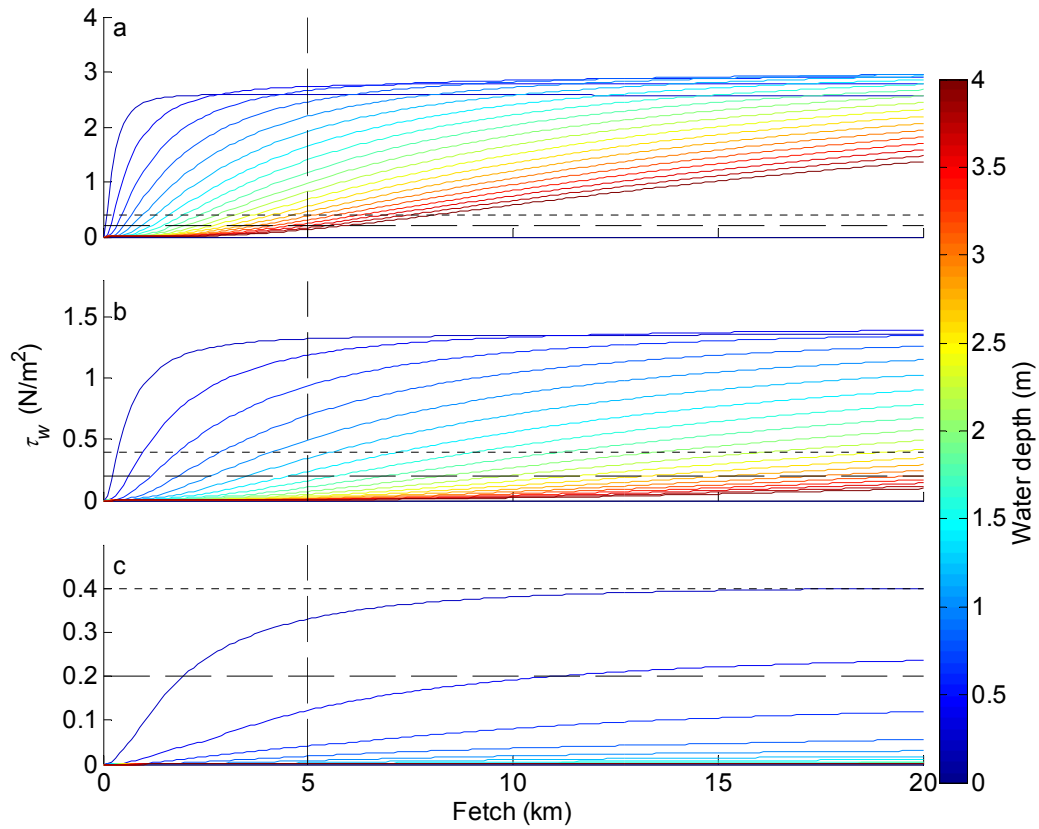


Figure 4.9: Values of τ_w calculated for a range of fixed water depths and fetches for a strong (10 m/s, a), a moderate (5 m/s) and a weak (2 m/s, c) wind speed. The vertical black dashed lines represent maximum fetch length in the northern arm of the case study site. The horizontal black dashed and dotted lines represent approximate maximum basin-averaged values of τ in the subtidal channel during a spring and neap tide from the Raglan Harbour numerical model. Note the change in y-axis scale between a, b and c.

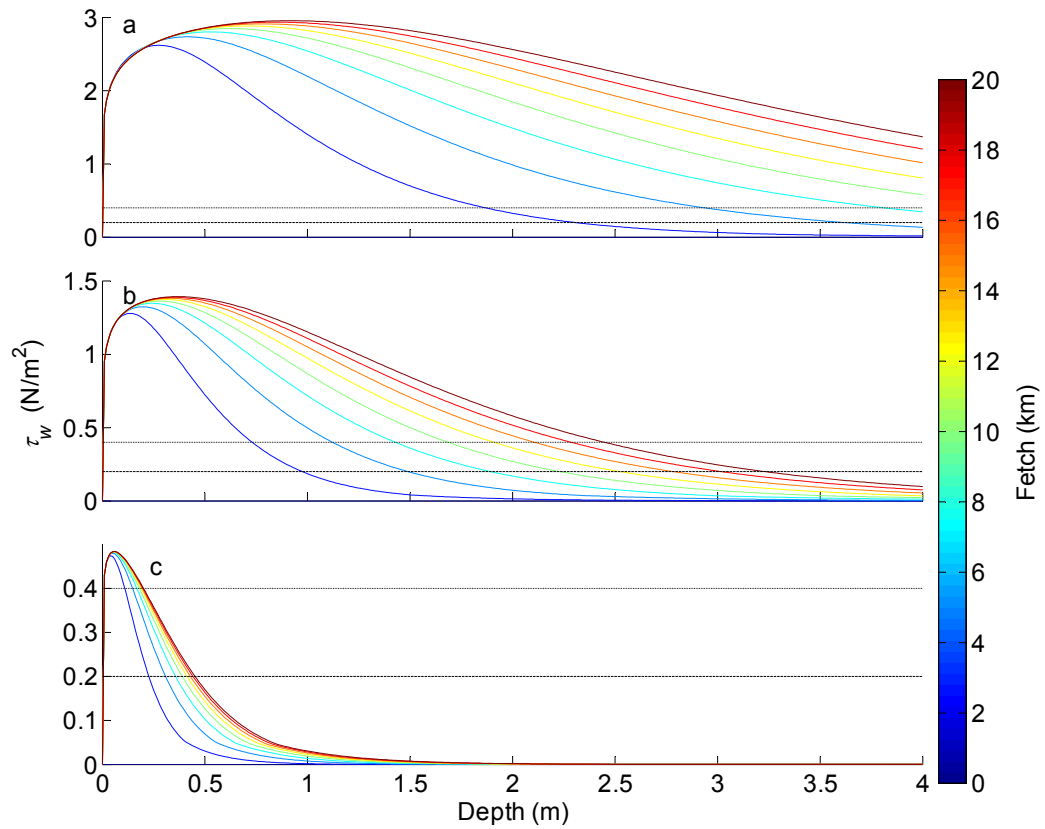


Figure 4.10: Calculated values of τ_w for a range of fixed water depths and fetches for a strong (10 m/s, a), a moderate (5 m/s) and a weak (2 m/s, c) wind speed. The horizontal black dashed and dotted lines represent approximate maximum basin-averaged values of τ in the subtidal channel during a spring and neap tide from the Raglan Harbour numerical model. Note the change in y-axis scale between a, b and c.

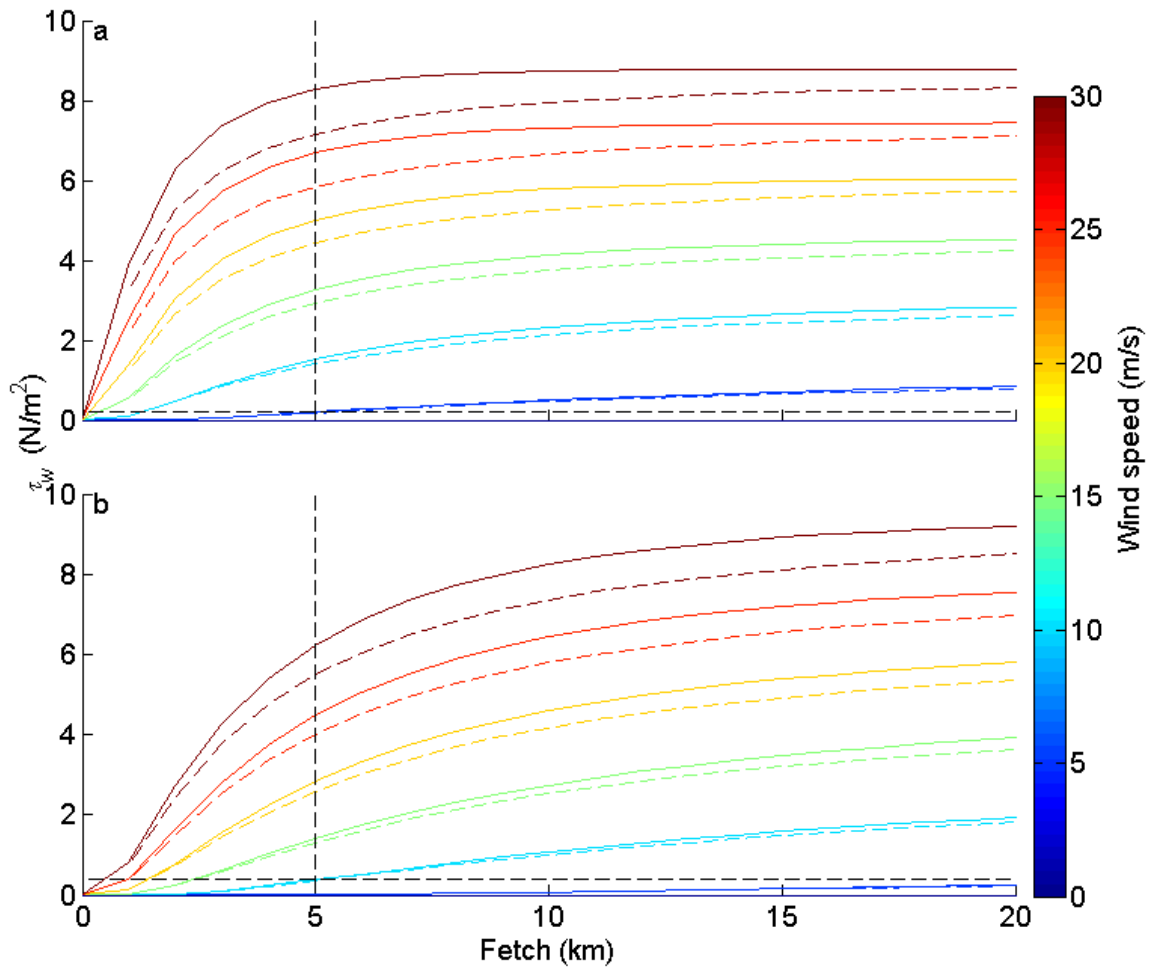


Figure 4.11: Values of τ_w for a range of wind speeds and fetches for a typical neap (1.5 m, a) and spring (3 m, b) water depth (solid lines). Values of τ_w are also shown for water depths modified by storm setup, taking into account both fetch and wind speed (dashed lines). The vertical black dashed lines represent maximum fetch length in the northern arm of the case study site. The horizontal black dashed lines represent approximate maximum basin-averaged values of τ in the subtidal channel of Raglan Harbour numerical model.

Chapter 5. Conclusions and future research



Whaingaroa (Raglan) Harbour mouth and the Tasman Sea from Ngarunui Beach.

5.1 General conclusions

The research presented in this thesis advances the understanding of wave processes in estuaries and how waves interact with tides to shape estuarine morphology. In Section 1.2, the aims of the thesis were abstracted into three research questions.

1 How do waves and tides interact to control whether an estuary exports or imports sediment?

This research shows that the interactions between waves and tides in mesotidal estuaries are more complex than those previously studied in microtidal estuaries. Tides in mesotidal estuaries are associated with strong and often asymmetric tides that are capable of transporting more sediment than tides in microtidal environments. Wind and waves are able to modify these tidal asymmetry patterns through the interruption of deposition around slack water, the reversal of the sediment gradient between intertidal and subtidal areas and the modification of circulation patterns.

Deposition of sediment can usually occur during slack water when currents drop below a critical velocity. In an estuary with a standing tidal wave, or partially standing tidal wave such as presented here, slack water and deposition of sediment occurs around high water when the intertidal areas are flooded. High water slack occurs at the same time as the maximum fetch, and therefore concurrently with the generation of the largest waves, which will disrupt sediment deposition that would otherwise occur when only tidal currents are present. Waves also enhance τ_{max} over the shallower intertidal compared to the deeper subtidal area creating a spatial sediment gradient and advection of sediment towards the subtidal areas.

Winds also create a residual circulation pattern in the estuary basins, these circulation patterns are strongest when winds are orientated with the main axis of the basin and blowing in an up-estuary direction towards the upper reaches of the estuarine basin. The wind enhances flow with the wind over the intertidal areas and creates a small setup against the head of the estuary and a strengthened return current through the subtidal part of the estuary against the wind. As might be

expected, the wind speed strength is directly related to the magnitude of wave and wind circulation with larger wind speeds exerting a greater modification on the overall hydrodynamic regime.

2 How does the morphology (fetch and intertidal shape) influence whether exporting or importing conditions occur, and how does this vary spatially through an estuary?

Waves, tides and morphology are related through a series of non-linear feedbacks which are very sensitive to the depth difference between the subtidal and intertidal areas. Deep intertidal areas encourage greater current speeds during the flood part of the tide because of the greater tidal prism in the intertidal; this tidal pattern encourages the import of sediment. In more infilled basins with shallower intertidal areas, currents are strengthened during the ebb in the subtidal areas but not over the intertidal areas where a slightly progressive tidal wave promotes flood dominance. These asymmetry patterns indicate that under tidal processes only, there is no evidence of a morphological equilibrium caused by a balance between flood and ebb dominance because shallower (infilled) intertidal areas do not lead to ebb dominance and erosion. Instead morphological equilibrium can only arise from infilling, where intertidal areas infill to a point where flows are too weak to transport sediment.

An alternative explanation for the existence of an estuary basin morphological equilibrium due to opposing patterns of accretion and erosion is provided through the incorporation of waves. Orbital velocities decay with depth so the disruption to slack water is more apparent over shallower intertidal areas; therefore this process exerts a control on the amount of intertidal infilling in which sediment deposition can only reach a critical depth before waves halt deposition. These differing pathways to morphological equilibrium within tidally-dominated and wave-dominated environments result in distinct characteristic basin morphologies. Wave dominated environments have deeper (unfilled) concave intertidal areas and shallow (relative to the intertidal elevation) flood dominant or weakly ebb dominant subtidal channels. Within tidally dominated environments, the intertidal areas are shallower (infilled) and convex and the subtidal regions are characterised by a deep (relative to the intertidal elevation) incised ebb dominant channel.

The strength of τ_w depends on fetch length which affects wave size and water depth, which in turn affect the strength of orbital velocities at the seabed. Within the mesotidal case study outlined here, the relatively large difference between neap and spring tides leads to a noticeable variation in both fetch and depth. The concave shape of the morphology in a wave dominated environment steepens the intertidal causing the fetch reduction between spring and neaps to be small relative to the reduction in depth. The small reduction in fetch allows only a small difference wave generation potential between springs and neaps relative to the increased penetration of orbital velocities afforded by the shallower water depths. This increase in τ_w over the intertidal along with lower τ in the subtidal areas during neaps, results in a reduced length of slack duration and an increased seaward advection of sediment. The net result is that erosion is more likely under neap rather than spring conditions in a wave dominated mesotidal environment.

This research highlights the important links between waves, tides and estuarine morphology. When considering the management of estuaries, especially on a regional-scale such as in a coastal management plan, there is often emphasis placed on broad-scale measures of hydrodynamics such as tidal asymmetry. The use of a single value of tidal asymmetry is appealing as it appears to provide a simple summary descriptor of an estuary's role as either a source or sink for sediment within the coastal system. However, here it is shown that use of a single metric of tidal asymmetry is misleading due to both the spatial variability of tidal asymmetry throughout an estuary and the important role of wind and waves. Predictions of future estuarine morphology are already complex due to natural and anthropogenic factors. When also considering wind and waves this complexity will be increased due to complex non-linear feedbacks and uncertainties about the affect of climate change on future wind patterns.

3 Waves depend on wind conditions, which can vary over a number of timescales. Under which conditions do waves become more important than tides for modifying asymmetry?

In this thesis, waves are considered to be a morphologically significant hydrodynamic process when waves are able to influence the basin-wide morphology over a decadal timescale. This definition of morphological

significance relates to conditions that are somewhere between the two extremes of (1) infrequent storm events that may have a dramatic but short lived impact on morphology and (2) frequent events that are of small magnitude and therefore have limited impact on the morphology. The wave size is dependent on both the wind speed and the available fetch, with smaller fetches requiring larger wind speeds to create morphologically-significant waves and larger fetches requiring smaller wind speeds to generate waves that generate comparable bed shear stress. For the fetch lengths tested here (maximum length = 5km), wind speeds of $< \sim 5$ m/s are unable to generate waves large enough to be considered morphologically significant despite occurring frequently. However, winds $\sim > 10$ m/s create waves large enough to completely reverse any flood dominance over intertidal areas regardless of the size of the fetch but are too infrequent to be considered morphologically significant. Winds $\sim > 5$ m/s $\sim < 10$ m/s are morphologically significant but only in estuaries where the fetch is large enough, such as in the northern arm of the case study site where the fetch is 5km under the prevailing wind direction. Winds between $\sim 5 - 8$ m/s are especially important as they occur frequently in daily sea breeze patterns but are also of sufficient strength to generate waves large enough to reverse patterns of flood dominated tidal asymmetry when the fetch is ~ 5 km or greater. The idea of morphological significant wave conditions explains the different morphology and sedimentation rates in the wave-dominated (and fetch aligned) and tidally-dominated (and non-fetch aligned) arms of the harbour. This research shows that for waves to be considered morphologically significant in the typical temperate westerly wind conditions experienced in the north island of New Zealand, the estuary needs to be aligned with the prevailing wind direction. However, the overall ability of waves to become morphologically significant depend not only the fetch length and orientation relative to the prevailing wind directions and speeds, but also the strength of tidal currents and the timing of slack duration and peak velocities, which varies between estuaries depending on the tidal prism and relative intertidal area.

The timing of a wind event relative to the tidal stage is a critical consideration when assessing the magnitude of the impact of waves on sediment transport. Here, this timing has been found to be complex involving a combination of both

local sea breeze patterns and regional climatic affects. This complex pairing between climate and oceanography has been represented within this research by establishing realistic envelopes of τ_{max} through the combination of wind events of varying probability with tides of differing ranges. The severity of each modelled event can then be determined through a consideration of the probability of each wind alongside its magnitude of affect. The availability of hydrodynamic and sedimentary record has provided an opportunity to test this approach and indicates that this method provides a viable method for assessing the impact of wind waves on an estuarine system.

5.2 Directions for future research

The effect of wind and waves on estuarine morphology can be tested by collecting morphological information and comparing the morphology to historical weather records. Useful and simple descriptors of estuary morphology include basin hypsometry and fetch length compared to the prevailing wind direction. The conclusions regarding estuarine morphology and wave dominated environments presented in this research imply that basins with deeper and more concave form will be orientated in the same direction as the prevailing wind direction. Within estuaries where the fetch is either too small or not aligned with the prevailing wind direction then there should be evidence of infilling and a more concave intertidal area.

The basins investigated here are typified by a predominantly standing wave tidal pattern where maximum tidal currents occur around mid tide and slack water occurs around high and low water. When tidal waves are fully progressive, these maximum velocities occur around high and low water and slack water occurs at mid tide. Under a progressive tidal wave, the maximum flood flow will occur whilst the intertidal area is flooded and the maximum fetch will coincide with this peak velocity presumably leading to a very different response to waves in estuaries of this type. Further research should be extended into estuaries with more progressive tidal waves in addition to macrotidal systems.

References

Agardy, T. and Alder, J. 2005. Coastal Systems. In: Hassan, R., Scholes, R. And Ash, N. (eds.) Ecosystems and Human Well-being: Current State and Trends, Volume 1. Findings of the Conditions and Trends Working Group of the Millennium Ecosystem Assessment. Island Press.

Aubrey, D.G. and Speer, P.E. 1985. A Study of Non-linear Tidal Propagation in shallow Inlet/estuarine Systems Part I: Observations. *Estuarine, Coastal and Shelf Science* 21, pp. 185-205.

Augustinus, P.G.E.F. 1980. Actual Development of the Chenier Coast of Suriname (South America). *Sedimentary Geology*, 26, pp. 91 – 113.

Bearman, J. A., Friedrichs, C. T., Jaffe, B. E. & Foxgrover, A. C. 2010. Spatial Trends in Tidal Flat Shape and Associated Environmental Parameters in South San Francisco Bay. *Journal of Coastal Research*, 26, 342-349.

Bentley, S.J., Swales, A., Pyenson, B. and Dawe, J. 2014. Sedimentation, bioturbation, and sedimentary fabric evolution on a modern mesotidal mudflat: A multi-tracer study of processes, rates and scales. *Estuarine, Coastal and Shelf Science*, 141, 58-68.

Bolle, A., Bing Wang, Z., Amos, C. and de Ronde, J. 2010. The influence of changes in tidal asymmetry on residual sediment transport in the Western Scheldt. *Continental Shelf Research*, 30, 871-882.

Booij, N., Ris, R.C. and Holthuijsen, L.H. 1999. A third-generation wave model for coastal regions. 1. Model description and validation. *Journal of Geophysical Research*, 104, 7649-7666.

Boon, J. D. 1975. Tidal discharge asymmetry in a salt marsh drainage system. *Journal of Limnology and Oceanography*, 20, 71-80.

Boon, J. D. and Byrne, R. J. 1981. On basin hypsometry and the morphodynamic response of coastal inlet systems. *Marine Geology*, 40, 27-48.

Bouma, T.J., van Belzen, J., Balke, T., Zhu, Z., Airoidi, L., Blight, A.J., Davies, A.J., Galvan, C., Hawkins, S.J., Hoggart, S.P.G., Lara, J.L., Losada, I.J., Maza, M., Ondiviela, B., Skov, M.W., Strain, E.M., Thompson, R.C., Yang, S., Zanuttigh, B., Zhang, L. and Herman, P.M.J. 2014. Identifying knowledge gaps hampering application of intertidal habitats in coastal protection: Opportunities & steps to take. *Coastal engineering* 87, pp. 147-157.

Bowers, D.G. and Al-Barakati, A. 1997. Tidal Rectification on Drying Estuarine Sandbanks. *Estuaries*, Vol. 20, No. 3, 559-568.

Brown, J. M. and Davies, A. G. 2010. Flood/ebb tidal asymmetry in a shallow sandy estuary and the impact on net sand transport. *Geomorphology*, 114, 431-439.

Cameron, W.M. and Pritchard, D.W. 1963. Estuaries. In: Hill, M.N. (ed.) *The Sea*, Vol. 2. Wiley, New York, 306-324.

CERC. 1984. *Shore Protection Manual*, Volume 1. Waterways Experiment Station, Corps of Engineers, Coastal Engineering Research Center (CERC).

Coco, G., Zhou, Z., van Maanen, B., Olabarrieta, M., Tinoco, R. And Townend, I. 2013. Morphodynamics of tidal networks: Advances and challenges. *Marine Geology*, 346, 1-16.

Colby, L. H., Maycock, S. D., Nelligan, F. A., Pocock, H. J. and Walker, D. J. 2010. An Investigation into the Effect of Dredging on Tidal Asymmetry at the River Murray Mouth. *Journal of Coastal Research*, 26, 843-850.

Dayton, P.K. 2003. The Importance of the Natural Sciences to Conservation. *The American Naturalist*, Vol. 162, No. 1, pp. 1-13.

de Lange, W. and Healy, T. 1990. Wave Spectra for a Shallow Meso-Tidal Estuarine Lagoon: Bay of Plenty, New Zealand. *Journal of Coastal Research*, 6, 189-199.

Dronkers, J. 1986. Tidal asymmetry and estuarine morphology. *Netherlands Journal of Sea Research*, 20, 117-131.

Duke, N.C. 1992. Mangrove floristics and biogeography. In: Tropical Mangrove Ecosystems. Robertson, A.I and Alongi, D.M. (Eds), American Geophysical Union.

Dyer, K.R. 1997. Estuaries: A Physical Introduction, 2nd edition. John Wiley and Sons, Chichester.

Eiser, W. C. and Kjerfve, B. 1986. Marsh topography and hypsometric characteristics of a South Carolina salt marsh basin. *Estuarine, Coastal and Shelf Science*, 23, 595-605.

Elias, E.P.L., Gelfenbaum, G. and Van der Westhuysen, A.J. 2012. Validation of a coupled wave-flow model in a high energy setting: The mouth of the Columbia River. *Journal of Geophysical research*, Vol. 117.

Elliott, A. H., Shanker, U., Hicks, D. M., Woods, R. A. & Dymond, J. R. 2008. SPARROW regional regression for sediment yields in New Zealand rivers. In: Schmidt, J., Cochrane, T., Phillips, C., Elliott, S., Davies, T. & Basher, L. (eds.) *Sediment Dynamics in Changing Environments*. Christchurch, NZ: International Association of Hydrological Sciences.

Fagherazzi, S., Carniello, L., D'Alpaos, A. and Defina, A. 2006. Critical bifurcation of shallow microtidal landforms in tidal flats and salt marshes. *Proc. Natl. Acad. Sci. USA*, 103, 8337-8341.

Fagherazzi, S., Palermo, C., Rulli, M. C., Carniello, L. and Defina, A. 2007. Wind waves in shallow microtidal basins and the dynamic equilibrium of tidal flats. *J. Geophys. Res.*, 112, F02024.

Fagherazzi, S., Hannon, M. and D'Odorico, P. 2008. Geomorphic structure of tidal hydrodynamics in salt marsh creeks. *Water Resources Research*, Vol. 44.

Fagherazzi, S. and Wiberg, P. L. 2009. Importance of wind conditions, fetch, and water levels on wave-generated shear stresses in shallow intertidal basins. *J. Geophys. Res.*, 114, F03022.

- Fortunato, A. B. and Oliveira, A. 2005. Influence of Intertidal Flats on Tidal Asymmetry. *Journal of Coastal Research*, 21, 1062-1067.
- French, J.R., Burningham, H. and Benson, T. 2008. Tidal and Meteorological Forcing of Suspended Sediment Flux in a Muddy Mesotidal Estuary. *Estuaries and Coasts*, 31, 843-859.
- Friedrichs, C. T. 2010. Barotropic tides in channelized estuaries. In: Valle-Levinson, A. (ed.) *Treatise on Contemporary Issues in Estuarine Physics*. Cambridge University Press, Cambridge, 27-61.
- Friedrichs, C. T. 2011. Tidal flat morphodynamics: a synthesis. In: Hansom, J. D. & Flemming, B. W. (eds.) *Treatise on Estuarine and Coastal Science, Volume 3: Estuarine and Coastal Geology and Geomorphology*. Elsevier.
- Friedrichs, C. T. and Aubrey, D. G. 1988. Non-linear tidal distortion in shallow well-mixed estuaries: a synthesis. *Estuarine, Coastal and Shelf Science*, 27, 521-545.
- Friedrichs, C. T. & Aubrey, D. G. 1996. Uniform bottom shear stress and equilibrium hypsometry of intertidal flats. In: Pattiaratchi, C. B. (ed.) *Mixing in Estuaries and Coastal Seas*. Washington, DC: AGU.
- Gao, S. and Collins, M. 1994. Tidal Inlet Equilibrium, in relation to Cross-sectional area and Sediment transport Patterns. *Estuarine, Coastal and Shelf Science*, 38, 157-172.
- Green, M.O. 2011. Very small waves and associated sediment resuspension on an estuarine intertidal flat. *Estuarine, Coastal and Shelf Science*, 93, 449-459.
- Green, M. O., Black, K. P. and Amos, C. L. 1997. Control of estuarine sediment dynamics by interactions between currents and waves at several scales. *Marine Geology*, 144, 97-116.
- Green, M.O., Bell, R., Dolphin, T.J. and Swales, A. 2000. Silt and sand transport in a deep tidal channel of a large estuary (Manakau Harbour, New Zealand). *Marine Geology*, 163, 217-240.

- Griffiths, G. A. & Glasby, G. P. 1985. Input of river-derived sediment to the New Zealand continental shelf: I. *Mass. Estuarine, Coastal and Shelf Science*, 21, 773-787.
- Hannah, S.J. 2004. An updated analysis of long-term sea level change in New Zealand. *Geophysical Research Letters*, Vol. 31, 1-4.
- Heath, R.A. 1976. Broad classification of New Zealand inlets with emphasis on residence times. *New Zealand Journal of Marine and Freshwater Research*. 10, 3, pp. 429-444.
- Heath, R.A. and Shakepeare, B.S. 1977. Summer temperatures and salinity distribution on three small inlets on the West Coast, North Island, New Zealand. *New Zealand Oceanographic Institute records*, Vol. 3, No. 17, pp. 151-158.
- Henderson, S.M. and Mullarney, J.C. 2013. Wave mixed, wind-generated near-surface shear observed over a tidal flat. *Continental Shelf Research*, 60S, S22-S29.
- Hicks, D. M., Shanker, U., McKerchar, A. I., Basher, L., Lynn, I., Page, M. & Jessen, M. 2011. Suspended sediment yields from New Zealand rivers. *Journal of Hydrology, New Zealand*, 50, 81-142.
- Horstman, E.M., Dohmen-Janssen, C.M. and Hulscher, S.J.M.H. 2013. Flow routing in mangrove forests: A field study in Trang province, Thailand. *Continental Shelf Research*, 71, 52-67.
- Hsu, S. A., J. M. Grymes III, and Z. Yan. 1997. A simplified hydrodynamic formula for estimating the wind-driven flooding in the Lake Pontchartrain-Amite River basin. *National Weather Digest*, 21:4, pp. 18 - 22.
- Hume, T.M. and Herdendorf, C.E. 1993. On the Use of Empirical Stability Relationships for Characterising Estuaries. *Journal of Coastal Research*. Vol. 9, No. 2, pp. 413 – 422.

Hume, T.M., Snelder, T., Weatherhead, M. and Liefing, R. 2007. A controlling factor approach to estuary classification. *Ocean & Coastal Management* 50, 905-929.

Hunt, S., Bryan, K.R., Mullarney, J.C. 2015. The influence of wind and waves on the existence of stable intertidal morphology in meso-tidal estuaries. *Geomorphology*, 228, pp. 158-174.

Hunt, S., Bryan, K.R., Mullarney, J.C. and Pritchard, M. 2016. Observations of asymmetry in contrasting wave- and tidally-dominated environments within a mesotidal basin: implications for estuarine evolution. *Earth Surface Processes and Landforms*, DOI: 10.1002/esp.3985

Janssen-Stedler, B. 2000. The effect of different hydrodynamic conditions on the morphodynamics of a tidal mudflat in the Dutch Wadden sea. *Continental Shelf Research*, 20, 1461-1478.

Jarrett, J.T. 1976. Tidal Prism – Inlet Area Relationships. General Investigation of Tidal Inlets (GITI) Report 3, Department of the Army Corp of Engineers.

Jones, N.L. and Monismith, S.G. 2007. Measuring short-period wind waves in a tidally forced environment with a subsurface pressure gauge. *Limnology and Oceanography: Methods* 5, pp.317-327.

Kaiser, D, Unger, D., Qin, G., Zhou, H. And Gan, H. 2013. Natural and human influences on nutrient transport through a small subtropical Chinese estuary. *Science of the Total Environment*, 450-451, 92-107.

Kirby, R. 2000. Practical Implications of tidal flat shape. *Continental Shelf Research*, 20, 1061-1077.

Kirby, R. 2002. Distinguishing accretion from erosion-dominated muddy coasts. In: Healy, T., Wang, H. and Healy, J.-A. (eds.) *Muddy Coasts of the World: Processes Deposits and Function*. Amsterdam: Elsevier Science B.V.

- Kirby, J.R. and Kirby, R. 2008. Medium timescale stability of tidal mudflats in Bridgwater Bay, Bristol Channel, UK: Influence of tides, waves and climate. *Continental Shelf research*, 28, 2615-2629.
- Kotze, C., Grant, S. & Hill, R. 2008. Suspended Sediment Monitoring Report 2007. Environment Waikato. 1-37
- Lanzoni, S. & Seminara, S. 2002. Long-term evolution and morphodynamic equilibrium of tidal channels. *Journal of Geophysical research*, Vol. 107, No. C1, 1-13.
- le Hir, P., Roberts, W., Cazaillet, O., Christie, M., Bassoullet, P. and Bacher, C. 2000. Characterization of intertidal flat hydrodynamics. *Continental Shelf Research*, 20, 1433-1459.
- Lesser, G.R., Roelvink, J.A., van Kester, J.A.T.M. and Stelling, G.S. 2004. Development and validation of a three-dimensional morphological model. *Coastal Engineering*, 51, 883-915.
- Liu, Y., MacCready, P., Hikey, B.M., Dever, E.P., Kosro, P.M. and Banas, N.S. 2009. Evaluation of a coastal ocean circulation model for the Columbia River plume in summer 2004. *Journal of Geophysical research*, Vol. 114.
- Mariotti, G. and Fagherazzi, S. 2012a. Channels-tidal flat sediment exchange: The channel spillover mechanism. *Journal of Geophysical research*, Vol. 117, C03032.
- Mariotti, G. and Fagherazzi, S. 2012b. Modeling the effect of tides and waves on benthic biofilms. *Journal of Geophysical research*, Vol. 117.
- Mariotti, G. & Fagherazzi, S. 2013a. A two-point dynamic model for the coupled evolution of channels and tidal flats. *Journal of Geophysical Research: Earth Surface*, 118, 1387-1399.
- Mariotti, G. And Fagherazzi, S. 2013b. Wind waves on a mudflat: The influence of fetch and depth on bed shear stresses. *Continental Shelf Research*, 60S, pp.S99-S110

McGlathery, K.J., M.A. Reidenbach, P. D'Odorico, S. Fagherazzi, M.L. Pace, and J.H. Porter. 2013. Nonlinear dynamics and alternative stable states in shallow coastal systems. *Oceanography* 26(3), 220–231.

McKergow, L. A., Pritchard, M., Elliott A. H., Duncan, M. J. & Senior, A. K. 2010. Storm fine sediment flux from catchment to estuary, Waitetuna-Raglan Harbour, New Zealand. *New Zealand Journal of Marine and Freshwater Research*, 44, 53-76.

Mehta, A. J. 2002. Mudshore dynamics and controls. In: Healy, T., Wang, H. and Healy, J.-A. (eds.) *Muddy Coasts of the World: Processes Deposits and Function*. Amsterdam: Elsevier Science B.V.

Mokrech, M. Gardiner, S, Nicholls, R.J., Watkinson, A.R. and Sutherland, W.J. 2015. Coastal Wetland Habitats: Future Challenges and Potential Solutions. In: Nicholls, R.J, Dawson, R.J. and Day, S.A. (ed.) *Broad Scale Coastal Simulation. New Techniques to Understand and Manage Shorelines in the Third Millennium*. *Advances in Global Change Research* 49, Springer Science.

Möller, I., Spencer, T., French, J.R., Leggett, D.J. and Dixon, M. 1999. Wave Transformation over Salt Marshes: A Field and Numerical Modelling Study from North Norfolk, England. *Estuarine, Coastal and Shelf Science* 49, 411–426

Moore, R. D., Wolf, J., Souza, A. J. and Flint, S. S. 2009. Morphological evolution of the Dee Estuary, Eastern Irish Sea, UK: A tidal asymmetry approach. *Geomorphology*, 103, 588-596.

Narváez, D.A. and Valle-Levinson, A. 2008. Transverse structure of wind-driven flow at the entrance to an estuary: Nansemond River. *Journal of Geophysical Research*, 113, C09004,1-9.

Needham, H., Singleton, N., Giles, H. and Jones, H. 2014. Regional estuary Monitoring Programme 10 year trend report: April 2001 to April 2011. Waikato Regional Council Technical Report 2014/41.

O'Brien, M.P. 1969. Equilibrium Flow Areas of Inlets on Sandy Coasts. *Journal of the Waterways and Harbors Division, Proceedings of the American Society of Civil Engineers*, Vol. 95, No. WW1.

O'Brien, D.J., Whitehouse, R.J.S. and Cramp, A. 2000. The cyclic development of a macrotidal mudflat on varying timescales. *Continental Shelf Research*, 20, 1593-1619.

Pawlowicz, R., Beardsley, B. And Lentz, S. 2002. Classical tidal harmonic analysis including error estimates in MATLAB using T_TIDE. *Computers and Geosciences*, 28, pp. 929-937.

Pethick, J. S. 1994. Estuaries and wetlands: function and form. In: Falconer, R. A. and Goodwin, P. (eds.) *Wetland Management*. London: Thomas Telford Services Ltd.

Prandle, D. 2003. Relationships between Tidal Dynamics and Bathymetry in Strongly Convergent Estuaries. *Journal of Physical Oceanography*, Vol 23, pp. 2738 – 2750.

Pritchard, D. 2005. Suspended sediment transport along an idealised tidal embayment: settling lag, residual transport and the interpretation of tidal signals. *Ocean Dynamics*, 55, 124-136.

Pugh, D. 2004. *Changing Sea Levels. Effects of Tides, Weather and Climate*. Cambridge University Press. ISBN 0 521 53218 3.

Quartel, S., Kroon, A., Augustinus, P.G.E.F., Van Santen, P. and Tri, N.H. 2007. Wave attenuation in coastal mangroves in the Red river Delta, Vietnam. *Journal of Asian Earth Sciences*, 29, 564-584.

Ranasinghe, R., McLoughlin, R., Short, A. And Symonds, G. 2004. The Southern Oscillation Index, wave climate, and beach rotation. *Marine Geology*, 204, pp. 273-287.

Ridderinkhof, H. 1997. The Effect of Tidal Asymmetries on the Net Transport of Sediments in the Ems Dollard Estuary. *Journal of Coastal Research*, Special Issue no. 25, 41-48.

Riffe, K.C., Henderson, S.M. and Mullarney, J.C. 2011. Wave dissipation by flexible vegetation. *Geophysical Research Letters*, 38, L18607.

Rinaldo, A., Fagherazzi, S., Lanzoni, S., Marani, M. and Dietrich, W.E. 1999. Tidal networks 3. Landscape-forming discharges and studies in empirical geomorphic relationships. *Water Resources Research*, Vol. 35, No. 12, pp. 3919-3929.

Roberts, W., Le Hir, P. & Whitehouse, R. J. S. 2000. Investigation using simple mathematical models of the effect of tidal currents and waves on the profile shape of intertidal mudflats. *Continental Shelf Research*, 20, 1079-1097.

Robins, P.E. and Davies, A.G. 2010. Morphological controls in sandy estuaries: the influence of tidal flats and bathymetry on sandy transport. *Ocean Dynamics*, 60, pp. 503-517.

Rohweder, J., Rogala, J. T., Johnson, B. L., Anderson, D., Clark, S., Chamberlin, F., Potter, D., and Runyon, K., 2012, Application of Wind Fetch and Wave Models for Habitat Rehabilitation and Enhancement Projects – 2012 Update. Contract report prepared for U.S. Army Corps of Engineers' Upper Mississippi River Restoration – Environmental Management Program. 52 p.

Saney, R. and Valle-Levinson, A. 2005. Wind-Induced Circulation in Semienclosed Homogenous, Rotating Basins. *Journal of Physical Oceanography*, 35, 2520-2531.

Sherwood, A.M. and Nelson, C.S. 1979. Surficial sediments of Raglan Harbour. *New Zealand Journal of Marine and Freshwater Research*, 13, 4, pp. 473-496.

Shi, B.W., Yang, S.L., Wang, Y.P., Bouma, T.J. and Zhu, Q. 2012. Relating accretion and erosion at an exposed tidal wetland to the bottom shear stress of combined current-wave action. *Geomorphology*, 138, 380-389.

Smith, M.J., Stevens, C.L., Gorman, R.M., McGregor, J.A. and Neilson, C.G. 2001. Wind-wave development across a large shallow intertidal estuary: a case study of Manukau Harbour, New Zealand. *New Zealand Journal of Marine and Freshwater Research*, Vol. 35, pp. 985-1000.

Souslby, R. 1997. *Dynamics of Marine Sands: A Manual for Practical Applications*. Published by Thomas Telford Publishing, London.

Speer, P.E. and Aubrey, D.G. 1985. A Study of Non-linear Tidal Propagation in shallow Inlet/estuarine Systems Part II: Theory. *Estuarine, Coastal and Shelf Science* 21, pp. 207-224.

Strahler, A. N. 1952. Hypsometric (area-altitude) analysis of erosional topography. *Geological Society of America Bulletin*, 63, 1117-1142.

Swales, A., Macdonald, I. T. and Green, M. O. 2004. Influence of Wave and Sediment Dynamics on Cordgrass (*Spartina anglica*) Growth and Sediment Accumulation on an Exposed Intertidal Flat. *Estuaries*, 27, 225-243.

Swales, A., Ovenden, R., McGlone, M.S., Hermanspahn, N., Budd, R., Okey, M.J. and Hawken, J. 2005. Whaingaroa (Raglan) Harbour: sedimentation rates and the effects of historical catchment landcover changes. NIWA technical report for Environment Waikato. Technical report 2005/36.

Syvitski, J.P.M., Vörösmarty, C.J., Kettner, A.J. and Green, P. 2005. Impact of Humans on the Flux of Terrestrial Sediment to the Global Coastal Ocean. *Science*, Vol. 308, No. 5720, pp. 376-380.

Talke, S.A. and Stacey, M.T. 2008. Suspended sediment fluxes at an intertidal flat: The shifting influence of wave, wind, tidal and freshwater forcing. *Continental Shelf Research*, 28, pp. 710-725.

Tay, H.W., Bryan, K.R., Pilditch, C.A., Park, S. and Hamilton, D.P. 2012. Variations in nutrient concentrations at different time scales in two shallow tidally dominated estuaries. *Marine and Freshwater Research*, 63, 95-109.

- Tono, D.D. and Chmura, G.L. 2013. Coastal Squeeze of Tidal Wetlands. *Journal of Coastal Research*, Vol. 29, No. 5, pp. 1049-1061.
- Townend, I. 2005. An Examination of Empirical Stability Relationships for UK Estuaries. *Journal of Coastal Research*, 21, 5, 1042-1053.
- Townend, I.T. 2010. An exploration of equilibrium in Venice Lagoon using an idealised form model. *Continental Shelf Research*, 30, 984-999.
- Trasviña, A., Ortiz-Figueroa, M., Herrera, H., Cosío, M. A. & González, E. 2003. 'Santa Ana' winds and upwelling filaments off Northern Baja California. *Dynamics of Atmospheres and Oceans*, 37, 113-129.
- van Maanen, B., Coco, G. & Bryan, K. R. 2013a. Modelling the effects of tidal range and initial bathymetry on the morphological evolution of tidal embayments. *Geomorphology*, 191, 23-34.
- van Maanen, B., Coco, G., Bryan, K.R. & Friedrichs, C. T. 2013b. Modelling the morphodynamic response of tidal embayments to sea-level rise. *Ocean dynamics*, Volume 63, Issue 11-12, pp. 1249-1262.
- van Maanen, B., Coco, G., Bryan, K.R. (2015). On the ecogeomorphological feedbacks that control tidal channel network evolution in a sandy mangrove setting. *Proc. R. Soc. A* 201501115. <http://dx.doi.org/10.1098/rspa.2015.0115>.
- van Santen, P., Augustinus, P.G.E.F., Janssen-Stelder, Quartel, S. and Tri, N.H. 2007. Sedimentation in an estuarine mangrove system. *Journal of Asian earth Sciences*, 29, 566-575.
- Waeles, B. T., Le Hir, P. & Silva Jacinto, R. 2004. Modélisation morphodynamique cross-shore d'un estran vaseux. *Comptes Rendus Geoscience*, 336, 1025-1033.
- Wang, Z. B., Jeuken, M. C. J. L., Gerritsen, H., de Vriend, H. J. and Kornman, B. A. 2002. Morphology and asymmetry of the vertical tide in the Westerschelde estuary. *Continental Shelf Research*, 22, 2599-2609.

Warner, J.C., Rockwell Geyer, W. and Lertzak, J.A. 2005. Numerical modelling of and estuary: A comprehensive skill assessment. *Journal of Geophysical Research*, Vol. 110.

Wells, J.T. and Coleman, J.M. 1981. Physical Processes and Fine-Grained Sediment Dynamics, Coast of Surinam, South America. *Journal of Sedimentary Petrology*, Vol. 51, No. 4, pp. 1053 – 1068.

Whitehouse, R., Soulsby, R., Roberts, W. And Mitchener, H. 2000. Dynamics of estuarine muds: a manual for practical applications, Telford.

Willmott, C.J. 1981. On the validation of models. *Physical Geography*, Vol. 2, Issue 2.

Winterwerp, J.C. and Wang, Z.B. 2013. Man-induced regime shifts in small estuaries-I: theory. *Ocean Dynamics*, 63, 1279-1292.

Winterwerp, J.C., Wang, Z.B., van Braeckel, A. van Holland, G and Kösters, F. 2013. Man-induced regime shifts in small estuaries-II: a comparison of rivers. *Ocean Dynamics*, 63, 1279-1292.

Woodroffe, C.D. 2002. Coasts. Form, process and evolution. Cambridge University Press.

Wong, K-C. 1994. On the nature of transverse variability in a coastal plain estuary. *Journal of Geophysical Research*, 99, C7, 14, 209-14.

Wong, P.P., I.J. Losada, J.-P. Gattuso, J. Hinkel, A. Khattabi, K.L. McInnes, Y. Saito, and A. Sallenger, 2014: Coastal systems and low-lying areas. In: *Climate Change 2014: Impacts, Adaptation, and Vulnerability. Part A: Global and Sectoral Aspects. Contribution of Working Group II to the Fifth Assessment Report of the Intergovernmental Panel on Climate Change* [Field, C.B., V.R. Barros, D.J. Dokken, K.J. Mach, M.D. Mastrandrea, T.E. Bilir, M. Chatterjee, K.L. Ebi, Y.O. Estrada, R.C. Genova, B. Girma, E.S. Kissel, A.N. Levy, S. MacCracken, P.R. Mastrandrea, and L.L. White (eds.)]. Cambridge University Press, Cambridge, United Kingdom and New York, NY, USA, pp. 361-409.

Zhou, Z., Coco, G., van der Wegen, M., Ghong, Z., Zhang, C. and Townend, I. 2015. Modeling sorting dynamics of cohesive and non-cohesive sediments on intertidal flats under the effect of tides and wind waves. *Continental Shelf Research*, pp. 76-91.